

Models for Predicting Reflection Cracking of Hot-Mix Asphalt Overlays

DETAILS

60 pages | | PAPERBACK

ISBN 978-0-309-15505-2 | DOI 10.17226/14410

AUTHORS

Fujie Zhou; Robert L Lytton; Sheng Hu; Rong Luo; Fang-Ling Tsai; Sang Ick Lee;
Transportation Research Board

BUY THIS BOOK

FIND RELATED TITLES

Visit the National Academies Press at NAP.edu and login or register to get:

- Access to free PDF downloads of thousands of scientific reports
- 10% off the price of print titles
- Email or social media notifications of new titles related to your interests
- Special offers and discounts



Distribution, posting, or copying of this PDF is strictly prohibited without written permission of the National Academies Press. (Request Permission) Unless otherwise indicated, all materials in this PDF are copyrighted by the National Academy of Sciences.

NCHRP REPORT 669

**Models for Predicting
Reflection Cracking of
Hot-Mix Asphalt Overlays**

**Robert L. Lytton
Fang Ling Tsai
Sang-Ick Lee
Rong Luo
Sheng Hu
Fujie Zhou**

TEXAS TRANSPORTATION INSTITUTE
TEXAS A&M UNIVERSITY
College Station, TX

Subscriber Categories
Pavements

Research sponsored by the American Association of State Highway and Transportation Officials
in cooperation with the Federal Highway Administration

TRANSPORTATION RESEARCH BOARD

WASHINGTON, D.C.
2010
www.TRB.org

NATIONAL COOPERATIVE HIGHWAY RESEARCH PROGRAM

Systematic, well-designed research provides the most effective approach to the solution of many problems facing highway administrators and engineers. Often, highway problems are of local interest and can best be studied by highway departments individually or in cooperation with their state universities and others. However, the accelerating growth of highway transportation develops increasingly complex problems of wide interest to highway authorities. These problems are best studied through a coordinated program of cooperative research.

In recognition of these needs, the highway administrators of the American Association of State Highway and Transportation Officials initiated in 1962 an objective national highway research program employing modern scientific techniques. This program is supported on a continuing basis by funds from participating member states of the Association and it receives the full cooperation and support of the Federal Highway Administration, United States Department of Transportation.

The Transportation Research Board of the National Academies was requested by the Association to administer the research program because of the Board's recognized objectivity and understanding of modern research practices. The Board is uniquely suited for this purpose as it maintains an extensive committee structure from which authorities on any highway transportation subject may be drawn; it possesses avenues of communications and cooperation with federal, state and local governmental agencies, universities, and industry; its relationship to the National Research Council is an insurance of objectivity; it maintains a full-time research correlation staff of specialists in highway transportation matters to bring the findings of research directly to those who are in a position to use them.

The program is developed on the basis of research needs identified by chief administrators of the highway and transportation departments and by committees of AASHTO. Each year, specific areas of research needs to be included in the program are proposed to the National Research Council and the Board by the American Association of State Highway and Transportation Officials. Research projects to fulfill these needs are defined by the Board, and qualified research agencies are selected from those that have submitted proposals. Administration and surveillance of research contracts are the responsibilities of the National Research Council and the Transportation Research Board.

The needs for highway research are many, and the National Cooperative Highway Research Program can make significant contributions to the solution of highway transportation problems of mutual concern to many responsible groups. The program, however, is intended to complement rather than to substitute for or duplicate other highway research programs.

NCHRP REPORT 669

Project 01-41
ISSN 0077-5614
ISBN 978-0-309-15505-2
Library of Congress Control Number 2010936725

© 2010 National Academy of Sciences. All rights reserved.

COPYRIGHT INFORMATION

Authors herein are responsible for the authenticity of their materials and for obtaining written permissions from publishers or persons who own the copyright to any previously published or copyrighted material used herein.

Cooperative Research Programs (CRP) grants permission to reproduce material in this publication for classroom and not-for-profit purposes. Permission is given with the understanding that none of the material will be used to imply TRB, AASHTO, FAA, FHWA, FMCSA, FTA, or Transit Development Corporation endorsement of a particular product, method, or practice. It is expected that those reproducing the material in this document for educational and not-for-profit uses will give appropriate acknowledgment of the source of any reprinted or reproduced material. For other uses of the material, request permission from CRP.

NOTICE

The project that is the subject of this report was a part of the National Cooperative Highway Research Program, conducted by the Transportation Research Board with the approval of the Governing Board of the National Research Council.

The members of the technical panel selected to monitor this project and to review this report were chosen for their special competencies and with regard for appropriate balance. The report was reviewed by the technical panel and accepted for publication according to procedures established and overseen by the Transportation Research Board and approved by the Governing Board of the National Research Council.

The opinions and conclusions expressed or implied in this report are those of the researchers who performed the research and are not necessarily those of the Transportation Research Board, the National Research Council, or the program sponsors.

The Transportation Research Board of the National Academies, the National Research Council, and the sponsors of the National Cooperative Highway Research Program do not endorse products or manufacturers. Trade or manufacturers' names appear herein solely because they are considered essential to the object of the report.

Published reports of the

NATIONAL COOPERATIVE HIGHWAY RESEARCH PROGRAM

are available from:

Transportation Research Board
Business Office
500 Fifth Street, NW
Washington, DC 20001

and can be ordered through the Internet at:

<http://www.national-academies.org/trb/bookstore>

Printed in the United States of America

THE NATIONAL ACADEMIES

Advisers to the Nation on Science, Engineering, and Medicine

The **National Academy of Sciences** is a private, nonprofit, self-perpetuating society of distinguished scholars engaged in scientific and engineering research, dedicated to the furtherance of science and technology and to their use for the general welfare. On the authority of the charter granted to it by the Congress in 1863, the Academy has a mandate that requires it to advise the federal government on scientific and technical matters. Dr. Ralph J. Cicerone is president of the National Academy of Sciences.

The **National Academy of Engineering** was established in 1964, under the charter of the National Academy of Sciences, as a parallel organization of outstanding engineers. It is autonomous in its administration and in the selection of its members, sharing with the National Academy of Sciences the responsibility for advising the federal government. The National Academy of Engineering also sponsors engineering programs aimed at meeting national needs, encourages education and research, and recognizes the superior achievements of engineers. Dr. Charles M. Vest is president of the National Academy of Engineering.

The **Institute of Medicine** was established in 1970 by the National Academy of Sciences to secure the services of eminent members of appropriate professions in the examination of policy matters pertaining to the health of the public. The Institute acts under the responsibility given to the National Academy of Sciences by its congressional charter to be an adviser to the federal government and, on its own initiative, to identify issues of medical care, research, and education. Dr. Harvey V. Fineberg is president of the Institute of Medicine.

The **National Research Council** was organized by the National Academy of Sciences in 1916 to associate the broad community of science and technology with the Academy's purposes of furthering knowledge and advising the federal government. Functioning in accordance with general policies determined by the Academy, the Council has become the principal operating agency of both the National Academy of Sciences and the National Academy of Engineering in providing services to the government, the public, and the scientific and engineering communities. The Council is administered jointly by both the Academies and the Institute of Medicine. Dr. Ralph J. Cicerone and Dr. Charles M. Vest are chair and vice chair, respectively, of the National Research Council.

The **Transportation Research Board** is one of six major divisions of the National Research Council. The mission of the Transportation Research Board is to provide leadership in transportation innovation and progress through research and information exchange, conducted within a setting that is objective, interdisciplinary, and multimodal. The Board's varied activities annually engage about 7,000 engineers, scientists, and other transportation researchers and practitioners from the public and private sectors and academia, all of whom contribute their expertise in the public interest. The program is supported by state transportation departments, federal agencies including the component administrations of the U.S. Department of Transportation, and other organizations and individuals interested in the development of transportation. www.TRB.org

www.national-academies.org

COOPERATIVE RESEARCH PROGRAMS

CRP STAFF FOR NCHRP REPORT 669

Christopher W. Jenks, *Director, Cooperative Research Programs*
Crawford F. Jencks, *Deputy Director, Cooperative Research Programs*
Amir N. Hanna, *Senior Program Officer*
Eileen P. Delaney, *Director of Publications*
Margaret B. Hagood, *Editor*

NCHRP PROJECT 01-41 PANEL **Field of Design—Area of Pavements**

Kevin D. Hall, *University of Arkansas - Fayetteville, Fayetteville, AR (Chair)*
Bruce A. Chadbourn, *Minnesota DOT, Maplewood, MN*
Dar-Hao Chen, *Texas DOT, Austin, TX*
Adam J. T. Hand, *Granite Construction, Inc., Sparks, NV*
Abdallah J. Jubran, *Georgia DOT, Forest Park, GA*
Linda M. Pierce, *Applied Pavement Technology, Inc., Santa Fe, NM (formerly Washington State DOT)*
Shakir R. Shatnawi, *Shatec Engineering Consultants LLC, El Dorado Hills, CA (formerly California DOT)*
Timothy E. Smith, *Maryland State Highway Administration, Hanover, MD*
Nelson H. Gibson, *FHWA Liaison*
Stephen F. Maher, *TRB Liaison*

FOREWORD

By Amir N. Hanna

Staff Officer

Transportation Research Board

This report presents mechanistic-based models for predicting the extent and severity of reflection cracking in hot-mix asphalt (HMA) overlays. These models were developed for use in the design and analysis of HMA overlays; they can be incorporated into the *AASHTO Mechanistic-Empirical Pavement Design Guide (MEPDG)* software. The report and accompanying software will guide pavement and construction engineers in identifying and specifying HMA overlays for asphalt and concrete pavements that will provide desired service life and performance. The information contained in the report will be of immediate interest to state pavement engineers and others concerned with the design and rehabilitation of asphalt and concrete pavements.

Reflection cracking is one of the primary forms of distress in HMA overlays of flexible and rigid pavements. In addition to affecting ride quality, the penetration of water and foreign debris into these cracks accelerates the deterioration of the overlay and the underlying pavement, thus reducing service life. The basic mechanism causing reflection cracking is strain concentration in the overlay due to movement in the existing pavement in the vicinity of joints and cracks. This movement may be induced by bending or shearing action resulting from traffic loads or temperature changes and is influenced by traffic volume and characteristics, daily and seasonal temperature variations, and other factors (e.g., pavement structure and condition, HMA mixture properties, the degree of load transfer at joints and cracks). Preliminary models for predicting the extent and severity of reflection cracking in HMA overlays have been developed; however, only limited research has been performed to evaluate and validate these models. Thus, research was needed to address the issues associated with reflection cracking and to develop mechanistic-based models that account for the effects of reflection cracking on performance for use in mechanistic-empirical procedures for the analysis and design of HMA overlays.

Under NCHRP Project 1-41, "Models for Predicting Reflection Cracking of Hot-Mix Asphalt Overlays," Texas A&M Research Foundation of College Station, Texas worked with the objective of identifying or developing mechanistic-based models for predicting reflection cracking in HMA overlays of flexible and rigid pavements and associated computational software for use in mechanistic-empirical procedures for overlay design and analysis. To accomplish this objective, the research reviewed available information relevant to reflection cracking of HMA overlays, considered the factors that contribute to reflection cracking, evaluated available models, and developed mechanistic-based models for predicting the extent and severity of reflection cracking in HMA overlays. In addition, the research developed software, compatible with the MEPDG software, to facilitate use of these models for (1) the design and

analysis of HMA overlays or (2) developing calibration coefficients and enhanced models for specific types of overlays and climatic conditions.

The models developed in this research will be particularly useful to highway agencies because they allow consideration of reflection cracking in the design of HMA overlays and selection of overlays for asphalt and concrete pavements that are expected to yield economic and other benefits. The incorporation of these models into the *AASHTO MEPDG* will help account for the effects of reflection cracking on performance thus improving the analysis and design of HMA overlays of flexible and rigid pavements.

Appendixes A through T contained in the research agency's final report provide detailed information on the different aspects of the research, including user guides to support the software. These appendixes are not published herein but they are available on the *NCHRP Report 669* summary web page at <http://www.trb.org/Main/Blurbs/163988.aspx>.

CONTENTS

1 Chapter 1 Introduction and Research Approach

- 1 Introduction
- 1 Objective
- 1 Scope
- 1 Organization of the Report
- 2 Research Approach
 - 2 Material Properties
 - 3 Traffic
 - 3 Crack Growth and Pavement Temperature
 - 3 Computational Efficiency
 - 3 Calibration to Field Data
 - 4 Use in Design

5 Chapter 2 Findings

- 5 Introduction
- 5 Reflection Cracking – Definition and Mechanisms
- 5 Available Reflection Cracking Models
- 6 Selection of a Reflection Cracking Model
- 7 Process of Constructing a Calibrated Reflection Cracking Model
- 8 Overlay Sections with Sufficient Data for Model Development
- 8 Collection of Pavement Structure Data
- 10 Pavement Distress Data Collection
- 10 Traffic Data Collection
 - 11 Categorization of Traffic Loads
 - 11 Classification of Vehicles
 - 11 Axle Load Distribution Factor
 - 13 Categorizing Traffic Load
- 14 Climatic Data Collection
- 14 Finite Element Method for Calculating SIF
- 17 Method of Predicting SIF
- 19 Traffic Loads and Tire Footprints
 - 19 Tire Patch Length
 - 19 Determination of the Effect of Cumulative Axle Load
 - Distribution on Tire Length
 - 19 Modeling of Cumulative Axle Load Distribution
- 20 Determination of Hourly Number of Axles
 - 20 Probability Density on Tire Patch Length
- 26 Reflection Cracking Amount and Severity Model
 - 27 Calibration of Field Reflection Cracking Model
 - 28 System Identification Process
 - 29 Parameter Adjustment and Adaption Algorithm
 - 30 Calibrating Reflection Cracking Model of Test Sections

33	Prediction of Temperature in a HMA Overlay
33	Heat Transfer in Pavement
34	The Surface Boundary Condition
34	The Bottom Boundary Condition
35	Numerical Solution of the Model
35	Obtaining Hourly Climatic Input Data
35	Stiffness, Tensile Strength, Compliance, and Fracture Properties of Mixtures
36	Artificial Neural Network Algorithms for Witczak's Complex Modulus Models
38	Models of Tensile Strength of Mixtures
38	Models of Paris and Erdogan's Law Fracture Coefficients A and n
39	Healing Coefficients
39	Stress Wave Pattern Correction for Viscoelastic Crack Growth
39	Computational Method for Crack Growth Due to Traffic
41	Computational Method for Viscoelastic Thermal Stresses
42	Supervisory Program to Compute Crack Growth
42	User Interface Program for Input and Output Data
42	Computation-to-Field Calibration Coefficients
44	Validation of the Calibration Coefficients
48	Chapter 3 Interpretations, Appraisal, and Applications
48	Introduction
48	The Model Development Process
48	Mechanistic Prediction of Crack Growth
49	HMA Overlay Material Properties
49	Weather Data and Temperature Prediction
49	Consistent Description of Reflection Cracking Distress
49	Calibration of Calculated Overlay Life to the Observed Distress
50	Calibrated Results Compared with Observed Field Data
50	Calibration Coefficients by Regression Analysis
50	Predictions of Overlay Reflection Cracking
55	Calibration of the Computational Model to Field Data
56	Chapter 4 Summary and Suggested Research
56	Summary
56	Suggested Research
58	References
60	Appendices

AUTHOR ACKNOWLEDGMENTS

The research reported herein was performed under NCHRP Project 1-41 by the Texas Transportation Institute of the Texas A&M University. Robert L. Lytton, Professor of Civil Engineering, was the principal investigator and the co-principal investigator was Fujie Zhou, Research Engineer. The other authors of this report are Fang Ling Tsai and Sang-Ick Lee, both Research Assistants and Sheng Hu and Rong Luo, both Post-Doctoral Research Associates.

The research work was materially aided by the assistance given by Jagannath Mallela and Harold L. von Quintus of the Applied Research Associates, Inc. (ARA), who provided information and data on the New York City overlay test sections. Permission to use that data was given by the City of New York, Department of Design and Construction, Division of Infrastructure. The Texas overlay test section data used in the project were provided by Joe W. Button and Arif Chowdhury of the Texas Transportation Institute with the approval of German Claros, Research Coordinator with the Texas Department of Transportation. The extraction of data and categorization of overlay sections from the Long-Term Pavement Performance database was done by Thomas Freeman of the Texas Transportation Institute. The two programs produced in the project are written in the C# language as was suggested by Gregg Larson of ARA and supported by Vicki Schofield of AASHTO. All subprograms which were not originally in that language were re-written by Sheng Hu of the Texas Transportation Institute. The Artificial Neural Network models of the mixture moduli and the stress intensity factors were provided under a subcontract by Halil Ceylan of Iowa State University. Helpful advice and direction on the use of weather databases was given by Gregg Larson of ARA. The temperature prediction model used in both the design and calibration programs and its description was provided by Charles J. Glover, Professor of Chemical Engineering, Texas A&M University and by Research Assistants Rongbin Han and Xin Jin, both of the Chemical Engineering Department of Texas A&M University. The thermal stress prediction program was provided by Reynaldo Roque of the University of Florida in Gainesville. The finite element program which generated the stress intensity factors which were modeled with the Artificial Neural Network algorithms was written by Sheng Hu, description of that model was written by Sheng Hu, Xiaodi Hu, and Lubinda Walubita, all Post-Doctoral Research Associates and by Fujie Zhou, Research Engineer with the Texas Transportation Institute. The review and evaluation of available reflection cracking models was written by Fujie Zhou. Cathy Bryan of the Texas Transportation Institute was responsible for the final manuscript preparation.

CHAPTER 1

Introduction and Research Approach

Introduction

Reflection cracking is one of the primary forms of distress in hot-mix asphalt (HMA) overlays of flexible and rigid pavements. In addition to affecting ride quality, the penetration of water and debris into these cracks accelerates the deterioration of the overlay and the underlying pavement, thus reducing service life. This project developed mechanistic-based models for use in both analysis and design of HMA overlays. The product of this research will help to account for the effects of reflection cracking on performance, improving the analysis and design of HMA overlays of flexible and rigid pavements.

Objective

The objective of this study was to identify and develop (a) mechanistic-based models for predicting reflection cracking in HMA overlays of flexible and rigid pavements and (b) associated computational software for use in mechanistic-empirical procedures for overlay design and analysis. This chapter summarizes the approach that has been used to accomplish these objectives. The research plan was developed with the expectation that the reflection cracking models and associated software will ultimately be used for routine asphalt overlay thickness design and for reflection cracking performance analysis of asphalt overlay structures. The plan was also guided by the realization that reflection cracking models and associated input must be compatible with the Mechanistic-Empirical Pavement Design Guide (MEPDG) (1), since reflection cracking is only part of the strategic objective of designing reliably performing asphalt overlay pavements. The body of this report describes the approach that was used, the major findings, the interpretation, appraisal and applications of the results of this study, and, finally, the conclusions and suggested further research that would be beneficial to the objectives of this research.

Scope

Because overlays are expected to perform differently in different climatic zones, the Long-Term Pavement Performance (LTPP) database for the four climatic zones (Wet-Freeze, Wet-No Freeze, Dry-Freeze, and Dry-No Freeze) will be reviewed carefully to determine if there are a sufficient number of overlay test sections of a given structural type to warrant developing a set of model coefficients for that type of overlay. As a rule of thumb, a minimum of 20 test sections, all of which have begun to experience reflection cracking, are needed to develop a reliable set of calibration coefficients.

The relationship between this reflection cracking model and the MEPDG software is that of a subprogram which has many of the same inputs and the same format for input screens and output. Figure 1 illustrates how this model is compatible with the MEPDG.

Organization of the Report

This report is organized into four chapters. The first chapter presents the introduction and research approach used in the research project. The second chapter presents the major findings. These include the definition of reflection cracking; a brief review of the available reflection cracking models; criteria for selection of the best presently available model; and a description of the various categories of data and algorithms that were used in assembling the model developed in this project. The data categories include pavement structure, traffic, weather, observed distress, and materials properties. The algorithm categories include methods to predict temperatures; material properties as they vary with temperature and loading rate; thermal stress; traffic stresses and the growth of cracks up from the cracks or joints in the old overlaid pavement. Finally, the second chapter describes how the model predictions are calibrated to the observed field data.

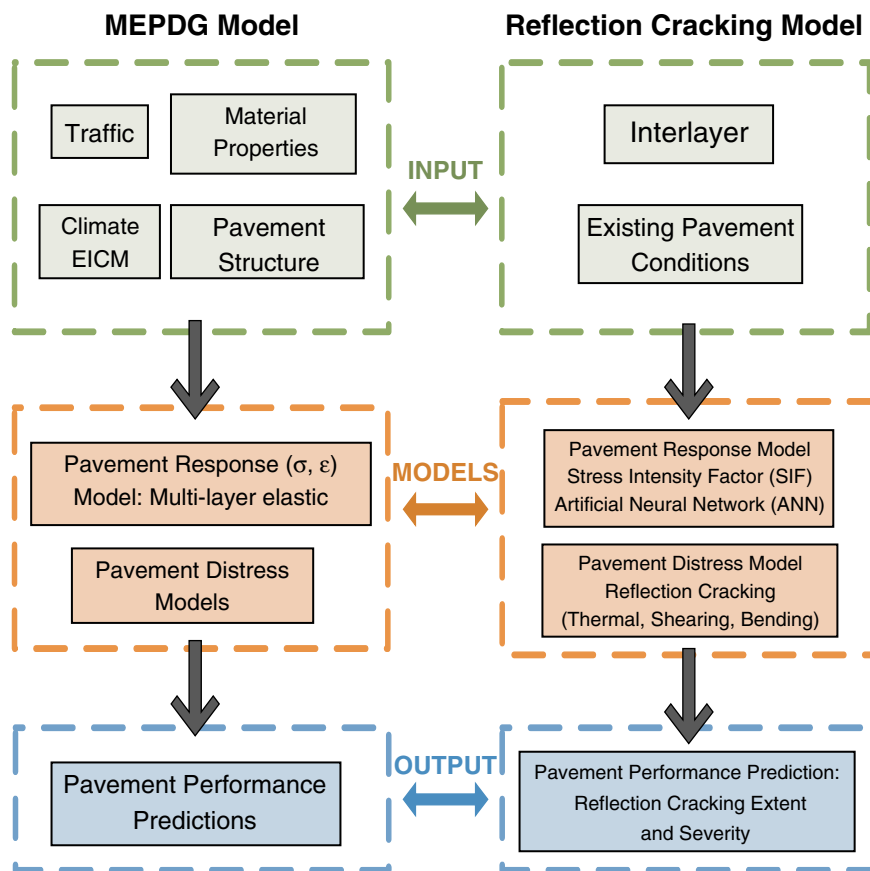


Figure 1. Compatibility of the MEPDG software with the reflection cracking model.

This project has produced two programs: the Design Program and a Calibration Program. The Design Program is written as a subprogram to the existing MEPDG software but is capable of being run separately. The Calibration Program is set up to allow the user to generate a new set of calibration coefficients for any other combination of pavement structure-overlay-climatic zone of special interest to that user. A narrated instructional video has been provided for each program to take the user through the steps of entering the data, running each program, and displaying the output. An interface has been provided so that the calibration coefficients that the user may develop with the Calibration Program can be inserted into the Design Program. The Users' Guides to the Design and Calibration Programs are in Appendices O and P, respectively.

The third chapter presents interpretations, appraisals, and applications of the model that was developed and calibrated. This chapter illustrates how well the calibrated predictions of the S-shaped accumulating distress curves fit the observed distress patterns. It also discusses the level of detail and amount of input data needed for the user of the Calibration Program to develop a new set of calibration coefficients.

The fourth chapter presents conclusions and suggested further research. The main body of this report is written to give

an accurate overview of the approach and results of this project. Much more detailed discussions of the subjects in this report are contained in Appendices A through T. These appendices are not published herein but they are available on the *NCHRP Report 669* summary web page at <http://www.trb.org/Main/Blurbs/163988.aspx>.

Research Approach

A single model that uses fracture mechanics as its basis is sufficient for the analysis of reflection cracking for different overlay types. This is appropriate because the model will consider the difference in the mechanisms of crack propagation and the field calibration coefficients. Three separate mechanisms of crack propagation, thermal, traffic bending, and traffic shearing, were modeled using Artificial Neural Network (ANN) algorithms.

Material Properties

The material properties of the overlay are calculated from the design of the asphalt mix of that overlay using a set of ANN algorithms that replicate Witczak's 1999 (2) and 2006 (3) models of asphalt mixture complex moduli. The input

data required for these models include the properties of the binder, some gradation of the aggregates, and the volumetric composition of the mix. The binder properties may be input in any of the three MEPDG levels:

Level 1: The input for this level will be the six measured values of the master curve of the binder (the glassy shear modulus, the crossover frequency, rheological index, the defining temperature, and the two time-temperature shift function coefficients). The properties of extracted binders that were measured in the Strategic Highway Research Program (SHRP) asphalt studies (4) are summarized in Appendix G.

Level 2: The input will be the PG of the binder and the geographical location of the project. All six binder properties that were measured, tabulated, and reported in the SHRP asphalt studies for a variety of asphalt binders in each of the four principal climatic zones (4) will be used. The program will use the means of the WLF coefficients, defining temperature and crossover frequency for the principal climatic zone where the project is located and then calculate the glassy shear modulus and rheological index from the Performance Grade of the binder.

Level 3: The input will be the geographical location of the project. The mean values of all six master curve properties in the climatic zone where the project is located will be used.

The fracture properties of the overlay mixture are derived from the input properties and the complex moduli neural network algorithms. The design method does not require laboratory tests of the crack growth in a mixture; it allows the user to try numerous variations of a mixture to determine which has the best resistance to reflection cracking. The material properties of the layers of the existing pavement may be input either from a Falling Weight Deflectometer measurement or can be assumed. The growth of cracks due to both thermal and traffic stresses is predicted using the fracture properties for predicting fatigue cracking (4).

Traffic

The daily traffic is input as individual axle loads and is identical to what is required by the MEPDG software for the three levels of input. The user can accept standard traffic distributions that are incorporated into the MEPDG or use traffic data taken from W4 Tables. The load imposed by the tire on the pavement is assumed to result in a rectangular, rather than a circular, uniform pressure distribution.

Crack Growth and Pavement Temperature

The crack growth is calculated each day taking into account the temperature calculated to be at the tip of the crack on that

day. The temperature is computed using U.S. Weather Bureau data that can be accessed readily through websites (5, 6) and Appendix B of this report. The computational model of temperature differs from that used in the MEPDG; it calculates the temperature more accurately than by using in the Enhanced Integrated Climatic Model as part of the MEPDG. It was considered necessary to increase the accuracy of computing the pavement temperature with depth because of the relevance of the thermal stress contribution to the growth of a reflection crack.

Computational Efficiency

Computational efficiency of the software was accomplished by calculating the growth of reflection cracks by the three different mechanisms separately and then combining the number of days that each required to grow vertically all the way through the overlay. Another contributing factor to efficiency in running time was realized by re-programming all of the subprograms from their original language into the C# language which is used in the MEPDG. Additional efficiency was achieved by using ANN algorithms to speed up the frequent calculations of mixture modulus and stress intensity factors that are done each day in a simulated pavement life. The stress intensity factor computations were particularly useful in cutting down on the program running time instead of using finite element calculations for that purpose. The objective of computational efficiency was to reduce the overall program run time down to a minimum as a convenience to the user or this program. The actual run time for a 20 to 30 year pavement life simulation is a matter of seconds and at most a few minutes, depending upon the computer that is used.

Calibration to Field Data

Calibration to field data recognizes that there are three degrees of severity in reflection cracking: low, medium, and severe. Some or all levels of severity may be present on a given pavement section at any time. An S-shaped curve was fit through the field data representing the total length of surface cracks at high (H), high plus medium (MH), and high plus medium plus low levels of cracking severity (LMH). The difference in the total length between any two curves gives the total length of the different levels of distress. Figure 2 illustrates the three cumulative severity curves. Three sets of S-shaped curves were generated with each pavement test section; each curve has a characteristic scale and shape parameter. The scale parameter, ρ , is the number of days required for the crack length to reach 0.368 (1/e) of its maximum length. The shape parameter, β , shows how sharply the curve is rising when it reaches the number of days given

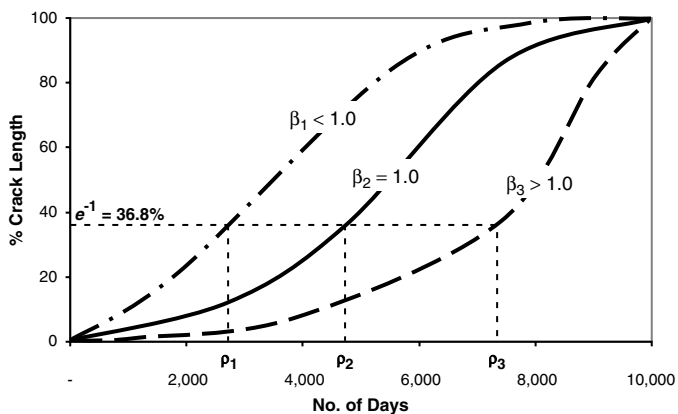


Figure 2. Parameters in reflection cracking severity model.

by the scale parameter, ρ . The three sets of coefficients that are developed for each type of overlay predict the number of days that a given overlay will require to reach the scale points, ρ , on the each of the three distress curves. A detailed discussion of the S-shaped curve and examples from the

field data that were analyzed in this project is provided in Chapter 2, the section entitled “Reflection Cracking Amount and Severity Model.” Appendix L shows how to determine the ρ -value from field data, and makes it possible for a user to develop a set of calibration coefficients. By inserting a set of calibration coefficients into the software, an agency can develop a regional or local version of the overlay analysis model.

Use in Design

The reflection cracking program presented in this report is a tool for designing an overlay. The output from the program shows graphically the rate of reflection cracking length and severity increase with the number of days after construction. The program runs as a subroutine of the MEPDG software, executes a 20-year set of computations in a relatively short time, and allows the trial of a variety of mixture designs, overlay thicknesses, and reinforcing or strain-absorbing interlayers to determine which combination provides the desired service life within acceptable costs.

CHAPTER 2

Findings

Introduction

This report addresses the issues associated with reflection cracking and reports the development of mechanics-based models for use in mechanistic-empirical procedures for the analysis and design of HMA overlays. These mechanics-based models are capable of predicting reflection cracking in HMA overlays of flexible and rigid pavements and incorporate associated computational software for use in mechanistic-empirical procedures for overlay design and analysis.

Reflection Cracking—Definition and Mechanisms

Reflection cracking can be defined as the cracking of a resurfacing or overlay above underlying cracks or joints, with movement of some form in the underlying pavement as its probable cause. As illustrated in Figure 3, this cracking can result from traffic and environmentally induced causes. The existing joints or cracks can affect reflection cracking in two forms (7):

1. The existing joints or cracks provide stress concentration at the bottom of an asphalt overlay, which will lead to the continued crack growth into the asphalt overlay layers.
2. If the stress-concentrating effect of the existing joints or cracks has been nullified by some means, a secondary effect of the existing joints or cracks is that a maximum deflection of the pavement under a wheel load will occur at the crack. Thus, the maximum stresses in the overlay will occur at this point, making it the most likely location for crack growth to initiate as an indirect effect of the existing crack.

Stress concentration, which is the first effect of existing joints or cracks, plays the dominant role in reflection crack-

ing due to the movement in the existing pavements in the vicinity of joints or cracks. This movement may be induced by bending or shearing action resulting from traffic loads or daily and seasonal temperature changes. In general, reflection cracking is caused by the combination of these three mechanisms. Every pass of a traffic load will induce two shearing and one bending effect on the HMA overlay that are affected by the daily temperature (see Figure 4). Thus the combination of all three mechanisms is required to successfully model reflection cracking. In addition, crack initiation and propagation is also influenced by the existing pavement structure (see Figure 5) and conditions, reflection cracking countermeasures (e.g., reinforcing, interlayer), HMA mixture properties, the degree of load transfer at joints and cracks, and others. Therefore, these three mechanisms and these influencing factors must be taken into account in developing a reflection cracking model.

Available Reflection Cracking Models

Concern about reflection cracking of asphalt overlays over existing pavements dates back to 1932, when Gary and Martin (10) studied this problem. Subsequently, many studies have been conducted to address this problem and many models have been developed to analyze or predict reflection cracking. In general, these models can be categorized as follows:

- Empirical model;
- Extended multi-layer linear elastic model;
- Equilibrium equations based models;
- Finite element plus traditional fatigue equation model;
- Finite element plus fracture mechanics model;
- Crack band theory based model;
- Cohesive zone cracking model; and
- Non-local continuum damage mechanics based model.

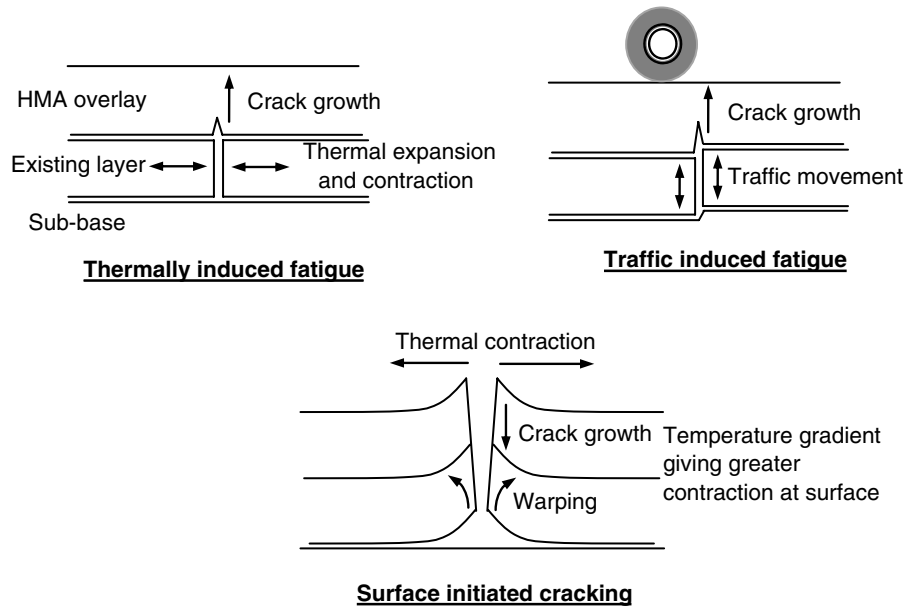


Figure 3. Mechanisms of reflection cracking (8).

Selection of a Reflection Cracking Model

A comprehensive review of available models and their capabilities, advantages, and disadvantages is provided in Appendix R. The review revealed that the finite element plus fracture mechanics model provides the most desirable attributes. The major requirements of the selected model for compatibility with the MEPDG include the following:

- The model must use the same input data as the MEPDG, including the traffic, weather, material properties, and pavement layer geometry.
- The model must be capable of using the same level of computational capability as the present MEPDG (e.g., it should not require the use of a supercomputer).

- The model must be capable of accepting the additional information that distinguishes the reflection cracking mechanisms, i.e., load transfer and crack or joint spacing in the underlying old pavement surface layer.
- The model must be capable of accepting the additional layer geometry associated with the more common overlay configurations and be capable of being enhanced in the future as computational capabilities increase.
- The model must be user friendly, accepting overlay design input data in a graphical format.
- The model must be able to calculate the crack growth potential directly from the input data, and it should permit the consideration of commonly used overlay approaches including interlayers, fabrics, and reinforcing layers.
- The computational time required by the use of the model must be short enough to allow effective use of the time in evaluating alternative overlay designs.

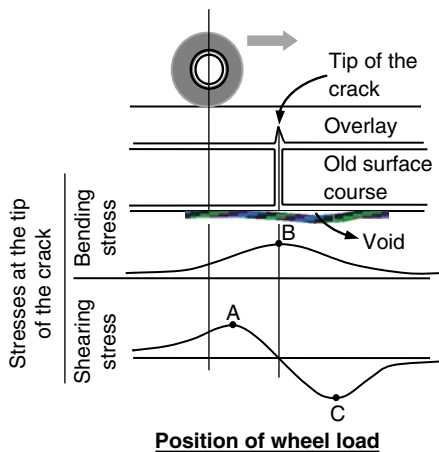


Figure 4. Bending and shear mechanisms (9).

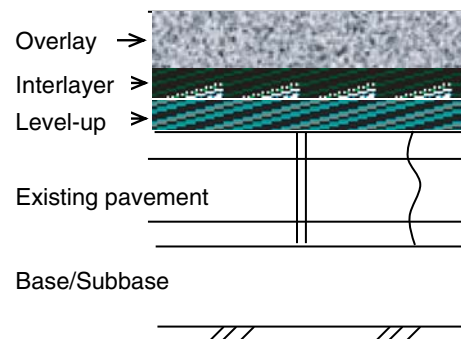


Figure 5. Illustration of an asphalt overlay system.

These compatibility requirements automatically eliminate a number of approaches such as the empirical model, extended multi-layer linear elastic program, equilibrium equations, and advanced models requiring use of supercomputers. While this use may be desirable in the future when super-computer use becomes more widespread and the MEPDG has been converted to such use, it is more desirable at the present to develop a model that uses the level of computational power that is commonly available for state design offices. After considering the different model features and compatibility requirements, the finite element plus fracture mechanics model was selected. However, the running time of a finite element program proved not to provide a practical tool for design so it was decided to incorporate the results of multiple runs into a faster algorithm. Nearly 100,000 runs of a finite element program were made in order to obtain a broad range of computed fracture mechanics results. These numerical results were then incorporated into a total of 18 separate ANN algorithms. These algorithms provide acceptable computational speeds and are the core of the overlay reflection cracking model developed in this project.

The key concept in fracture mechanics is Paris and Erdogan's Law (11) for modeling crack propagation, particularly for fracture-micromechanics applications. Expressed in Equation 1, Paris and Erdogan's Law has been successfully applied to HMA by many researchers, for the analysis of experimental test data and prediction of reflection- and low temperature-cracking (4, 12).

$$\frac{dc}{dN} = A * (\Delta K)^n \quad (1)$$

where

c = the crack length;

N = the number of loading cycles;

A and n = fracture properties of the asphalt mixture; and

ΔK = the SIF amplitude (depends on the stress level, the geometry of the pavement structure, the fracture mode, and crack length).

There are three fracture modes: tensile, shearing, and tearing.

The number of loading cycles, N_f , needed to propagate a crack (initial length, c_0) through the pavement layer thickness, h , can be estimated by numerical integration in the form of Equation 2.

$$N_f = \int_{c_0}^h \frac{dc}{A(\Delta K)^n} \quad (2)$$

Because the SIF is one of the key parameters in Paris and Erdogan's Law, the speed and accuracy of computing SIF values is a very critical aspect of crack propagation analysis and the development of a reflection cracking model.

Process of Constructing a Calibrated Reflection Cracking Model

The process of constructing a calibrated reflection cracking model (Figure 6) involves several steps:

- Select a sufficient number of overlay sections to provide a good likelihood of having a sufficient amount of good quality data (including sequential distress measurements; pavement structure and materials property data; and traffic and weather data) to permit development of a set of calibrated reflection cracking model coefficients. As a rule of thumb, at least 20 such sections are required to develop a complete set of calibration coefficients.
- Collect pavement structure data (including layer thickness, construction dates, and nondestructive testing data on each pavement section) and the mixture design data for the overlay.
- Collect pavement distress data (including the total length of cracking in the old pavement surface prior to overlay and the lengths and levels of severity of reflection cracking) for at least three (preferably more) sets of sequential observations.
- Collect traffic data on each pavement section including the input data used in the MEPDG program (i.e., the traffic load spectrum rather than the total 18-kip equivalent single axle loads).
- Collect climatic data on each of the candidate sections of overlay, including the data needed to accurately calculate the overlay temperature with depth below the surface (i.e., hourly air temperature, solar radiation, and surface reflectance).
- Develop a finite element mechanistic method for calculating the SIF in overlays for thermal, bending, and shearing traffic stresses as a crack grows up through different thicknesses of overlay.
- Develop a numerically accurate and computationally efficient method of predicting the SIF computed by the finite element method.
- Develop a method of dealing with different traffic loads and tire footprints in calculating the SIF.
- Analyze the field distress data into a standard form to represent the total length of reflected cracks that appear with time at the different levels of severity (i.e., low, medium and high). At this point, the number of test sections with actual observed reflection cracking data can be determined (in some cases, not all levels of severity have been observed).
- Develop a method for accurately calculating the hourly and daily temperatures in an overlay at the current tip of the crack.
- Write a program to calculate the stiffness, tensile strength, compliance, and fracture coefficients of the overlay mixture using the mixture properties of volumetric contents of the mixture components, aggregate gradation, and binder master curve characteristics. These properties must be

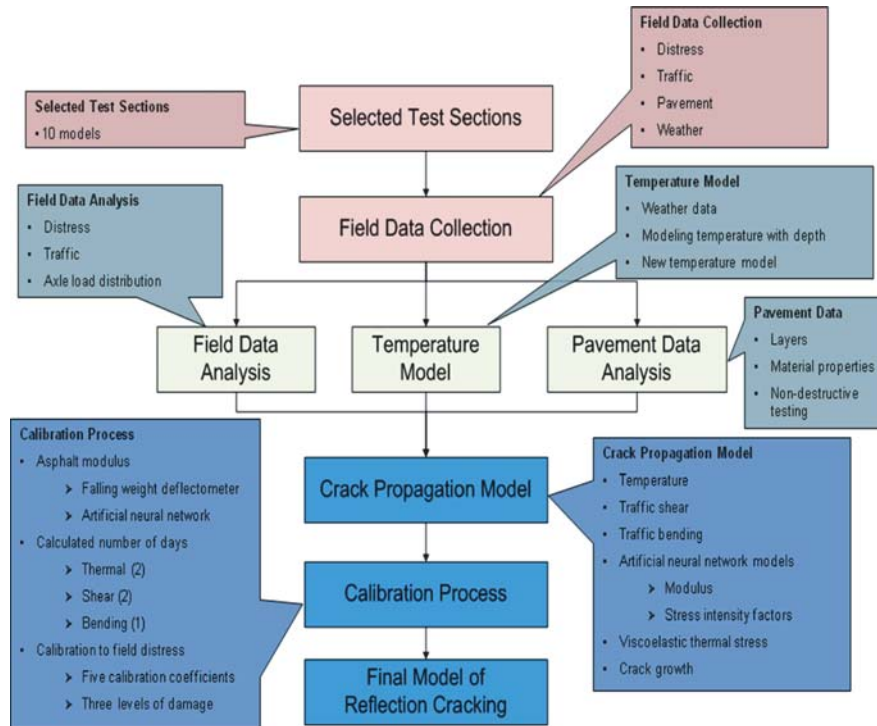


Figure 6. Flow chart of the process of constructing a calibrated reflection cracking model.

computed for the loading times for thermal stresses and the passage of traffic loads representing single, tandem, tridem, and quadrem axles.

- Develop a computational technique for calculating the total crack growth caused by single, tandem, tridem, and quadrem axles passing over a growing crack, and include the healing shift factor that increases with the length of time between traffic loads.
- Develop a program to calculate the viscoelastic thermal stresses in the overlay.
- Develop a computational technique to calculate the growth of a crack caused by daily thermal stresses.
- Write a supervisory program that will combine the computations of crack growth by each of the separate mechanisms (thermal, bending, and shearing).
- Write an interface program to permit the user to input data in the same format used in the MEPDG.
- Calculate the number of days required for each of the three fracture mechanisms to cause a reflection crack to grow through the thickness of the overlay.
- Develop sets of computation-to-field calibration coefficients for each type of pavement-overlay structure and climatic zone.

The work performed in each of these steps to develop the hot-mix overlay reflection cracking model and its calibration coefficients is summarized in the following sections.

Overlay Sections with Sufficient Data for Model Development

After a thorough review of the data available in the LTPP database and for test sections in New York and Texas, the researchers concluded that there is sufficient high quality data to develop sets of calibration coefficients for the reflection cracking model for each major climatic zone in the United States. Data were collected for a total of 11 pavement-structure-overlay-climatic zone sets representing 411 overlay sections, as shown in Table 1.

The LTPP sections provided the bulk of the data that were used for modeling reflection cracking in the different types of pavement structure. The distribution of these sections within the different climatic zones is given in Table 2. The sections were well distributed throughout the United States and Canada, in 37 states, the District of Columbia, and six Canadian provinces as listed in Table 3.

Collection of Pavement Structure Data

The pavement data used were the layer thickness of each pavement layer and the Falling Weight Deflectometer (FWD) data for each test section prior to the placement of the overlay including the temperature at which the FWD data were obtained. The layer moduli of the old pavement were back-

Table 1. Overlay sections for model development.

Data Set	Pavement Structure*	No. of Test Sections	Climatic Zone+
1	AC/mill/AC OL	62	WF
2	AC/mill/AC OL	47	WNF
3	JCP/AC OL	69	WF
4	AC/AC OL	59	WF
5	AC/AC OL	33	WNF
6	AC/SAMI/AC OL	26	WF
7	CRC/AC OL	21	WF
8	AC/AC OL	16	DF
9	AC/mill/AC OL	16	DNF
10	AC/SAMI/AC OL	12	WNF
11	AC/Grid/AC OL	50	NY, Texas
Totals		411	

*The abbreviations are listed in order from the old pavement surface layer upward to the overlay.

- AC = existing hot mix asphalt surface layer,
- JCP = jointed concrete pavement,
- CRC = continuously reinforced concrete surface layer,
- Mill = old surface layer was milled before the overlay was placed.
- SAMI = (Strain Absorbing Membrane Interlayer) indicates that a compliant interlayer was placed between the old surface layer and the hot mix overlay. A reinforcing interlayer was placed between a leveling course and the hot mix overlay.
- AC OL = hot mix asphalt overlay.

+ WF, DF, WNF, and DNF designate Wet-Freeze; Dry Freeze; Wet-No Freeze; and Dry-No Free, respectively

calculated using the program MODULUS (13). The LTPP data included the deflections measured at many equally spaced locations within each test section. The mean of the backcalculated moduli for each layer was used as the modulus of that layer for the entire test section.

In addition to the layer thickness and the backcalculated moduli of the old pavement, the mixture design data of the

overlay was available, including the volumetric composition of the asphalt mixture, the gradation of the aggregate, and some indication of the grade of the asphalt binder. The grade was used to determine the six characteristics of the master curve of the binder according to the CAM model (the glassy shear modulus, G_g , the crossover frequency, ω_R , the rheological index, R , the defining temperature, T_d , and the two time-temperature

Table 2. LTPP test sections used for calibration.

Pavement-Overlay Structure	Description	Total Test Sections	No. of Test Sections at Each Climatic Zone			
			WF	DF	WNF	DNF
AC/AC OL	AC, then AC overlay	108	59	16	33	-
AC/Mill/AC OL	AC, then Mill+AC overlay	125	62	-	47	16
CRC/AC OL	CRC, then AC overlay	21	21	-	-	-
JRC/AC + JPC/AC OL	JRC or JPC, then AC overlay	69	69	-	-	-
AC/SC or FC/AC OL	AC, then seal coat or friction course +AC overlay	38	26	-	12	-
Total		361	237	16	92	16

Table 3. Distribution of LTPP test sections by states.

State	Climate Zone	No. of Sections	State	Climate Zone	No. of Sections	State	Climate Zone	No. of Sections
Alabama	WNF	14	Massachusetts	WF	-	South Dakota	WF	3
Alaska	WF	4	Michigan	WF	12	Tennessee	WF/WNF	4/1
Arizona	DNF	11	Minnesota	WF	21	Texas	DF/ WNF	2/28
Arkansas	WNF	2	Mississippi	WNF	13	Utah	DF	-
California	DNF/WNF	5/3	Missouri	WF	23	Vermont	WF	4
Colorado	DF	9	Montana	DF	-	Virginia	WF/WNF	1/3
Connecticut	WF	6	Nebraska	DF/ WF	-	Washington	DF	1
Delaware	WF	1	Nevada	DF/DNF	-	West Virginia	WF	-
D.C.	WF	1	New Hampshire	WF	1	Wisconsin	WF	20
Florida	WNF	2	New Jersey	WF	21	Wyoming	DF	-
Georgia	WNF	2	New Mexico	DF/DNF	-	Alberta	WF	4
Idaho	DF/WF	-	New York	WF	4	British Columbia	DF	-
Illinois	WF	13	North Carolina	WF/WNF	2/11	Manitoba	WF	9
Indiana	WF	14	Ohio	WF	3	New Brunswick	WF	1
Iowa	WF	10	Oklahoma	WF/WNF	1/11	Nova Scotia	WF	-
Kansas	WF	13	Oregon	WNF	1	Ontario	WF	3
Kentucky	WF	2	Pennsylvania	WF	7	Quebec	WF	9
Maine	WF	6	Rhode Island	WF	-	Saskatchewan	DF	4
Maryland	WF	14	South Carolina	WNF	1	-	-	-

shift coefficients, C_1 and C_2). The method of making this conversion is explained in Appendix G. These six properties of the master curve of extracted binders were measured and reported in SHRP studies (4) and tabulated in Appendix G. This information was used together with the calculated temperature to determine the input to the ANN models of Witczak's 1999 (2) and 2006 (3) models of the complex modulus.

The overlay test sections in Texas and New York City contributed high quality data and the unique feature of having the overlays reinforced by geosynthetic interlayers.

Pavement Distress Data Collection

The pavement distress data included the total length and severity of the cracks in the old pavement surface prior to the placement of the overlay and the length and severity of the cracks reflected through the overlay. Only transverse cracks were considered as reflection cracks in each test section. In

order to have reliable ρ and β values for the S-shaped curves that were fitted to the distress data, at least three separate and sequential observations of distress were required. In some cases, no distress data were recorded on the old pavement surface prior to overlay and a mathematical method had to be devised to estimate the original amount of cracking which was subject to reflection. The mathematical method used was the Systems Identification method which is described in detail subsequently in this chapter and also in Appendix L.

Traffic Data Collection

Traffic data is a key element for the design and analysis of a HMA overlay structure or a new pavement structure. For compatibility with the MEPDG, traffic was described by the actual load distribution (spectrum) for each axle type (single, tandem, tridem, or quadrem axle) for each vehicle (truck) class or number of tires (single or dual).

The daily traffic distribution data was determined based on the traffic data collected in the field over the years. However, it was found that some sections did not have enough field data to determine the traffic characteristics, while others had complete historical traffic data. In order to consider the level of collected traffic data, a hierarchical approach was adopted in the MEPDG and also is used in this project. The three levels were defined based on the availability of collected traffic data and Weigh-In-Motion (WIM) data which is used to determine the normalized axle load distribution for each axle and vehicle types (14):

- Level 1: Very good knowledge of past and future traffic characteristics and site/segment specific WIM data;
- Level 2: Modest knowledge of past and future traffic characteristics and regional default summaries WIM data; and
- Level 3: Poor knowledge of past and future traffic characteristics and national default summaries WIM data or only Average Annual Daily Truck Traffic (AADTT) available.

Categorization of Traffic Loads

In order to analyze traffic load effects for reflection cracking, the annual number of axle loads for each vehicle class and axle type were entered in the analysis process. The number of axle loads was determined using the traffic load categorized based on the FHWA vehicle class, the axle type, and the number of tires (details of this process are found in Appendix C).

Classification of Vehicles

FHWA defines vehicles into 13 classes, as shown in Table 4, depending on whether they carry passengers or commodities.

Nonpassenger vehicles (class 4 to class 13) are divided by the number of axles and the trailer units (15). Although a bus (vehicle class 4) is a passenger vehicle, the term truck traffic applies to the load level and includes both trucks and buses since the proportion of buses in the traffic flow is relatively small (16).

Because the light axle load groups, such as vehicle classes 1 to 3, do not have significant effects on load related distresses, the traffic analysis in this study considered only the heavier load groups (i.e., classes 4 to 13).

Axle Load Distribution Factor

The axle load distribution is defined as the classification of traffic loading in terms of the number of load applications by each axle type (single, tandem, tridem, or quadrem) within a given range of axle load. The axle load distribution factor is the percentage of the total axle applications in each load interval by an axle type for a specific vehicle class (classes 4 to 13) (14, 17). The load ranges and intervals for each axle type are listed in Table 5.

The determination of the axle load distribution requires WIM data, which is the number of axles measured within each axle load range by axle types of each vehicle class. LTPP guidelines require that the vehicle axle weights should be collected using a WIM sensor by vehicle classes, type of axle, and axle load intervals. Using measured WIM data, the distribution is calculated by averaging the number of axles measured within each load interval of an axle type for a vehicle class divided by the total number of axles for all load intervals for a given vehicle class. The normalized axle load distribution factors should total 100 for each axle type within each truck class. Table 6 presents an example of FHWA W-4 Truck

Table 4. FHWA vehicle classification.










Vehicle Class	Schema	Description
4		Buses
5		Two-axle, single-unit trucks
6		Three-axle, single-unit trucks
7		Four-axle or more than four-axle single-unit trucks
8		Four-axle or less than four-axle single trailer trucks
9		Five-axle single trailer trucks
10		Six-axle or more than six-axle single trailer trucks
11		Five-axle or less than five-axle multi-trailer trucks
12		Six-axle multi-trailer trucks
13	—	Seven-axle or more than seven-axle multi-trailer trucks

Table 5. Load intervals for each axle type.

Axle Type	Axle Load Interval
Single Axles	3,000 ~ 40,000 lb at 1,000 lb intervals
Tandem Axles	6,000 ~ 80,000 lb at 2,000 lb intervals
Tridem Axles	12,000 ~ 102,000 lb at 3,000 lb intervals
Quad Axles	

Table 6. Number of single axle loads for vehicle class 4 to 7 (LTPP Section 180901 in 2004).

Axle Load (lb)	Vehicle Class			
	4	5	6	7
3,000	0	53,818	183	11
4,000	10	54,606	558	52
5,000	42	39,113	993	139
6,000	175	20,289	1,099	168
7,000	988	24,555	2,426	252
8,000	10,687	22,491	5,617	298
9,000	9,713	13,719	8,154	365
10,000	10,156	12,839	12,423	879
11,000	6,011	7,127	8,945	1,516
12,000	5,875	6,413	7,725	2,913
13,000	3,409	3,511	3,257	2,464
14,000	2,947	3,128	2,289	2,710
15,000	1,640	1,756	975	1,740
16,000	1,239	1,513	725	1,419
17,000	679	834	285	664
18,000	446	800	235	423
19,000	212	424	104	159
20,000	181	360	73	111
21,000	106	261	44	70
22,000	51	131	22	46
23,000	41	135	6	26
24,000	21	85	4	9
25,000	24	90	3	12
26,000	11	43	1	7
27,000	4	33	1	2
28,000	1	12	3	1
29,000	4	25	0	1
30,000	3	13	0	0
31,000	1	16	2	0
32,000	2	8	0	0
33,000	0	5	0	0
34,000	0	2	1	0
35,000	0	0	0	0
36,000	0	0	0	0
37,000	0	2	0	0
38,000	0	0	0	0
39,000	0	0	0	0
40,000	0	0	0	0
Total	54,679	268,157	56,153	16,457

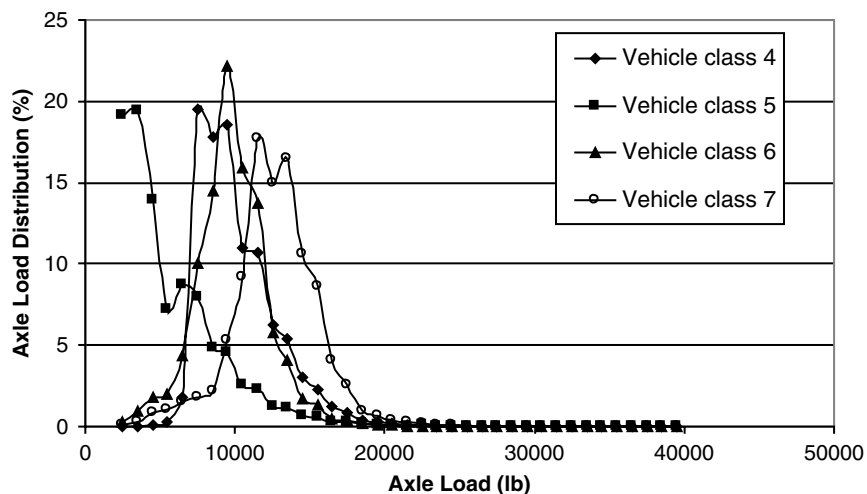


Figure 7. Annual normalized single axle load distribution for vehicle class 4 to 7 (LTPP Section 180901 in 2004).

Weight Tables in which WIM data are typically reported for vehicle classes 4, 5, 6, and 7 for LTPP test section 180901 in 2004. Figure 7 shows the annual normalized single axle load distribution calculated using the data in Table 6.

Categorizing Traffic Load

In this study, the traffic loads were categorized based on the vehicle class, axle type, and number of tires to facilitate the analysis of load effects for reflection cracking. Every truck in each vehicle class has single, tandem, tridem, or/and quadrem

axles, and each axle has single or dual tires. Table 7 lists the number of axles for each axle type and vehicle class.

All axles of vehicle classes 4 and 5 and single axles of class 6 and 7 vehicles have single tires while the others have dual tires. Thus the matrix of vehicle class and axle types can be categorized according to the number of tires. When the steering and non-steering axles are put together in the single axle type, the matrix can be characterized into eight categories based on the vehicle class, the axle type, and the number of tires. The total number of axle loads for each category was used to determine the axle load distribution factor for the

Table 7. Number of axles for each vehicle class.

Vehicle Class	Number of Axles			
	Single*	Tandem	Tridem	Quadrem
4	1	1		
5	2 (1)			
6	1	1		
7	1		1	
8	3 (2)			
9	1	2		
10	1	1	1	
11	5 (4)			
12	4 (3)	1		
13	3 (2)	2		

The number of nonsteering single axles are shown in parentheses.

Shaded areas are vehicle classes that use single tires; unshaded areas are vehicle classes that use dual tires.

Table 8. Vehicle class related to axle and tire categories.

Vehicle Class	Single Axle	Tandem Axle	Tridem Axle	Quad Axle
4	1	3	5	7
5		Single Tire		
6		Dual Tire		
7	2	4	6	8
8				
9				
10				
11				
12				
13				
14				

Shaded areas are vehicle classes that use single tires; unshaded areas are vehicle classes that use dual tires.

analysis of the traffic load effect on reflection cracking. Table 8 shows the categorization of the axles of each vehicle class based on tire configuration. Categories 1, 3, 5, and 7 have single tires and the categories 2, 4, 6, and 8 have dual tires. These eight categories are used in calculating the traffic stresses which are partly the cause of reflection cracking.

Climatic Data Collection

The climatic data were collected from two principal sources in addition to the LTPP database. The hourly solar radiation and the daily air temperature and wind speed were needed to make accurate estimates of the temperature in the overlay. In addition to these data, the temperature model requires the albedo of the pavement surface, its thermal conductivity, and emissivity and absorption coefficients. The solar radiation data can be obtained from the internet at METSTAT Model (Meteorological–Statistical Solar Model) and the SUNY Model for the State University of New York at Albany (http://rredc.nrel.gov/solar/old_data/nsrdb/). The daily climate data on air temperature and wind speed can be found at <http://www.ltpo-products.com/DataPave/>. It was necessary to develop a different temperature model than the one contained in the Enhanced Integrated Climatic Model (EICM) in order to calculate the temperatures to a higher degree of accuracy (more detail is provided in Appendix B).

Although temperatures predicted with the EICM model satisfy pavement design needs in general, there have been some large differences when compared to measured pavement temperature (18). These differences are most likely caused by the

assumption that heat fluxes at the pavement surface are exactly balanced by conduction into the ground well below the surface; inaccuracy of climatic data (especially calculated solar radiation); and the assumptions of the constant temperature boundary condition and site-independent model parameter values.

Recently, significant improvement over the EICM model has been achieved by several groups using a similar one-dimensional heat transfer model, but with an unsteady-state surface heat flux boundary condition, measured model input data, and site-specific model parameters that were optimized based on measured pavement temperatures (19, 20, 21).

Figure 8 presents a comparison of the temperatures measured at different depths below the pavement surface with those calculated with the EICM model (18).

Figure 9 shows a comparison between the measured temperatures and those calculated with the new model used in this project (the model is described later in this chapter: details are provided in Appendix B).

The one dimensional heat transfer model employs an unsteady-state heat flux boundary condition at the pavement surface, a depth-independent heat flux 3 m below the surface, and the ability to estimate site-specific model parameters using known measured pavement temperatures.

Finite Element Method for Calculating SIF

In this project, it was found that the computational time to calculate new stress intensity factors using the finite element method at the daily location of the tip of the crack was too

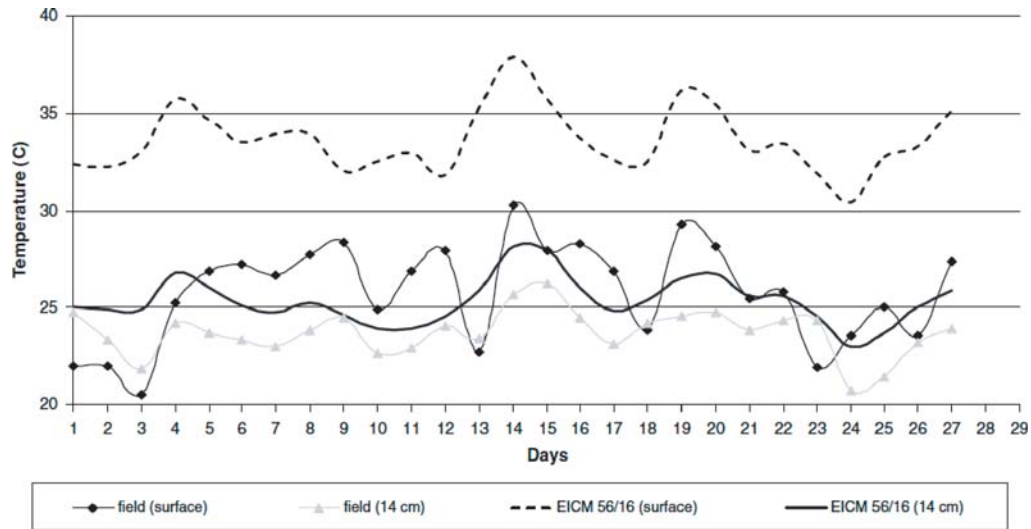


Figure 8. Typical daily pavement temperature prediction using EICM model (18).

long. Therefore a method was adopted to calculate the SIF for a wide variety of conditions, pavement structures, and crack lengths using a finite element method and then to model the computed results with the computationally efficient ANN algorithm (the method used to generate these sets of SIF is presented in detail in Appendix Q).

The finite element method is a two-dimensional method which uses Fourier Series to represent the effects of loads that act at some distance from the two-dimensional plane where the calculations are made (details are provided in Appendix Q). A comparison of the results obtained using this method with the results obtained using a true three-dimensional finite element program revealed differences of 2 to 5 percent. Use of a two-dimensional finite element program was ruled out because of the long computational time it required (the time required for a three-dimensional program is of course much greater).

The following six basic pavement structures were used in the computations:

- Asphalt overlay over cracked asphalt surface;
- Asphalt overlay over compliant interlayer (SAMI) over cracked asphalt surface;
- Asphalt overlay with reinforcing geosynthetic layer over cracked asphalt surface;
- Asphalt overlay over jointed concrete surface;
- Asphalt overlay with reinforcing geosynthetic layer over jointed concrete surface; and
- Asphalt overlay over cracked continuously reinforced concrete surface.

The following three different loading conditions were used in the finite element calculations of the SIF at the tip of the crack:

- Thermal stress;
- Bending stress due to traffic; and
- Shearing stress due to traffic.

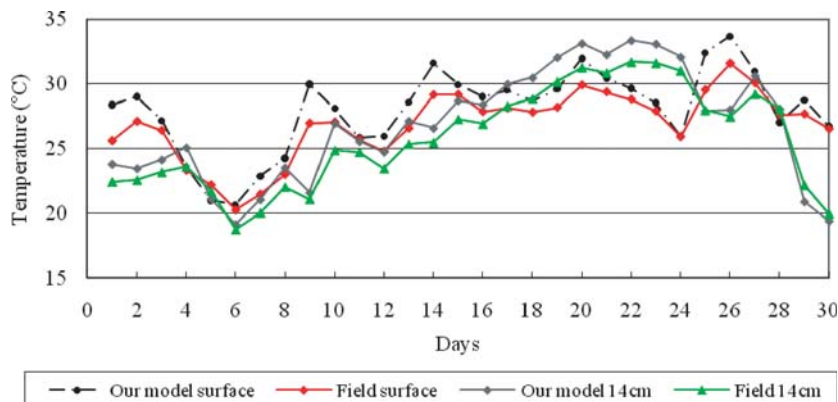


Figure 9. Typical daily pavement temperature prediction using improved model.

Table 9. Number of computer runs of SIF.

Pavement Structures	Number of Test Sections	Computer Runs of Stress Intensity Factors with Varying Crack Lengths		
		Thermal	Shear	Bending
AC/AC OL	233	1,620	25,920	4,320
JCP/AC OL	69	14,580	25,920	4,320
AC/SAMI/AC OL	38	6,480	-	-
AC/GRID/AC OL	50	9,720	-	-
CRC/AC OL	21	1,620	-	-

The following two tire and axles configurations were included in the traffic stress finite element computations:

- Single axle, single tire
- Single axle, dual tire

Collateral studies with multiple axles showed that the SIF beneath one axle is affected by the loads of other axles at standard axle spacings by no more than about 10 percent. This effect was included in the computations of the SIF for tandem, tridem, and quadrem axles.

Table 9 lists the pavement structures and the number of computer runs performed for developing the SIF. The total number of computer runs was 94,500. The number of bending SIF computations was reduced because the bending stresses become compressive only a short distance into the overlay.

The variables included in the finite element computational runs were the layer thickness, modulus of overlay, surface layer, and base course and the crack or joint spacing. In the thermal stress cases, different levels of thermal expansion coefficient were used. With the jointed concrete pavement structures, different levels of load transfer efficiency were used. For those

cases where a compliant interlayer (SAMI) was used, the thickness and modulus of that layer were also varied. In those pavement structures in which reinforcing geosynthetics were used, the thickness and the grid stiffness were used. Because there are no uniform industry standards for specifying the properties of these commercially available products, three levels of geosynthetic stiffness (high, medium, and low) were used in the computer runs. The appropriate level can be chosen by the user by referring to the graph in Figure 10. The user will calculate the reinforcing product stiffness (in MN-mm/m² units) and enter the value on the graph in Figure 10 at the corresponding reinforcing product thickness (in mm). The curved line that is closest to this point provides the stiffness level that should be used as input to the design program.

For a geo-grid, the stiffness is computed from its geometric and material properties as Ea/s where E is the material modulus (MN/m²); a is the rib cross-sectional area, (mm²); s is the rib spacing (mm); and t is the vertical rib thickness (mm). If the reinforcing material is a sheet instead of a grid, then the overlay reinforcing stiffness in MN-mm/m² is calculated as Et .

Successful use of geo-grids as reinforcing interlayers depends upon embedding the grid within the overlay so that there is

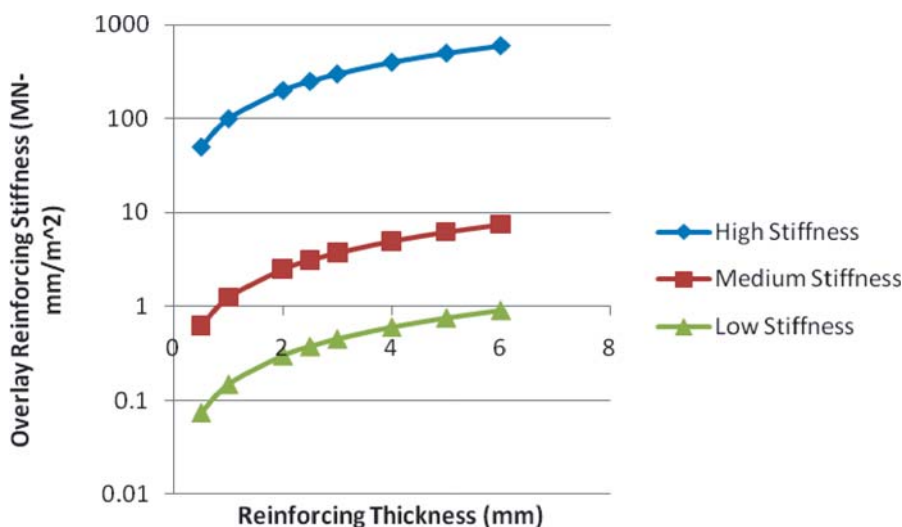


Figure 10. Overlay reinforcing stiffness versus reinforcing thickness.

aggregate interpenetration through the grid from above and below to lock the grid into place. The grid will provide no reinforcing function if there is slippage between the grid and the overlay material. For this reason, in all finite element runs the reinforcing interlayer was placed within the overlay on top of a leveling course.

Method of Predicting SIF

The method chosen to model the computed results from the finite element runs was the ANN algorithm. The formulation of an accurate and computationally efficient algorithm using the ANN approach is described in the literature (22, 23, 24). The final model is a multi-layered equation which can achieve very good fits to the original data. A total of 18 different ANN models were constructed for use in this program (see Table 10). Details of the ANN models of SIF for the different pavement structure and thermal and traffic cases is provided in Appendix F, including graphs of the computed SIF versus those predicted by the ANN algorithms. The coefficient of determination (R^2) of all of these models was above 0.99 except for one case of pure bending in an asphalt overlay over a jointed concrete pavement. For this model, the R^2 value was 0.83 because tensile stresses rarely occur in asphalt overlays due to pure bending and as a consequence there were very few data points.

As noted in Table 10, ANN Models 1, 2, and 3 provide different degrees of interlayer slip between the overlay and the

underlying old asphalt surface for the thermal stress case. ANN Model 4 provides a compliant interlayer (SAMI) between the overlay and the old asphalt surface layer for the thermal stress case. Model 5 provides a no-slip condition between the overlay and the underlying old asphalt surface for the thermal stress case. Model 6 provides a no-slip condition between the overlay and an underlying jointed concrete pavement for the thermal stress case. ANN Models 7 through 12 provide the Bending SIF for a tire located directly above the crack or joint in the old pavement surface; dual and single tire models are provided. ANN Models 13 through 18 provide the Shearing and Bending SIF that occur when the leading or trailing edge of the tire is above the crack or joint in the old pavement surface layer; both dual and single tire models are provided. The ANN Models 8, 10, and 12 are designated by the term “Only Positive” (i.e., only tensile SIF are modeled). This condition occurs when the crack is still small and in the bottom part of the overlay. Negative SIF can be calculated and occur in compressive stress areas where cracks will not grow. Figure 11 shows the different pavement structures and traffic or thermal stress cases that apply to each ANN model.

An example of the fit of an ANN model to the SIF data that was calculated by the finite element program is given in Figure 12 for the case of thermal stress in a HMA overlay over an old cracked asphalt pavement surface for which the R^2 was 0.9982. Appendix F provides similar graphs for all of ANN models and describes the variations and ranges of overlay pavement structure and the material and interface properties used

Table 10. Artificial neural network models for stress intensity factors.

Model No	Model Name	Load Case
1	AC_over_AC_Interlayer_slip_L	Thermal
2	AC_over_AC_Interlayer_slip_M	Thermal
3	AC_over_AC_Interlayer_slip_H	Thermal
4	AC_SC_AC	Thermal
5	AC_over_AC	Thermal
6	AC_over_PCC	Thermal
7	Pure_Bending_AC_over_AC_Dual_Tire_Together	Traffic
8	Pure_Bending_AC_over_AC_Dual_Tire_Together_Only_Positive	Traffic
9	Pure_Bending_AC_over_AC_Single_Tire_Together	Traffic
10	Pure_Bending_AC_over_AC_Single_Tire_Together_Only_Positive	Traffic
11	Pure_Bending_AC_over_PCC_Single_Tire_Together	Traffic
12	Pure_Bending_AC_over_PCC_Single_Tire_Together_Only_Positive	Traffic
13	AC_Over_AC_Shearing_Bend_Part_Dual_Tire	Traffic
14	AC_Over_AC_Shearing_Shear_Part_Dual_Tire	Traffic
15	AC_Over_PCC_Shearing_Shear_Part_Dual_Tire	Traffic
16	AC_Over_AC_Shearing_Bend_Part_Single_Tire	Traffic
17	AC_Over_AC_Shearing_Shear_Part_Single_Tire	Traffic
18	AC_Over_PCC_Shearing_Shear_Part_Single_Tire	Traffic

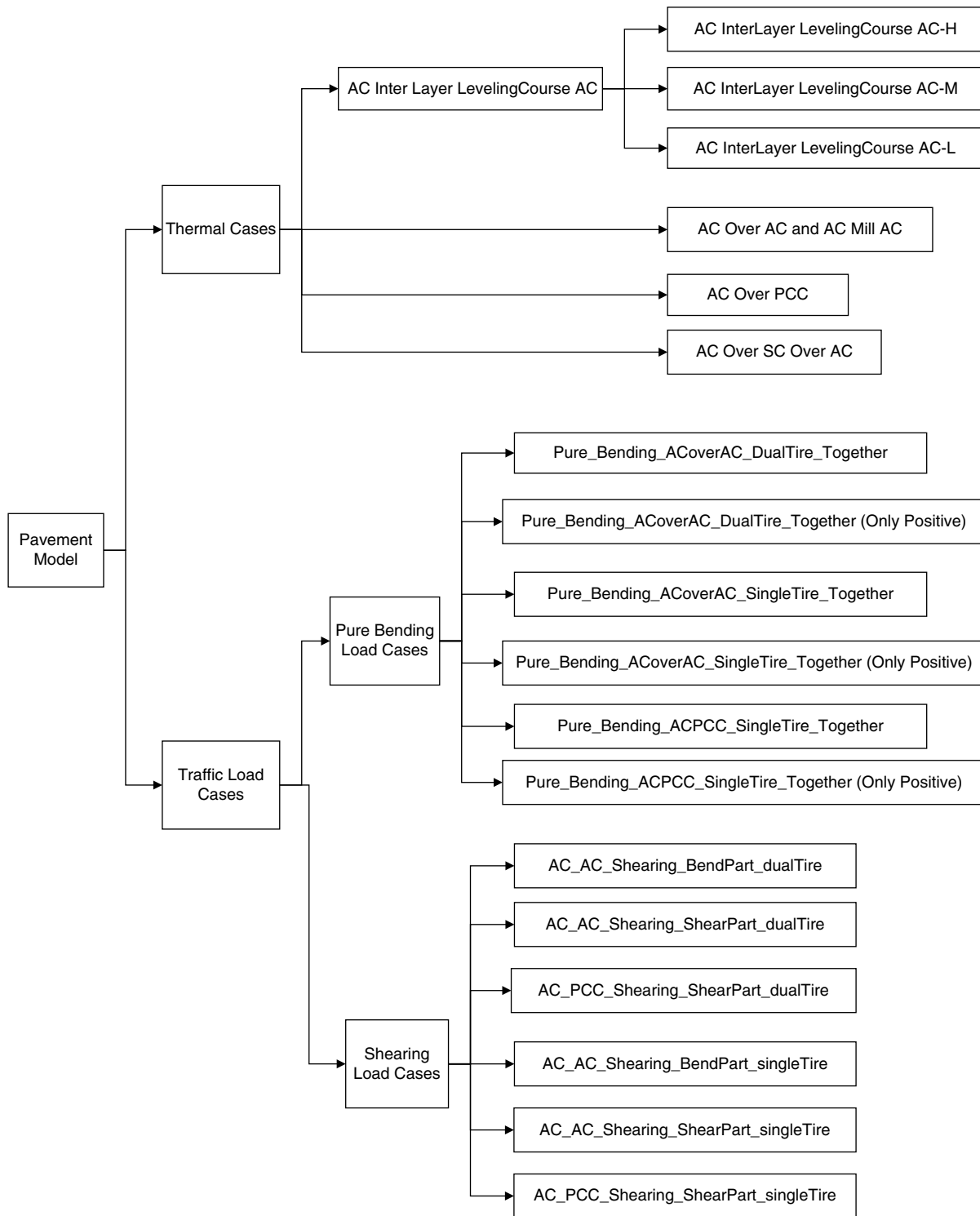


Figure 11. ANN models applications to overlaid pavement structures.

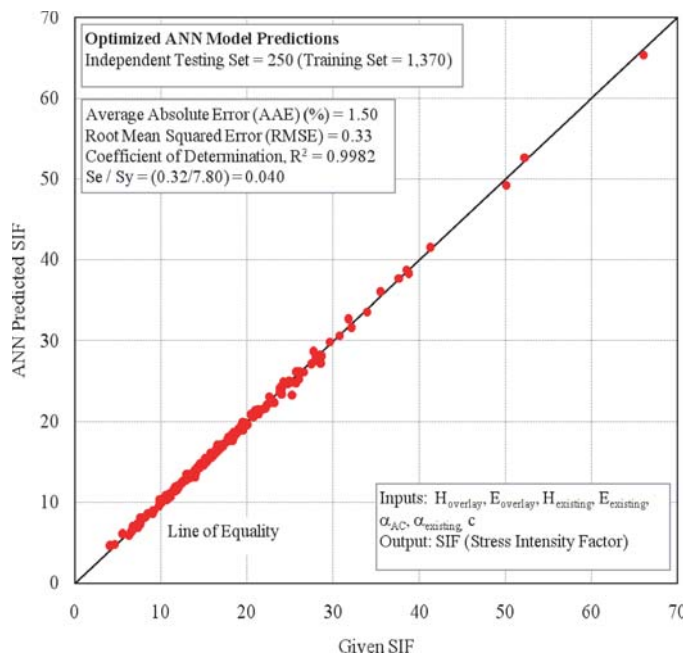


Figure 12. Comparison of SIF with ANN model predictions for HMA overlays over a cracked asphalt pavement surface layer.

in developing the models. These models apply only to the variable ranges used as input to these models; extrapolation outside the range of inference may not produce accurate results.

Traffic Loads and Tire Footprints

Tire footprints are closer to rectangles than to the commonly assumed circular footprints (25). In this project, rectangular tire footprints with known tire widths were used; tire footprint length was calculated from the tire load and the inflation pressure. The length of tire patch was used to evaluate bending and shearing SIF in asphalt overlays. Also, because the tire length is proportional to the load, a cumulative axle load distribution on tire length for each category may be determined, based on collected traffic data such as WIM or AADTT.

Tire Patch Length

The tire-load model that assumes a rectangular tire contact area (as shown in Figure 13) was used to evaluate the effect of tire load on reflection cracking.

Tire width is assumed to be constant within each traffic category (vehicle class and axle type) even under different tire pressures. Thus, the tire length can be calculated as follows:

$$\text{Tire Length (in.)} = \frac{\text{tire load (lb)}}{\text{tire pressure} \left(\frac{\text{lb}}{\text{in.}^2} \right) \times \text{tire width (in.)}} \quad (3)$$

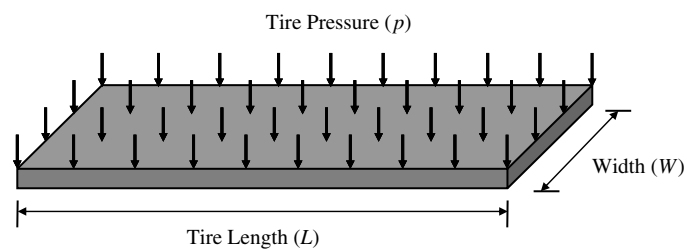


Figure 13. Tire load applied to pavement surface.

Determination of the Effect of Cumulative Axle Load Distribution on Tire Length

Because of the difficulty of employing each tire length for axle load intervals to evaluate traffic load effects on propagation of reflection cracking, the effect of the axle load distribution on the tire patch length for each category was used for the evaluation of traffic load. The axle load distribution intervals can be converted into tire length intervals using the characteristics of each axle type presented in Table 11.

The tire patch lengths of corresponding axle load intervals for each category can be calculated using Equation 3 and the characteristics of axle types. Table 11 lists the calculated axle load intervals for all traffic categories, and Table 12 lists the tire patch length increments.

Using the tire patch length and collected traffic data, the cumulative axle load distribution can be determined for each category. Figure 14 illustrates the procedure for determining tire length and the cumulative axle load distribution (CALD) of each category. Such distribution should be produced for all eight traffic categories to account for all types of vehicles and axles.

Figure 15 shows the cumulative axle load distribution of tire load for Category 1 of LTTP section 180901 in 2004, which was determined using data in Table 12.

Modeling of Cumulative Axle Load Distribution

Since the frequency distribution of each tire length of a load category is used to evaluate load effects for reflection cracking propagation, the cumulative axle load distribution (CALD) of pavement sections and traffic categories should be developed along with the tire length. The CALD of traffic loads or tire lengths follows a sigmoidal curve having a lower asymptote of zero and a finite upper asymptote as shown in Figure 16. (Details of the modeling process are provided in Appendix D).

After reviewing potential models that describe the statistical properties of the cumulative axle load distribution versus tire length, the Gompertz model presented in Equation 4, was chosen.

$$y = \alpha \exp[-\exp(\beta - \gamma x)] \quad (4)$$

where α , β , and γ are model parameters.

Table 11. Typical characteristics for axle types (24).

Category	Axle Type	Tires	Tire Width (in.)	Tire Pressure (PSI)	Axle Load Interval (lb)
1	Single	Single	7.874	40 (< 6,000 lb) 120 (> 6,000 lb)	3,000 ~ 40,000 lb at 1,000 lb intervals
2		Dual	8.740		
3	Tandem	Single	7.874	120	6,000 ~ 80,000 lb at 2,000 lb intervals
4		Dual	8.740	120	
5	Tridem	Single	7.874	120	12,000 ~ 102,000 lb at 3,000 lb intervals
6		Dual	8.740	120	
7	Quadrem	Single	7.874	120	12,000 ~ 102,000 lb at 3,000 lb intervals
8		Dual	8.740	120	

The Gompertz model is appropriate because it has a clear physical boundary condition which shows asymptotes at $y = 0$ and $y = \alpha$ and is asymmetric about its inflection point which occurs at β/γ (26). The parameter α in the model indicates the upper asymptote which is equal to 1.00 (100%) for the cumulative axle load distribution curve. The parameter β describes how wide the rising portion of the curve is. In addition, the parameter γ indicates the slope of the cumulative axle load distribution curve. Figure 17 illustrates a typical curve of the Gompertz model.

The parameter α should be equal to 1.00 because the cumulative axle load distribution curve has a physical boundary condition ranging from 0 to 1.00 (i.e., 0 to 100 percent). Therefore, the modified model for cumulative axle load distribution is:

$$C(L_i)_j = \exp[-\exp(\beta - \gamma L_{ij})] \quad (5)$$

where

L_{ij} = i th tire length in tire patch length increment in traffic category j ;

$C(L_i)_j$ = cumulative axle load distribution factor at L_i within traffic category j ; and

β, γ = model parameters describing the curve width and slope, respectively.

The collected traffic data from WIM or AADTT for a given section were used to develop the model parameters β and γ in the modified Gompertz model of Equation 5. The results provided a good fit of the data along with relatively high significance. Table 13 lists the developed model parameters β and γ for the traffic category 1 of LTPP Section 180901. Typical model parameters for each traffic category are presented in Table 14.

Figure 18 shows a plot of the calibrated model data and the corresponding measured traffic data for the LTPP section.

The distribution factor of C_1 represents the minimum axle load (tire length) to be considered for load related distress. The lower limits of axle load and tire length are presented in Table 15. C_2 is the factor at which the cumulative distribution reaches 100 percent first. L_1 and L_2 are the tire lengths corresponding to C_1 and C_2 , respectively. The model parameters and plots of calibrated cumulative axle load distribution versus tire lengths for all categories of Section 180901 are provided in Appendix A.

For Level 1 data inputs, the model parameters for the cumulative axle load distribution can be computed using WIM data for each category, while the default values for Level 3 input are provided. The default model parameters, shown in Table 14, were prepared using traffic data from the LTPP database. Also, Table 16 presents the default CALD values which were determined based on the model parameter default values.

Determination of Hourly Number of Axles

In order to analyze reflection cracking propagation caused by bending or shearing, the hourly number of axles should be considered in each of the tire length increments within each traffic category. The number of axles can be calculated from the probability density which is determined based on the cumulative axle load distribution of tire lengths in each category (details of the process of determining the hourly traffic distribution are provided in Appendix E).

Probability Density on Tire Patch Length

The probability density of the tire patch length is the frequency distribution of each tire length in a category, which is required to determine the number of traffic loads during

Table 12. Tire patch length increment for traffic categories (inches).

Tire Patch Length	Traffic Category							
	1	2	3	4	5	6	7	8
1	3.704	1.669	1.588	0.715	2.117	0.953	1.588	0.715
2	4.233	1.907	2.117	0.953	2.646	1.192	1.984	0.894
3	4.763	2.145	2.646	1.192	3.175	1.430	2.381	1.073
4	5.292	2.384	3.175	1.430	3.704	1.669	2.778	1.251
5	5.821	2.622	3.704	1.669	4.233	1.907	3.175	1.430
6	6.350	2.860	4.233	1.907	4.763	2.145	3.572	1.609
7	6.879	3.099	4.763	2.145	5.292	2.384	3.969	1.788
8	7.408	3.337	5.292	2.384	5.821	2.622	4.366	1.967
9	7.938	3.576	5.821	2.622	6.350	2.860	4.763	2.145
10	8.467	3.814	6.350	2.860	6.879	3.099	5.159	2.324
11	8.996	4.052	6.879	3.099	7.408	3.337	5.556	2.503
12	9.525	4.291	7.408	3.337	7.938	3.576	5.953	2.682
13	10.054	4.529	7.938	3.576	8.467	3.814	6.350	2.860
14	10.583	4.767	8.467	3.814	8.996	4.052	6.747	3.039
15	11.113	5.006	8.996	4.052	9.525	4.291	7.144	3.218
16	11.642	5.244	9.525	4.291	10.054	4.529	7.541	3.397
17	12.171	5.482	10.054	4.529	10.583	4.767	7.938	3.576
18	12.700	5.721	10.583	4.767	11.113	5.006	8.334	3.754
19	13.229	5.959	11.113	5.006	11.642	5.244	8.731	3.933
20	13.758	6.198	11.642	5.244	12.171	5.482	9.128	4.112
21	14.288	6.436	12.171	5.482	12.700	5.721	9.525	4.291
22	14.817	6.674	12.700	5.721	13.229	5.959	9.922	4.469
23	15.346	6.913	13.229	5.959	13.758	6.198	10.319	4.648
24	15.875	7.151	13.758	6.198	14.288	6.436	10.716	4.827
25	16.404	7.389	14.288	6.436	14.817	6.674	11.113	5.006
26	16.933	7.628	14.817	6.674	15.346	6.913	11.509	5.184
27	17.463	7.866	15.346	6.913	15.875	7.151	11.906	5.363
28	17.992	8.105	15.875	7.151	16.404	7.389	12.303	5.542
29	18.521	8.343	16.404	7.389	16.933	7.628	12.700	5.721
30	19.050	8.581	16.933	7.628	17.463	7.866	13.097	5.900
31	19.579	8.820	17.463	7.866	17.992	8.105	13.494	6.078
32	20.108	9.058	17.992	8.105	18.521	8.343	13.891	6.257
33	20.638	9.296	18.521	8.343	19.050	8.581	14.288	6.436
34	21.167	9.535	19.050	8.581	19.579	8.820	14.684	6.615
35	-	-	19.579	8.820	20.108	9.058	15.081	6.793
36	-	-	20.108	9.058	20.638	9.296	15.478	6.972
37	-	-	20.638	9.296	21.167	9.535	15.875	7.151
38	-	-	21.167	9.535	-	-	-	-

each hour of each day. The number of traffic loads for each 1-hour time period in each day for eight traffic categories and tire length increments is used to calculate the bending or shearing stress intensity factor. The probability density of tire patch lengths for each traffic category can be determined from the cumulative axle load distribution function as follows:

$$P(L_j) = \frac{dC(L_j)}{dL_j} \quad (6)$$

where $P(L_j)$ is the probability density function within traffic category j and $C(L_j)$ is the cumulative probability within traffic category j .

For instance, the probability density function for the Category 1 of LTPP Section 180901 can be determined, based on the cumulative axle load distribution of the section provided in Figure 18; results are shown in Figure 19. The probability density for all categories of the LTPP sections is provided in Appendix E. The default probability density for Level 3 data input is presented in Table 17.

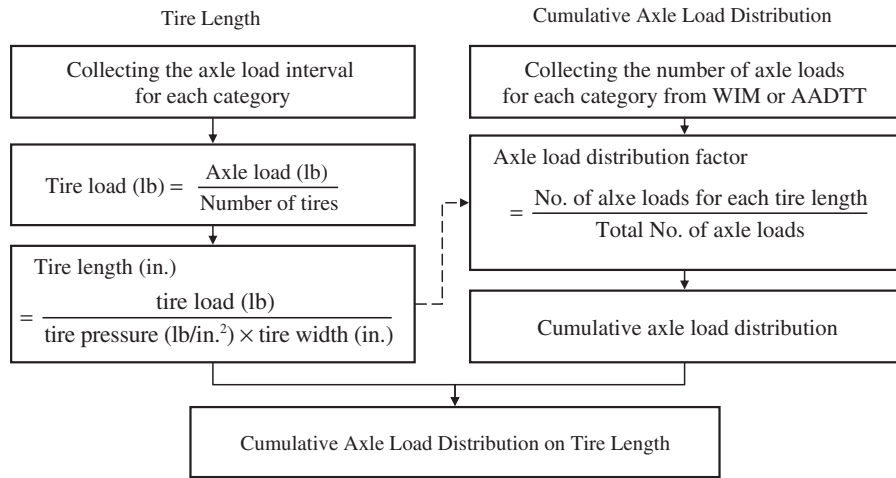


Figure 14. Determination of cumulative axle load distribution on tire patch length.

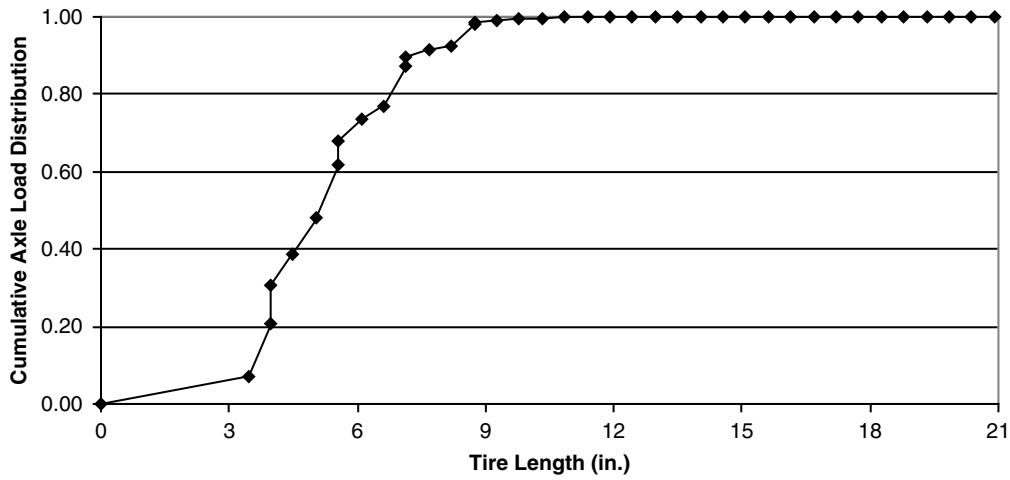


Figure 15. Cumulative axle load distribution versus tire length (Category 1 of LTPP section 180901 in 2004).

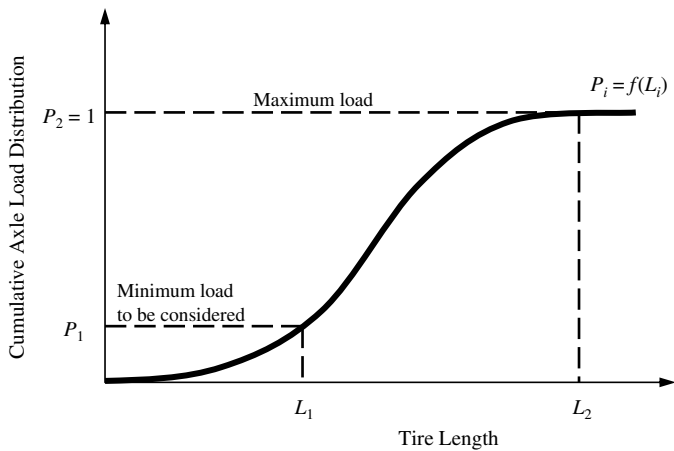


Figure 16. Typical tire length versus cumulative axle load distribution.

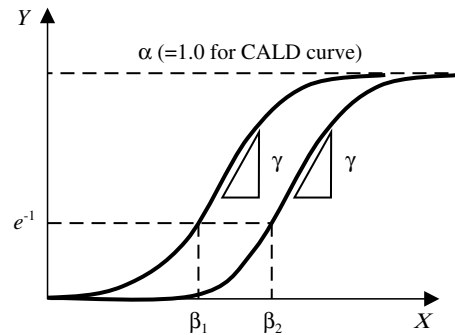


Figure 17. Gompertz model curve.

Table 13. Model parameters and CALD on tire length (Category 1 of LTPP section 180901 in 2004).

Parameter	Values	CALD Value		Tire Length (in.)	
		C_1		L_1	
β	4.301	C_1	0.071	L_1	3.704
γ	0.967				
R^2	0.982	C_2	1.000	L_2	16.933

Table 14. CALD model parameter default values determined based on LTPP data.

Traffic Category	Parameters		R^2
	β	γ	
1	3.44056	0.73836	0.980
2	3.58353	1.61999	0.999
3	1.62387	0.48959	0.972
4	2.03042	1.04234	0.990
5	1.72904	1.10906	0.906
6	1.92533	1.02297	0.982
7	1.47412	0.98443	0.969
8	2.70840	1.48446	0.956

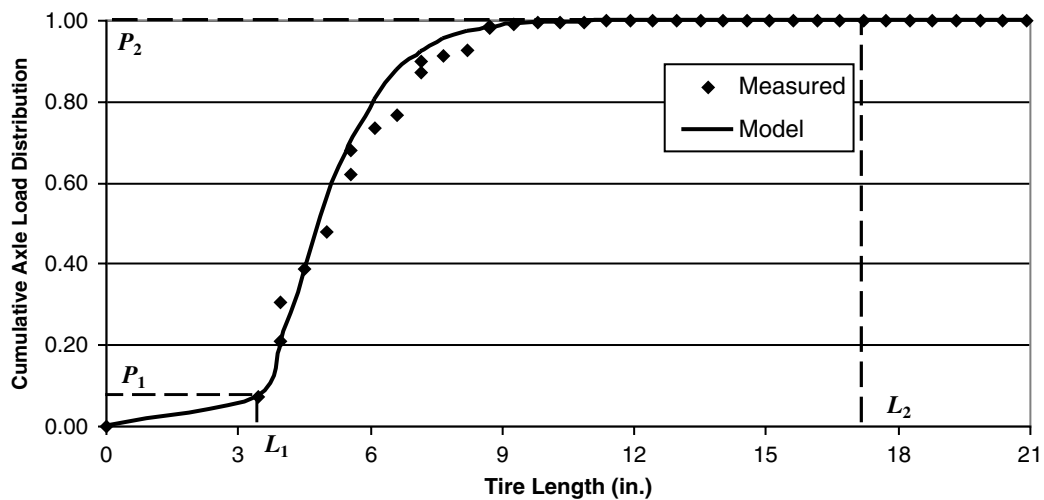


Figure 18. Cumulative axle load distribution versus tire length (Category 1 of LTPP Section 180901 in 2004).

Table 15. Minimum values to be considered for load related distress.

Traffic Category	Axle Type	Minimum Values	
		Axle load (lb)	Tire Length (in.)
1	Single	3,000	3.704
2			1.669
3	Tandem	6,000	1.588
4			0.715
5	Tridem	12,000	2.117
6			0.953
7	Quad	12,000	1.588
8			0.715

Table 16. Default cumulative axle load distribution for each traffic category.

No.*	Category							
	1	2	3	4	5	6	7	8
1	0.1320	0.0896	0.0971	0.0269	0.5835	0.0754	0.4005	0.0056
2	0.2541	0.1941	0.1654	0.0596	0.7411	0.1318	0.5384	0.0187
3	0.3958	0.3282	0.2494	0.1109	0.8465	0.2044	0.6578	0.0472
4	0.5341	0.4689	0.3424	0.1799	0.9115	0.2882	0.7532	0.0962
5	0.6542	0.5977	0.4373	0.2624	0.9498	0.3772	0.8255	0.1660
6	0.7505	0.7048	0.5281	0.3522	0.9718	0.4658	0.8783	0.2523
7	0.8235	0.7884	0.6110	0.4431	0.9842	0.5496	0.9160	0.3478
8	0.8769	0.8508	0.6837	0.5300	0.9912	0.6256	0.9423	0.4449
9	0.9149	0.8960	0.7457	0.6094	0.9951	0.6924	0.9606	0.5373
10	0.9416	0.9281	0.7973	0.6796	0.9973	0.7497	0.9732	0.6210
11	0.9601	0.9505	0.8396	0.7398	0.9985	0.7979	0.9818	0.6940
12	0.9728	0.9661	0.8738	0.7905	0.9992	0.8379	0.9876	0.7557
13	0.9815	0.9768	0.9011	0.8325	0.9995	0.8706	0.9916	0.8067
14	0.9875	0.9842	0.9228	0.8668	0.9997	0.8971	0.9943	0.8481
15	0.9915	0.9892	0.9399	0.8945	0.9999	0.9184	0.9962	0.8813
16	0.9942	0.9927	0.9533	0.9167	0.9999	0.9355	0.9974	0.9076
17	0.9961	0.9950	0.9637	0.9344	1.0000	0.9491	0.9982	0.9284
18	0.9974	0.9966	0.9719	0.9484	1.0000	0.9599	0.9988	0.9446
19	0.9982	0.9977	0.9782	0.9596	1.0000	0.9684	0.9992	0.9572
20	0.9988	0.9984	0.9832	0.9683	1.0000	0.9752	0.9995	0.9670
21	0.9992	0.9989	0.9870	0.9752	1.0000	0.9805	0.9996	0.9746
22	0.9994	0.9993	0.9899	0.9806	1.0000	0.9847	0.9997	0.9805
23	0.9996	0.9995	0.9922	0.9848	1.0000	0.9880	0.9998	0.9850
24	0.9997	0.9997	0.9940	0.9882	1.0000	0.9906	0.9999	0.9885
25	0.9998	0.9998	0.9954	0.9907	1.0000	0.9926	0.9999	0.9911
26	0.9999	0.9998	0.9964	0.9928	1.0000	0.9942	0.9999	0.9932
27	0.9999	0.9999	0.9972	0.9944	1.0000	0.9954	1.0000	0.9948
28	0.9999	0.9999	0.9979	0.9956	1.0000	0.9964	1.0000	0.9960
29	1.0000	1.0000	0.9984	0.9966	1.0000	0.9972	1.0000	0.9969
30	1.0000	1.0000	0.9987	0.9973	1.0000	0.9978	1.0000	0.9976
31	1.0000	1.0000	0.9990	0.9979	1.0000	0.9983	1.0000	0.9982
32	1.0000	1.0000	0.9992	0.9984	1.0000	0.9987	1.0000	0.9986
33	1.0000	1.0000	0.9994	0.9987	1.0000	0.9989	1.0000	0.9989
34	1.0000	1.0000	0.9995	0.9990	1.0000	0.9992	1.0000	0.9992
35	-	-	0.9997	0.9992	1.0000	0.9994	1.0000	0.9994
36	-	-	0.9997	0.9994	1.0000	0.9995	1.0000	0.9995
37	-	-	0.9998	0.9995	1.0000	1.0000	1.0000	1.0000
38	-	-	1.0000	1.0000	-	-	-	-

* Number represents the tire patch length increment listed in Table 12.

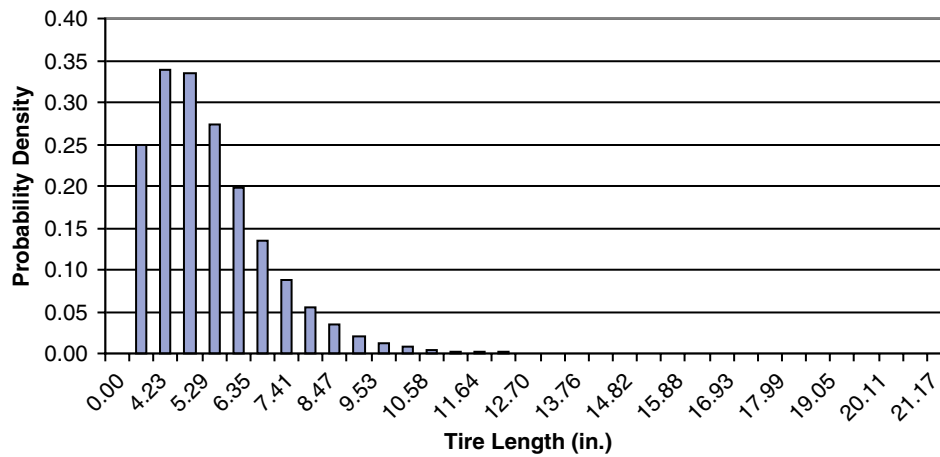


Figure 19. Probability density function of tire length (Category 1, LTPP Section 180901).

Table 17. Default probability density for each traffic category.

No.*	Traffic Category							
	1	2	3	4	5	6	7	8
1	0.1974	0.3502	0.1109	0.1014	0.3486	0.1993	0.3608	0.0429
2	0.2570	0.5155	0.1457	0.1753	0.2462	0.2733	0.3282	0.1103
3	0.2709	0.5924	0.1696	0.2542	0.1564	0.3320	0.2713	0.2140
4	0.2473	0.5753	0.1797	0.3216	0.0936	0.3668	0.2102	0.3344
5	0.2050	0.4984	0.1771	0.3659	0.0543	0.3762	0.1558	0.4426
6	0.1591	0.3994	0.1651	0.3831	0.0309	0.3640	0.1122	0.5158
7	0.1181	0.3037	0.1474	0.3759	0.0174	0.3365	0.0792	0.5453
8	0.0851	0.2227	0.1273	0.3508	0.0097	0.3002	0.0551	0.5349
9	0.0601	0.1594	0.1071	0.3146	0.0054	0.2604	0.0380	0.4954
10	0.0418	0.1122	0.0884	0.2736	0.0030	0.2209	0.0260	0.4392
11	0.0289	0.0781	0.0719	0.2324	0.0017	0.1842	0.0178	0.3763
12	0.0198	0.0540	0.0577	0.1937	0.0009	0.1516	0.0121	0.3143
13	0.0135	0.0371	0.0459	0.1591	0.0005	0.1234	0.0082	0.2573
14	0.0092	0.0254	0.0363	0.1292	0.0003	0.0997	0.0056	0.2074
15	0.0062	0.0174	0.0285	0.1040	0.0002	0.0800	0.0038	0.1653
16	0.0042	0.0118	0.0223	0.0831	0.0001	0.0638	0.0026	0.1306
17	0.0029	0.0081	0.0174	0.0661	0.0000	0.0507	0.0017	0.1024
18	0.0019	0.0055	0.0136	0.0523	0.0000	0.0402	0.0012	0.0799
19	0.0013	0.0037	0.0105	0.0413	0.0000	0.0318	0.0008	0.0621
20	0.0009	0.0025	0.0082	0.0325	0.0000	0.0251	0.0005	0.0481
21	0.0006	0.0017	0.0063	0.0255	0.0000	0.0198	0.0004	0.0372
22	0.0004	0.0012	0.0049	0.0200	0.0000	0.0156	0.0002	0.0287
23	0.0003	0.0008	0.0038	0.0157	0.0000	0.0122	0.0002	0.0221
24	0.0002	0.0005	0.0029	0.0123	0.0000	0.0096	0.0001	0.0170
25	0.0001	0.0004	0.0023	0.0096	0.0000	0.0075	0.0001	0.0131
26	0.0001	0.0003	0.0018	0.0075	0.0000	0.0059	0.0001	0.0101
27	0.0001	0.0002	0.0014	0.0059	0.0000	0.0046	0.0000	0.0077
28	0.0000	0.0001	0.0010	0.0046	0.0000	0.0036	0.0000	0.0059
29	0.0000	0.0001	0.0008	0.0036	0.0000	0.0029	0.0000	0.0046
30	0.0000	0.0001	0.0006	0.0028	0.0000	0.0022	0.0000	0.0035
31	0.0000	0.0000	0.0005	0.0022	0.0000	0.0018	0.0000	0.0027
32	0.0000	0.0000	0.0004	0.0017	0.0000	0.0014	0.0000	0.0021
33	0.0000	0.0000	0.0003	0.0013	0.0000	0.0011	0.0000	0.0016
34	0.0000	0.0000	0.0002	0.0010	0.0000	0.0008	0.0000	0.0012
35			0.0002	0.0008	0.0000	0.0007	0.0000	0.0008
36			0.0001	0.0005	0.0000	0.0004	0.0000	0.0005
37			0.0001	0.0004	0.0000	0.0000	0.0000	0.0000
38			0.0000	0.0000				

* Number represents the tire patch length increment listed in Table 12.

Reflection Cracking Amount and Severity Model

The development of reflection crack amount and severity versus time or number of load repetitions follows a sigmoidal curve having a finite upper asymptote for three different severity levels, as shown in Figure 20.

Jayawickrama and Lytton (12) proposed an s-shaped empirical model to describe the amount and severity development of reflection cracking on an asphalt overlay. This model describes the reflection cracking versus the number of load repetition or time relationship as follows:

$$RFAS = 100 \cdot e^{-\left(\frac{\rho}{D_{Total}}\right)^{\beta}} \quad (7)$$

where

$RFAS$ = reflection cracking amount and severity, ranging from 0 to 100%;

D_{Total} = total number of days since the overlay construction was completed; and

ρ and β = calibration parameters for each severity level.

The parameter ρ is the scale factor for reflection cracking amount and severity. A large ρ value indicates that much accumulated damage must occur to reach a given level of reflection cracking amount; that is, the parameter ρ describes the spread of the rising portion of the curve, the parameter ρ is always equal to the total number of days to reach 36.8 percent ($= 1/e$) of the total amount of expected reflection cracking. The parameter β is the shape factor that describes how steep the rising portion of the curve is as shown in Figure 21 (more details on this amount and severity model are provided in Appendix K).

Because the reflection cracking severity and amount model has a clear physical boundary condition (0 to 100 percent) and the parameters, ρ and β , have physical meanings, the model was selected for the calibration with different field data sets. However, because the database used for model calibration consisted of the length of observed transverse cracks when the survey was performed before and after overlay, the variables of the original reflection cracking model were modified as follows:

$$D(N_i)(\%) = e^{-\left(\frac{\rho}{N_i}\right)^{\beta}} \quad (8)$$

where

$D(N_i)$ = percent of reflection crack length of maximum crack length at N_i ;

i = i th crack observation;

N_i = number of days after overlay.

The percent of reflection crack length, $D(N_i)$, at each observation was calculated by dividing the observed length of transverse crack, after overlay construction, by the total length of transverse crack on an existing pavement surface just before overlay construction. The total crack length on an existing surface can be described as the likelihood of maximum reflection cracking length on an overlay surface. The number of days after overlay, N_i , is determined by counting the days after overlay construction when a given set of observations were made. Based on the field data obtained from test sections, the parameters ρ and β were calibrated for different severity levels. Three sets of parameters were calibrated when all three severity levels were available:

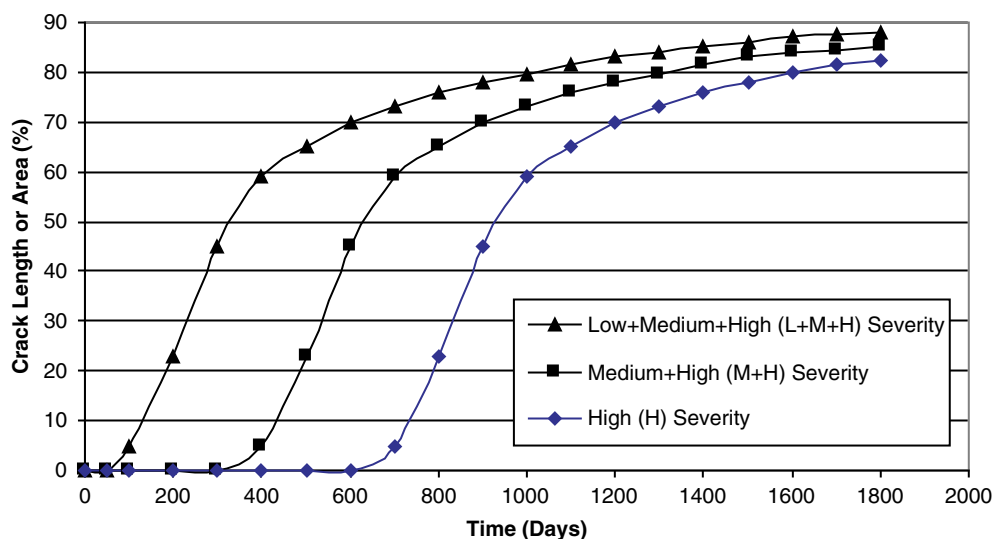


Figure 20. Typical development of reflection crack by severity levels.

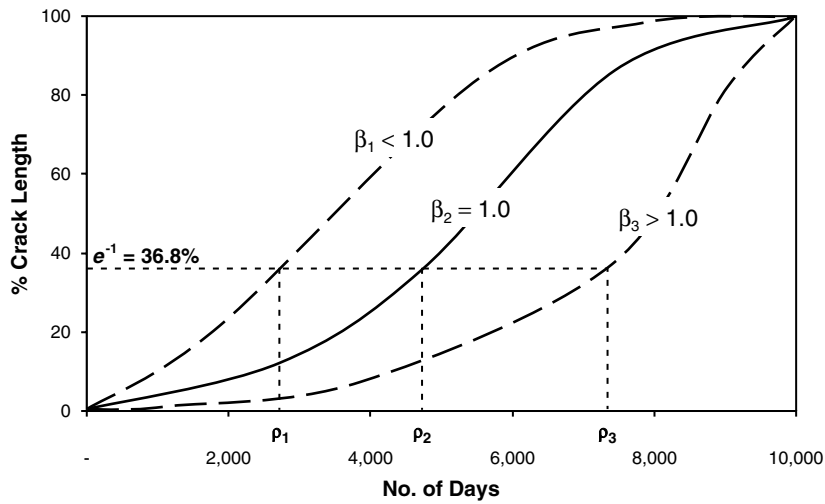


Figure 21. Parameters in reflection cracking severity model.

- ρ_H and β_H for high severity level,
- ρ_H and β_H for medium and high severity levels, and
- ρ_{LMH} and β_{LMH} for low, medium, and high severity levels.

The reflection cracking models were calibrated using field data for overlay test sections which have sufficient crack measurements. Figure 22 shows the crack amounts expressed as percentages of the original crack length observed in LTPP section 270506, at three severity conditions: high; high or medium; and high, medium, or low severity.

The same type of data was obtained for the test sections in New York City (27); example is shown in Figure 23. These sections included different types of geosynthetic materials reinforcing the overlays.

Another set of reflection cracking data was found in the geosynthetically reinforced test sections in Texas, an example

of which is shown in Figure 24 (28). These sections included HMA overlays over cracked asphalt surface layers in Amarillo and HMA overlays over jointed concrete pavements in Marlin. Geosynthetic materials were used to reinforce all of the overlays in both of these sites. Reflection cracking data for the LTPP sites, New York test sections, and Texas test sections are presented in Appendix J.

Calibration of Field Reflection Cracking Model

One objective of the study was to calibrate the reflection cracking amount and severity model with reflection crack data observed in the field. The calibration refers to the mathematical process through which the total error or difference between observed and predicted values of distress

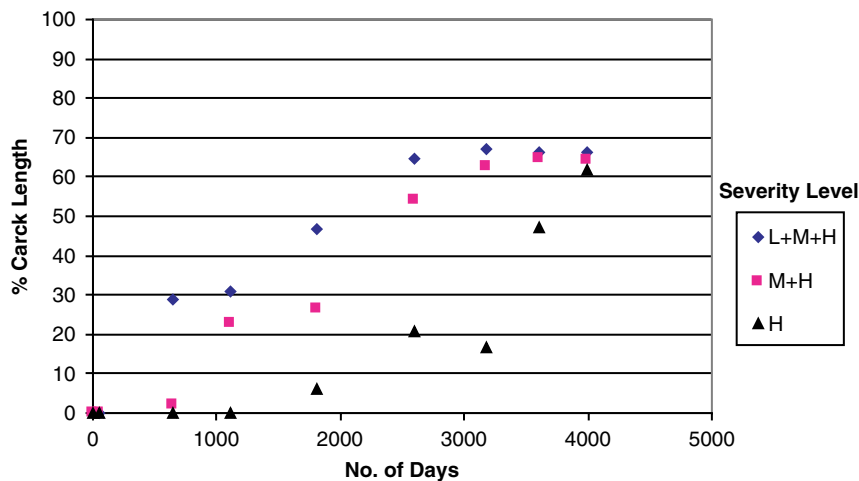


Figure 22. Reflection cracking amount versus number of days for LTPP section 270506.

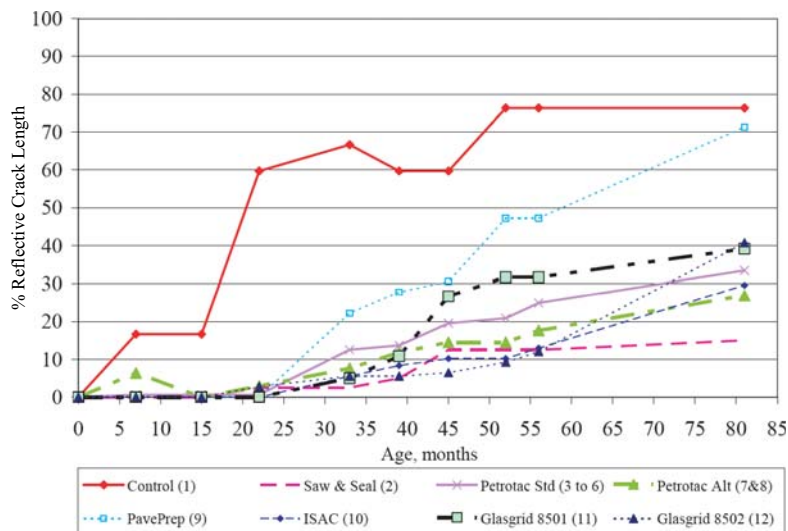


Figure 23. Reflection cracking amount data from test sections in New York City.

is minimized. The process used to achieve the calibration, which determines ρ and β in the reflection cracking model, was conducted using available field reflection cracking data and an iterative method of the System Identification process (details of the calibration process are presented in Appendix L).

System Identification Process

The reflection cracking amount and severity model at a given severity level was considered to have been calibrated

when the error between observed and predicted crack lengths was minimized. Since the predicted crack length is calculated by the calibrated model at each test section, a solution method was required to determine the parameters ρ and β in the model. In this study, the system identification process was used.

The purpose of the system identification process is to develop a mathematical model which describes the behavior of a system (real physical process). The actual system and the mathematical model are identified when the error between them is minimized or satisfies the error criteria; otherwise, the model

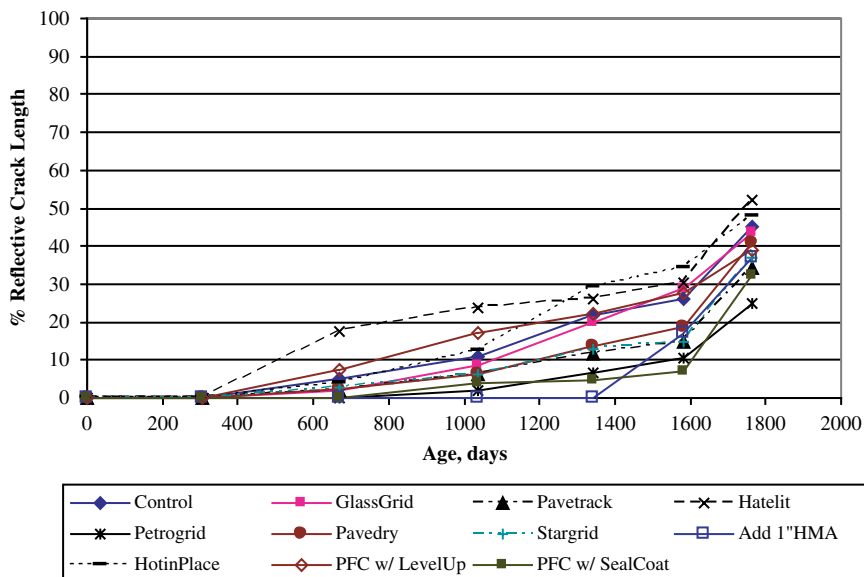


Figure 24. Low severity reflection cracking amount data in Amarillo, Texas.

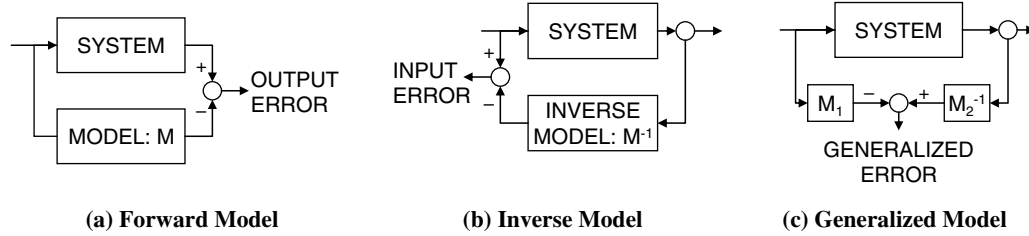


Figure 25. Methods for system identification process (29).

should be adjusted until the error is reduced sufficiently (29). The system identification process considers three different error minimization models depending on the choice of residuals combined with the model: forward model, inverse model, and generalized model shown in Figure 25. The forward approach minimizes the output error between the model and the system while using the same input. In the inverse approach, the input error is minimized based on the same output. The generalized model is a combination of the forward and inverse approach when the model is invertible (29).

When the system output is fixed because it is observed or obtained from an actual system, the output from the model must be refined to calibrate the mathematical model including its parameters. In this project, the reflection cracking amount and severity model (mathematical model) was calibrated based on observed reflection crack data (actual system output) to produce the predicted crack data (model output) which is close to the observed crack data.

An optimal model for the physical system is obtained when the output error between the system and the model is small enough to meet an error criterion. However, if the error does not meet the criterion, the parameters in the mathematical model should be corrected by a parameter adjustment and adaptation algorithm. The correction process is performed iteratively until the error becomes small enough to meet the

error criterion. Figure 26 depicts use of the forward model in the system identification process including the parameter adjustment and adaptation algorithm for the reflection cracking model calibration.

Parameter Adjustment and Adaption Algorithm

A parameter adjustment and adaptation algorithm was developed based on the Taylor series expansion as follows (30)

$$[F_{ki}]\{\alpha_i\} = \{r_k\} \tag{9}$$

where

$$[F_{ki}] = \text{sensitivity matrix} = \sum_{k=1}^m \sum_{i=1}^n \frac{\partial f_k}{\partial p_i} \frac{p_i}{f_k} (m \times n \text{ matrix});$$

m, n = number of output data and model parameters, respectively;

f_k = mathematical model;

p_i = model parameters;

$\{\alpha_i\}$ = change vector (relative change of parameters) = $[\alpha_1, \alpha_2, \dots, \alpha_m]^T$; and

$\{r_k\}$ = residual vector (error between system and model outputs) = $[r_1, r_2, \dots, r_m]^T$.

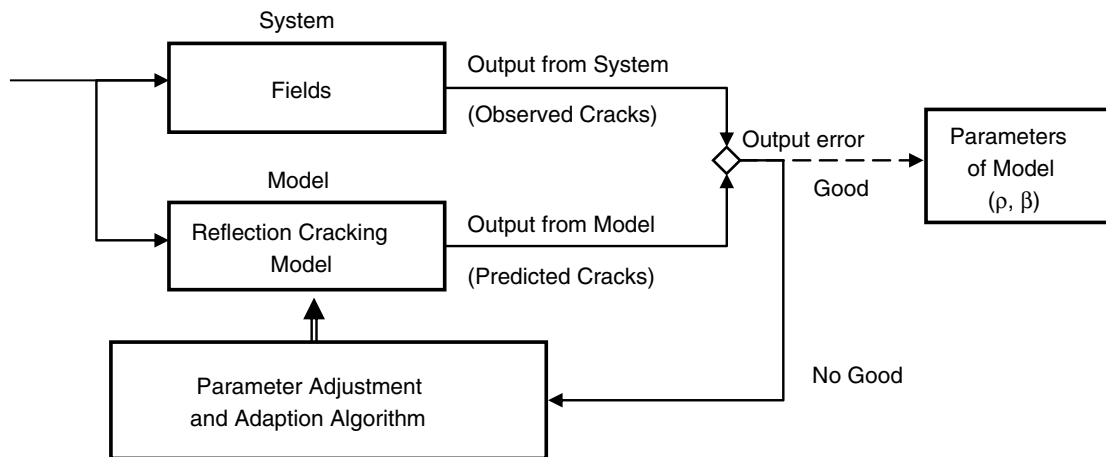


Figure 26. Scheme of system identification process.

The minimization of error contained within the residual vector $\{r_k\}$ is analogous to the reduction of error employed in least squared error analysis. The squared error between actual output and predicted output is calculated by using a mathematical model to determine the sensitivity of the weighting parameters for allocating the squared error. It is possible to adjust the model parameters until there is no squared error remaining; however, because of the presence of random error, the values in the residual matrix $\{r_k\}$ should not be forced to zero (31). The elements in the residual vector $\{r_k\}$ which represents errors between the actual and model outputs are determined based on model parameters p_i assuming at each iteration in the process, that they are known values. The sensitivity matrix $[F_{ki}]$, which reflects the sensitivity of the output from mathematical model f_k to the assumed parameters p_i , is also a known value. Therefore, the unknown change vector $\{\alpha_i\}$ presents the relative changes of the model parameters and is the target vector to be determined in the process. Equation 9 can be rewritten as:

$$\{\alpha_i\} = [F_{ki}^T F_{ki}]^{-1} [F_{ki}]^T \{r_k\} \quad (10)$$

The change vector $\{\alpha_i\}$ obtained using an initial assumption of parameters, can then be used to determine the following new set of parameters.

$$p_i^{j+1} = p_i^j (1 + 0.6\alpha_i) \quad (11)$$

Where j is the iteration count.

Solutions for the parameters in the model are found by minimizing the change vector $\{\alpha_i\}$. Therefore, the iteration process using Equation 10 is continued until there is no squared error remaining or the desired convergence is reached. Thus, the iteration was repeated until the elements in the change vector $\{\alpha_i\}$ are less than 0.01.

Calibrating Reflection Cracking Model of Test Sections

Based on the system identification and the parameter adjustment algorithm, the reflection cracking models were calibrated using the data obtained from LTPP, New York City, and Texas asphalt overlay test sections. The process was used to fit the predicted crack length to the measured crack length by iteration. Thus, the parameter adjustment algorithm of Equation 9 can be expressed as follows:

$$[F]\{\alpha\} = \{r\} \quad (12)$$

$$\begin{bmatrix} \frac{\partial \bar{D}(N_1)}{\partial \rho^j} \frac{\rho^j}{\bar{D}(N_1)} & \frac{\partial \bar{D}(N_1)}{\partial \beta^j} \frac{\beta^j}{\bar{D}(N_1)} \\ \frac{\partial \bar{D}(N_2)}{\partial \rho^j} \frac{\rho^j}{\bar{D}(N_2)} & \frac{\partial \bar{D}(N_2)}{\partial \beta^j} \frac{\beta^j}{\bar{D}(N_2)} \\ \vdots & \vdots \\ \frac{\partial \bar{D}(N_i)}{\partial \rho^j} \frac{\rho^j}{\bar{D}(N_i)} & \frac{\partial \bar{D}(N_i)}{\partial \beta^j} \frac{\beta^j}{\bar{D}(N_i)} \end{bmatrix} \begin{bmatrix} \rho^{j+1} - \rho^j \\ \beta^{j+1} - \beta^j \\ \beta^j \end{bmatrix} = \begin{bmatrix} \frac{D(N_1) - \bar{D}(N_1)}{\bar{D}(N_1)} \\ \frac{D(N_2) - \bar{D}(N_2)}{\bar{D}(N_2)} \\ \vdots \\ \frac{D(N_i) - \bar{D}(N_i)}{\bar{D}(N_i)} \end{bmatrix} \quad (13)$$

where

$\bar{D}(N_i)$ = crack length at N_i , calculated using ρ^j and β^j , and
 $D(N_i)$ = measured crack length at N_i .

The parameters ρ and β in the model were determined by iteration. The convergence criterion was set to 1.0 percent (i.e., the iteration was repeated until the elements in the change vector were less than 0.01).

The percent crack length at each of the pavement ages was used to develop the model parameters ρ and β in the reflection cracking model along with the system identification process. Table 18 presents an example of the percent of reflection cracking development of all severity levels of four LTPP sections, which were calculated based on reflection crack data in Table 18. Table 19 shows the developed model parameters, and Figures 27 through 30 present plots of the compiled and measured data for four LTPP sections. The calibrated parameters for all asphalt overlay test sections in the LTPP, New York City, and Texas are listed in Appendix M.

The model parameters ρ and β for the three levels of distress are the “field data” which will be calibrated to the number of days for a crack to propagate through the overlay computed with the reflection cracking model. The coefficients by which the different modes of crack propagation relate to these field derived model parameters are the “calibration coefficients” which define a particular application (pavement structure, climatic zone, region) of the reflection cracking model. The ρ and β calibration coefficients for all of the overlaid sections are tabulated in Appendix M.

Table 18. Reflection cracking development of L+M+H for LTPP test sections.

Section No.	Overlay Type	Number of Days after Overlay	% Crack Length
340503	AC/AC OL	0	0
		1,200	0
		1,492	0
		2,283	9.86
		2,640	8.28
		3,004	20.41
		3,367	28.12
		3,757	29.59
		4,121	45.92
		4,247	55.78
270506	AC/Mill/AC OL	0	0
		52	0
		641	28.76
		1,110	30.84
		1,803	46.60
		2,595	64.55
		3,183	67.02
		3,600	66.46
		3,992	66.07
240563	AC/FC/AC OL	0	0
		1,226	20.60
		1,799	65.76
		2,590	70.47
		2,990	64.76
		3,375	81.89
		3,802	88.59
		4,012	92.06
		4,395	93.30
55B901	JRC/AC OL	0	0
		114	3.91
		358	37.32
		869	75.44
		2,499	93.86
		3,760	95.14
		4,410	99.12

Table 19. Calibrated model parameters of LTPP sections.

LTPP Section No.	Overlay Type	Model Parameters (L+M+H)	
		β	ρ
340503	AC/AC	2.365	3,617.12
270506	AC/Mill/AC	0.702	1,004.85
240563	AC/FC/AC	2.276	1461.25
55B901	JRC/AC	1.159	329.42

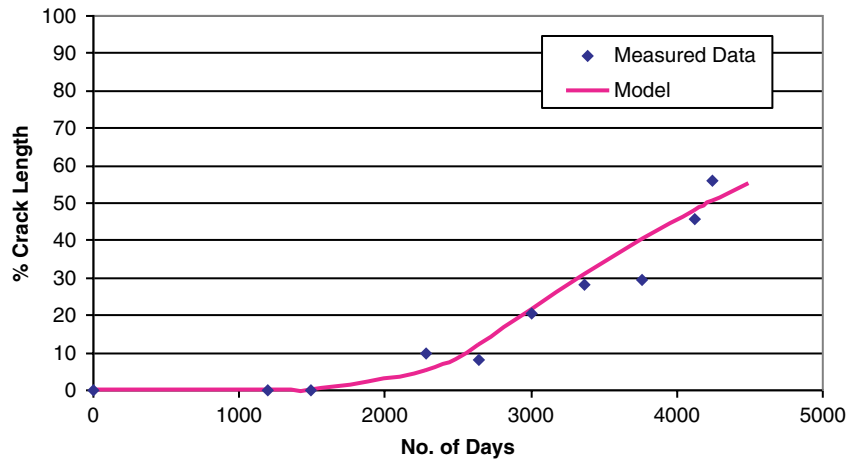


Figure 27. Computed and measured reflection crack for LTPP section 340503.

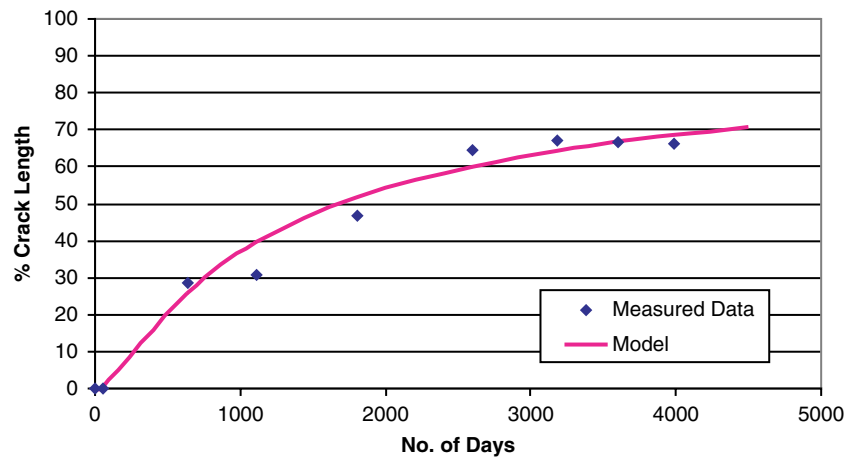


Figure 28. Computed and measured reflection crack for LTPP section 270506.

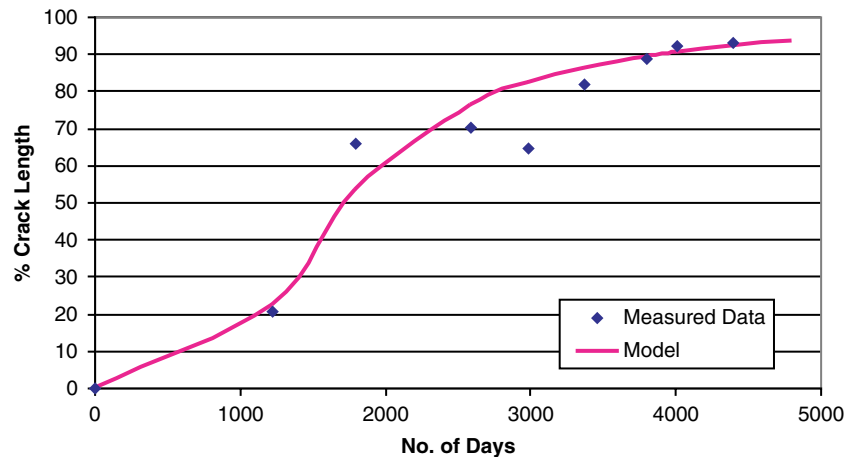


Figure 29. Computed and measured reflection crack for LTPP section 240563.

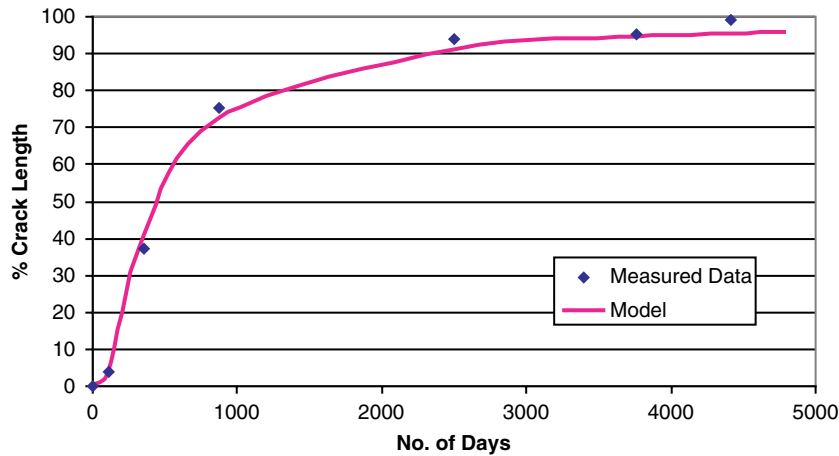


Figure 30. Computed and measured reflection crack for LTPP section 55B901.

Prediction of Temperature in a HMA Overlay

A new temperature model was developed to better predict temperature variations with depth within the overlay. The model differs somewhat from the model in the EICM (32, 33, 34) that is used in the MEPDG. A comparison of the temperatures in a pavement surface as measured and as calculated by the EICM model is shown in Figure 8. Figure 9 shows a comparison between the measured temperatures and as calculated with the new model. The figures illustrate that the new model matches the measured temperatures more closely than the EICM model. The new one-dimensional model was developed based on radiation and conduction energy balance fundamentals (details of the model are presented in Appendix B). The heat transfer process is depicted in Figure 31. Sources of heat transfer at the pavement surface are solar radiation and reflection of the solar radiation at the surface by a fraction α , the albedo; absorption of atmospheric down-welling long-wave radiation by the pavement surface; emission by long-

wave radiation to the atmosphere; convective heat transfer between pavement surface; and the air close to the surface, which is enhanced by wind. Below the surface and within the pavement and ground beneath it, heat is transferred by conduction. Not included in this model is heat transfer enhancement by precipitation. Mathematical details of this model follow.

Heat Transfer in Pavement

Heat transfer in the pavement is governed by the classical thermal diffusion equation

$$\frac{\partial T}{\partial t} = \alpha \frac{\partial^2 T}{\partial x^2} \quad (14)$$

where

T = the pavement temperature as a function of time and depth below the surface (x);

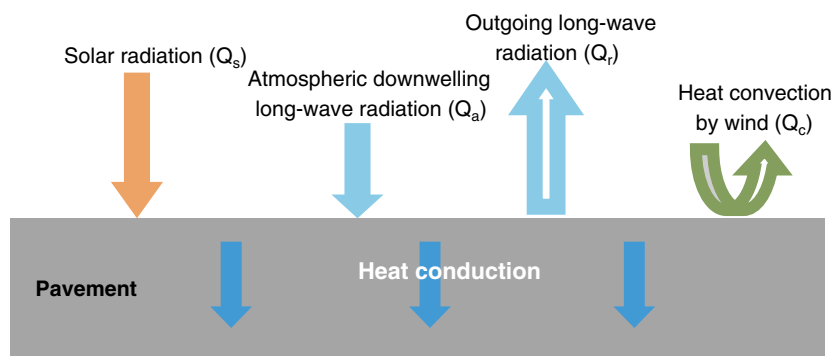


Figure 31. Schematic presentation of heat transfer model of pavement.

α = the thermal diffusivity;
 $\alpha = k/\rho C$ where k is the thermal conductivity;
 ρ = the density; and
 C = the pavement heat capacity.

Together with this equation, a flux boundary condition at the pavement surface and a second flux condition at 3 m below the surface are considered.

The Surface Boundary Condition

Considering a differential element of the pavement surface, its thermal energy (temperature) will change to the extent that the fluxes from above and from below do not balance. The various fluxes shown in Figure 31 lead to the following surface condition:

$$\rho C \frac{\Delta x}{2} \frac{\partial T_s}{\partial t} = Q_s - \tilde{\alpha} \cdot Q_s + Q_a - Q_r - Q_c - Q_f \quad (15)$$

where

ρC = volumetric heat capacity of the pavement;
 T_s = pavement surface temperature;
 x = the depth below the pavement surface;
 $\frac{\Delta x}{2}$ = the (differential) pavement thickness for the energy balance;
 Q_s = heat flux due to solar radiation;
 $\tilde{\alpha}$ = albedo of pavement surface, the fraction of reflected solar radiation;
 Q_a = down-welling long-wave radiation heat flux from the atmosphere;
 Q_r = outgoing long-wave radiation heat flux from the pavement surface;
 Q_c = the convective heat flux between the surface and the air; and
 Q_f = the heat flux within the pavement at the pavement surface.

The incoming and outgoing long-wave radiation (in $W \cdot m^{-2}$) are calculated by:

$$Q_a = \epsilon_a \sigma T_a^4 \quad (16)$$

$$Q_r = \epsilon \sigma T_s^4 \quad (17)$$

where

ϵ_a = absorption coefficient of pavement;
 ϵ = emission coefficient of pavement;
 T_s = pavement surface temperature, k;
 T_a = air temperature, k; and
 $\sigma = 5.68 \times 10^{-8} W \cdot m^{-2} K^{-4}$ is Stefan-Boltzman constant

The convective heat flux (in $W \cdot m^{-2}$) is calculated as:

$$Q_c = h_c (T_s - T_a) \quad (18)$$

where h_c is the heat transfer coefficient from the empirical equation (33).

$$h_c = 698.24 \cdot a \cdot \left[0.00144 \left(\text{abs} \left(\frac{T_s + T_a}{2} \right) \right)^{0.3} U^d + 0.00097 (\text{abs}(T_s + T_a))^{0.3} \right] \quad (19)$$

where U is the hourly wind speed ($i m \cdot s^{-1}$) and a and d are two-dimensionless empirical parameters.

The heat flux within the pavement at the surface is expressed by Fourier's equation:

$$Q_f = k \frac{\partial T_s}{\partial x} \quad (20)$$

where T_s is pavement surface temperature, and k is thermal conductivity of asphalt concrete (in $W \cdot m^{-1} \cdot k^{-1}$).

Combining these results, the following equation serves as the surface boundary condition:

$$\rho C \frac{\Delta x}{2} \frac{\partial T_s}{\partial t} = Q_s - \tilde{\alpha} \cdot Q_s + \epsilon_a \sigma T_a^4 - \epsilon \sigma T_s^4 - h_c (T_s - T_a) + k \frac{\partial T_s}{\partial x} \quad (21)$$

The Bottom Boundary Condition

Commonly, a constant-temperature boundary condition at some distance below the surface is reported. For example, Hermansson (19) used the annual mean temperature 5 m below the surface as a bottom boundary condition and Gui (20) used a measured temperature of 33.5°C at a depth of 3 m as the boundary condition. In the EICM model, temperatures were measured from water wells across the country at a depth of 10 to 18 m, from which an isothermal map was constructed. Such a constant-temperature boundary condition has the advantage of simplicity.

In this project, a different approach was used. Measured data in the LTPP database showed that temperatures at a depth beyond 2 m tend to vary approximately linearly with depth. Therefore, a flux boundary condition was used at a depth of 3 m. That is

$$\frac{\partial T}{\partial x} \Big|_{3 \text{ m}} = \text{independent of depth} \quad (22)$$

This boundary condition is independent of location and does not require a specific value. In addition, it is easy to implement this boundary condition in the finite difference

calculation procedure. However, this thermal gradient boundary condition is not accurate if extrapolated to too great a depth.

Numerical Solution of the Model

This model was solved numerically using a finite difference approximation method, together with required input data (i.e., hourly solar radiation, air temperature, wind speed, and model parameter values). In the numerical solution, the pavement thickness was divided into cells, which are thinner near the surface and thicker at deeper levels. Each cell is given a temperature (equal to air temperature) at the start of the calculation as an initial condition. The model then calculates a new temperature for each cell (several times for each simulated hour) at each time step.

Obtaining Hourly Climatic Input Data

For any pavement site, model calculation requires accurate site-specific hourly climatic data and model parameters, including hourly solar radiation, hourly air temperature, and daily average wind speed data in an hourly format.

Hourly solar radiation can be collected from the National Solar Radiation Database (NSRDB). Hourly solar radiation data are modeled using State University of New York at Albany (SUNY) or Meteorological-Statistical (METSTAT) models based on satellite images, covering nearly all parts of the country from 1990 to 2005.

Daily average wind speed can be collected directly from the Virtual Weather Station program in the LTPP. Additionally, daily wind speed can be obtained directly from the National Climatic Data Center (NCDC) or the meteorological network in each state. Hourly wind speed is preferred, but such data are difficult to obtain and more vulnerable to environmental conditions, adding difficulty in the interpolation. However, the model is not overly sensitive to the wind speed such that daily values are adequate.

Hourly air temperature data are not commonly available, yet reasonable estimates of these hourly temperatures are needed for accurate temperature calculations. In order to estimate hourly wind speed data, a method was developed to estimate hourly air temperatures from daily maximum and minimum air temperatures. Recorded daily maximum and minimum air temperatures can be obtained easily from the Virtual Weather Stations in the LTPP database or NCDC.

A conventional method to impute hourly air temperatures fits a sinusoidal function to daily maximum and minimum air temperatures (e.g., 32, 33, 34). However, the daily profile of air temperature is not exactly sinusoidal. Typically, air temperature rises from the daily minimum temperature to the daily maximum temperature in about 9 hours, and decreases

from the daily maximum temperature to the daily minimum in about 15 hours. A more accurate air temperature prediction method would incorporate this non-sinusoidal pattern.

In order to obtain a more representative pattern of daily air temperatures, data over an entire year were obtained from the Automatic Weather Station (AWS) in the LTPP database and analyzed using a seasonal trend decomposition time series analysis. The trend trace is a moving average of the measured data, which represents the daily average temperature throughout the year. The “seasonal” trace is obtained by subtracting the trend line from the measured data and finding a local polynomial which best fits the result. This trace represents the regular pattern of daily air temperature, which is used instead of a sinusoidal function.

With a known daily pattern of air temperature, the hourly air temperatures can be reconstructed from daily maximum and minimum measured data. First, the daily average air temperature data are taken from the trend trace. Then, the trend and the seasonal traces obtained from the time series analysis are added together. Finally, the result is linearly transformed to fit the measured data, day by day. The non-sinusoidal predicted daily temperature patterns at six different sites are shown in Figure 32.

More details on this temperature model are presented in Appendix B, including comparisons of the predicted pavement temperatures at different depths with the measured temperatures. Also presented are maps of the geographic distributions of the temperature variables of albedo, emissivity, and absorptivity, all of which were shown by a sensitivity analysis to be important input variables.

Stiffness, Tensile Strength, Compliance, and Fracture Properties of Mixtures

The properties of a HMA mixture in an overlay must be estimated both accurately and with computational efficiency to achieve an overlay design resistant to reflection cracking. The stiffness and compliance of the mixture must be calculated at widely different temperatures and loading rates (thermal and traffic). The tensile strength must also be calculated over the same wide ranges of temperature and loading rates. The fracture properties (i.e., Paris and Erdogan’s Law coefficients) must be calculated. These coefficients are also sensitive to temperature and loading rates. For these reasons, ANN algorithms which reproduce Witczak’s 1999 (2) and 2006 (3) Complex Modulus models were developed to form the basis for calculating the overlay stiffness under traffic loads and computing the viscoelastic thermal stress for thermal reflection cracking. The method used to construct ANN algorithms is described in the literature (22). The accuracy with which these algorithms reproduce the Witczak Complex Modulus

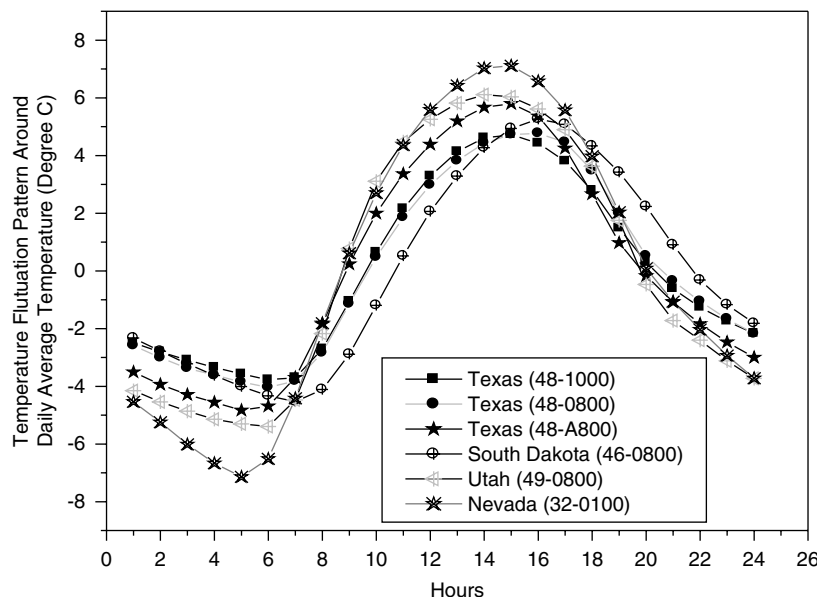


Figure 32. Predicted daily air temperatures at six different LTPP test sites.

models is described. The tensile strength was determined by Schapery (36, 37) to be an important variable in making realistic estimates of the Paris and Erdogan’s Law fracture coefficient, A. Earlier studies reported tensile strengths obtained of field cores taken from pavement sections well distributed around the United States and Canada (4, 38) and were considered to be representative of HMA mixtures. The calibration coefficients from these studies (4) could be used to predict both thermal and traffic related reflection cracking and healing between traffic loads.

Artificial Neural Network Algorithms for Witczak’s Complex Modulus Models

The binder input data required for the 1999 Witczak model (2) are the viscosity, η , and frequency of loading in Hertz, as shown in Table 20. Figure 33 shows a graphic comparison between the data obtained using Witczak’s 1999 model and those developed using the ANN algorithm (35) (statistical comparisons are provided in Appendix G). The R^2 values are

0.68 and 0.98 for the 1999 Witczak model and the ANN algorithm, respectively, when using the source input data

The binder input data for the 2006 Witczak model is the magnitude of the shear modulus, G^* , of the binder and its phase angle, δ , in degrees, as shown in Table 21. Also shown in that table are the other required input variables for the model, which include the same gradation and volumetric composition as in the 1999 model. The output is the magnitude of the Complex Modulus. A comparison of the behavior of the 2006 Witczak model (3) and the corresponding ANN algorithm is shown in Figure 34. The R^2 values are 0.77 and 0.96 for the 2006 Witczak model and the corresponding ANN algorithm, respectively.

The user input to the ANN mixture modulus model is the gradation and volumetric parts of the mix design and the binder data. In keeping with the MEPDG format, the binder data can be input at any of three levels. The binder data are the six properties of the CAM model (i.e., G_b , the glassy modulus in Gpa; R, the Rheological Index; ω_m , the cross-over frequency in rad/sec; T_b , the defining temperature in $^{\circ}C$; and the two time-temperature shift parameters, C_1 and C_2) (39). The

Table 20. Data input for 1999 Witczak model (viscosity, η , and frequency of loading in Hertz).

Input								Output	R^2	
Gradation				Volumetric		Binder Data			Witczak	ANN
3/4 (%)	3/8 (%)	#4 (%)	#200 (%)	V_a (%)	V_{beff} (%)	η 10^6 poise	f_c Hz	E^* psi	0.68	0.98

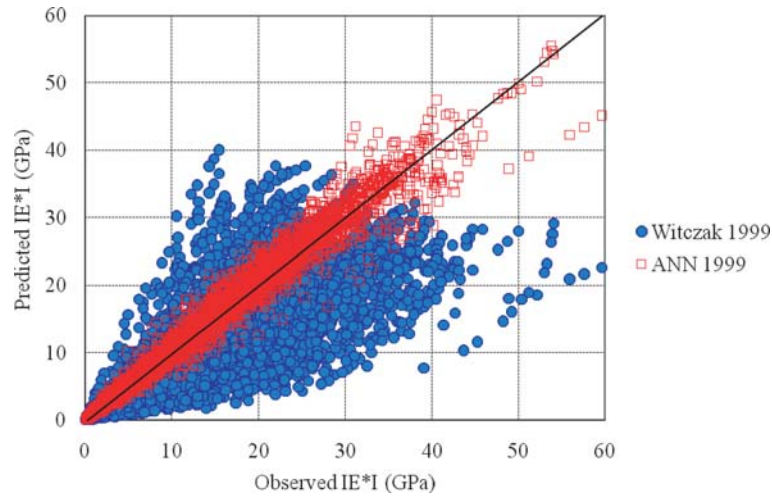


Figure 33. Comparison of Witzak 1999 model with ANN algorithm.

Table 21. Input data for the 2006 Witzak model (magnitude of the shear modulus of the binder and its phase angle in degrees).

Input								Output	R ²	
Gradation				Volumetric		Binder Data			Witzak	ANN
3/4 (%)	3/8 (%)	#4 (%)	#200 (%)	V _a (%)	V _{beff} (%)	Log G* 10 ⁶ psi	δ _c deg	E* psi	0.77	0.96

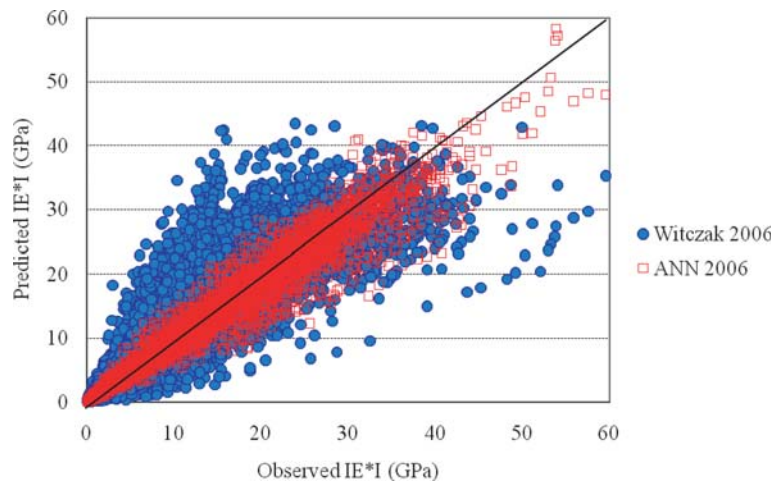


Figure 34. Comparison of Witzak 2006 model with ANN algorithm.

Table 22. Mean CAM model parameters for the four climatic regions.

Climatic Region	ω_{m} (rad/sec)	R	T_d (°C)	C_1	C_2	G_g (Gpa)
Wet-Freeze	0.01516	1.935	-5.8	31.57	199.2	0.861
Wet-No Freeze	7.06E-05	2.261	-6.41	42.49	259.3	0.906
Dry-Freeze	0.001397	2.286	-6.22	38.77	239.0	1.571
Dry-No Freeze	0.000845	2.032	-6.07	41.55	266.9	0.532

user may input these six properties with Level 1 input. In Level 2 input, the user may specify the Performance Grade (PG) of the binder and the climatic region in which the overlay is to be placed and the program will internally calculate the six CAM parameters that correspond to the PG specified. In Level 3 input, the user only needs to specify the climatic region where the overlay will be built. These simplifications can be made because the mean values of the six CAM parameters for each of the four climatic regions in North America are stored. A total of 48 sets of CAM parameters were measured on binders extracted from cores (4); the mean values for each of the climatic regions are listed in Table 22.

The use of the ANN algorithms permits the calculation of the magnitude and phase angle of a mixture modulus at any temperature and loading rate. The input of mixture moduli at different loading times to the viscoelastic thermal stress subprogram is also generated by use of the ANN algorithm.

Models of Tensile Strength of Mixtures

The tensile strength of a mixture depends upon the temperature and loading rate application. In order to have a realistic estimate of the tensile strength of a mixture in the field, the relationships between the mixture modulus and tensile strength that were measured in earlier research (4) were used and converted from the U.S. Customary units to the International System (SI) of units. The relationship developed for the slowest rate (0.005 in./min) was used for the thermal fracture properties (Equation 23) and that developed for the most rapid rate (0.5 in./min) was used for the traffic fracture properties (Equation 24).

$$\sigma_t = 6.895 \left[\frac{E(t, T) \times 1000}{6.895 \times 21.3} \right]^{1.95} \quad (23)$$

$$\sigma_t = 6.895 \left[\frac{E(t, T) \times 1000}{6.895 \times 45.5} \right]^{1.56} \quad (24)$$

Where $E(t, T)$ designates the mixture modulus in MPa and the σ_t designates tensile strength in kPa.

Models of Paris and Erdogan's Law Fracture Coefficients A and n

Earlier studies (4) provided formulas for the Paris and Erdogan's Law fracture coefficients A and n which were found to work well for predicting reflection cracking without being altered. The formulas presented in these studies had been calibrated to field fatigue cracking data in each of the four climatic zones. The form of the equations for both A and n were taken from viscoelastic crack growth theory by Schapery (36, 37) (some details on developing these formulas using a Systems Identification method are presented in Appendix J).

$$n = g_0 + \frac{g_1}{m_{\text{mix}}} \quad (25)$$

$$\log A = g_2 + \frac{g_3}{m_{\text{mix}}} \log D_1 + g_4 \log \sigma_t \quad (26)$$

$$D_1 = \frac{\sin(m_{\text{mix}} \pi)}{E_1 m_{\text{mix}} \pi} \quad (27)$$

$$\log(E(t, T)) = \log(E_1) - m_{\text{mix}} \log(t) \quad (28)$$

where

m_{mix} = the log-log slope of the mixture modulus versus loading time graph for the current temperature and loading rate;

$E(t, T)$ = the mixture relaxation modulus (in MPa) at loading time, t (in sec.), and temperature, T (in °C);

D_1 = the coefficient of the mixture creep compliance expressed in a power law form (in kPa^{-1}); and

σ_t = tensile strength (in kPa).

The magnitudes of the Complex Modulus at three different loading times, t , which are set at one log cycle apart and at the current temperature, were determined by the selected ANN Witczak model and fit by linear regression to produce the values of E_1 and m_{mix} that are used in defining the current value of the Creep Compliance coefficient, D_1 . The values of D_1 and m_{mix} and the tensile strength, σ_t , which is computed from the current value of $E(t, T)$ are then used in the Schapery

Table 23. Climatic zone variations of fracture and healing coefficients for HMA.

Coefficient	Climatic Zone			
	Wet-Freeze	Wet-No Freeze	Dry-Freeze	Dry-No Freeze
g_0	-2.09	-1.429	-2.121	-2.024
g_1	1.952	1.971	1.677	1.952
g_2	-6.108	-6.174	-5.937	-6.107
g_3	0.154	0.19	0.192	1.53
g_4	-2.111	-2.079	-2.048	-2.113
g_5	0.037	0.128	0.071	0.057
g_6	0.261	1.075	0.762	0.492

equation for the logarithm of the Paris and Erdogan's Law coefficient, A .

Healing Coefficients

In addition to the fracture coefficients, the healing coefficients obtained in earlier studies (4) are used to account for the healing shift function that occurs between the traffic loads on the overlay. The healing shift function is

$$SF_{healing} = 1 + g_5 (\Delta t_{rest})^{g_6} \quad (29)$$

The rest period in seconds between load applications is calculated as the number of seconds in a day (86,400) divided by the average daily traffic in vehicles per day. Values for the coefficients g_0 through g_6 were determined for each of the four climatic zones; these are listed in Table 23 (4). These coefficients were used without alteration and the fracture coefficients g_0 through g_4 were applied without modification to determine both the thermal and traffic fracture properties. The healing coefficients were used only with the traffic crack growth equations.

Stress Wave Pattern Correction for Viscoelastic Crack Growth

Schapery's theory of crack growth in viscoelastic materials takes into account the loading time and the shape of the stress pulse during the time that the material is being loaded (30, 31). The normalized wave shape, $w(t)$, has a peak value of 1.0. The wave shape rises to 1.0 and falls back to zero in a length of time, Δt . The correction term for viscoelastic crack growth a_k is given by the following equation.

$$a_k = \int_0^{\Delta t} w(t)^n dt \quad (30)$$

The exponent, n , is the Paris and Erdogan's Law exponent which is given in Equation 25 and is typically between 2 and 6. If the applied load is a square wave, the integral is equal

to 1.0. If the stress wave is a rising and falling shape as is commonly the case with traffic and thermal stresses, the value of a_k is usually considerably less than 1.0. Appendix F shows the patterns of the rise and fall of the stress waves caused by the passage of single, tandem, tridem, and quadrem axles. These patterns were used in determining the effect during each day of each set of axle groupings on the growth of reflection cracks.

Computational Method for Crack Growth Due to Traffic

Although the SIF for bending and shear occur at the same time under traffic loads, the crack growth technique adopted in this project calculates the growth of cracks due to each of the two stresses separately. Thus, Paris and Erdogan's Law for bending and shearing are provided by Equations 31 and 32, respectively.

$$\frac{dc}{dN} = A [K_{I1}(\text{bending})]^n [a_k(\text{bending})] \quad (31)$$

$$\frac{dc}{dN} = A [2K_{II1}(\text{shearing})]^n [a_k(\text{shearing})] \quad (32)$$

The wave patterns for a_k —the viscoelastic factor—are shown in Appendix F for each of the types of traffic loading: bending and shearing and each of the four axle groupings. With shearing stresses, there is a peak shearing stress as the leading edge of the tire approaches the reflection crack and then another peak shearing stress of a different sign as the trailing edge of the tire leaves the location of the reflection crack. Thus there are two peak shearing SIF with the passage of a single tire. Examples of these patterns are shown in Figures 35 and 36 for bending and shearing, respectively.

The time increment, Δt , for the tridem axle group to pass over a given point on a pavement is given in Equation 33.

$$\Delta t(\text{sec}) = \frac{18 + L_j}{V} \left(\frac{\text{ft}}{\text{ft/sec}} \right) \quad (33)$$

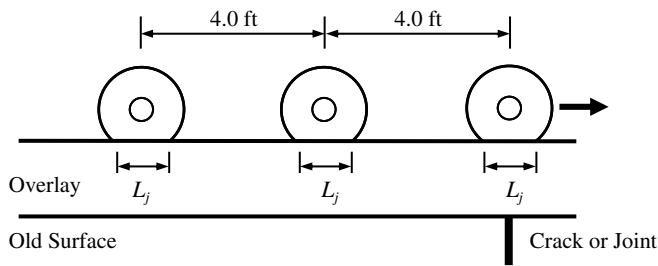


Figure 35a. Bending loading pattern for a tridem axle.

The incremental crack growth each day is calculated from the accumulated effects of all of the traffic that have passed over the reflection crack during that day as follows:

$$dc = \sum_{i=1}^{i=n} A(K_{II})^n (a_{ki}) dN_i \left(\frac{1}{SF_{healing}} \right) \text{ for bending and} \quad (34)$$

$$dc = \sum_{i=1}^{i=n} A(2K_{III})^n (a_{ki}) dN_i \left(\frac{1}{SF_{healing}} \right) \text{ for shearing} \quad (35)$$

Crack length, c_n on the n th day of this crack growth process is the sum of all of the n incremental crack growth increments:

$$c_n = \sum_{i=1}^{i=n} \Delta c_i \quad (36)$$

When the sum of the bending crack increments reaches the point in the overlay where the bending stresses become compressive, that defines what is termed "Position 1." At crack

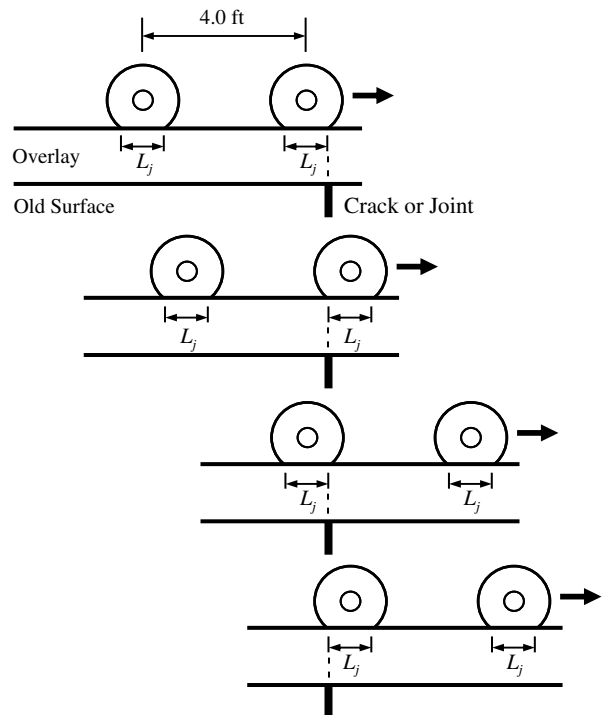


Figure 36a. Shearing loading pattern for a tandem axle.

lengths above this point, bending stresses no longer contribute to the growth of cracks and crack growth is due only to thermal and shearing stresses. The number of days that are required for cracks caused by each type of stress to reach Position 1 are recorded. Then the number of days required to grow a crack from Position 1 to the surface of the overlay because of shear

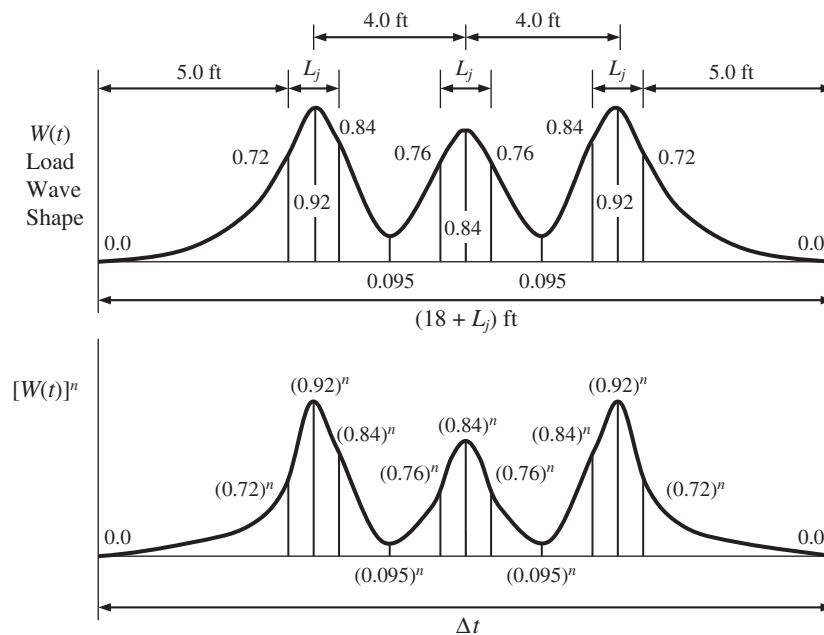


Figure 35b. Normalized SIF and a_k wave patterns for tridem bending loading.

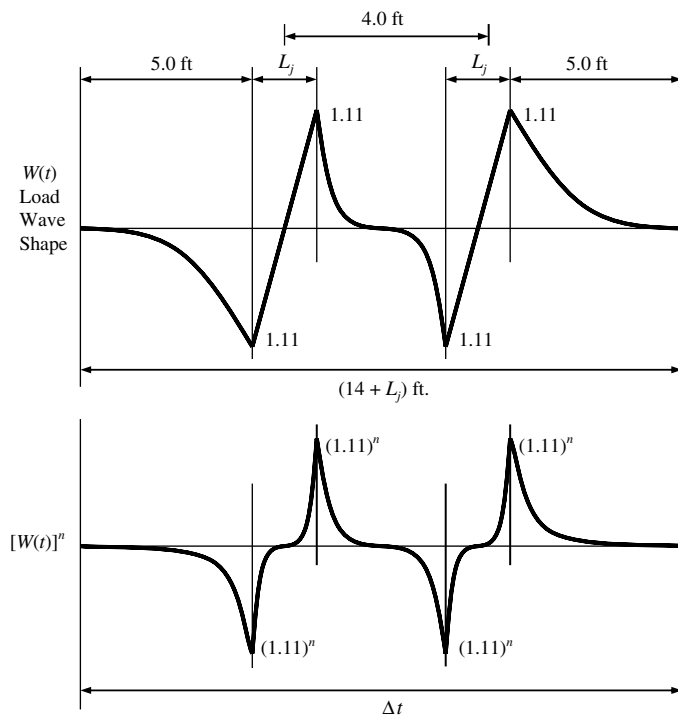


Figure 36b. Normalized SIF and a_k wave patterns for tandem shearing loading.

and thermal stresses is computed. This gives a total of five numbers of days that are computed and recorded in the process of growing a reflection crack up through an overlay. All five numbers of days are used in the calibration equations to estimate the values of ρ (the scale parameter) and β (the shape parameter) of the observed field cracking data.

Computational Method for Viscoelastic Thermal Stresses

In determining the thermal viscoelastic modulus of an in-service mixture for use in calibrating the program, Falling Weight Deflectometer (FWD) data was used to determine the modulus of the overlay and the mixture temperature at the time of the measurement. The overlay asphalt mixture was used in the 2006 Witczak modulus model to calculate the modulus of the mixture. Discrepancy between the FWD modulus and that predicted by the Witczak 2006 model (3) at the same temperature was ascribed to the rubbery stiffness of the mixture, E_∞ .

$$E(t, T)_{FWD} = E_\infty + E(t, T)_{2006} \quad (37)$$

If the stiffness of the Witczak 2006 model was greater than the FWD back calculated modulus, the value of E_∞ was set to zero. Otherwise, the value of E_∞ was used in calculating the master curve of the relaxation moduli at 11 different loading times to

make use of the viscoelastic thermal stress computation algorithm (38). The details of the viscoelastic thermal stress computation are given in Appendix I. It makes use of Dirichlet series (Equation 38) to represent the master curve of the relaxation modulus of the asphalt mixture at any loading time, t .

$$E(t_r) = E_\infty + \sum_{i=1}^n E_i e^{-\frac{t_r}{T_i}} \quad (38)$$

where t_r is the reduced time of the master curve of the relaxation modulus of the asphalt mixture. The Dirichlet series coefficients, E_i , and relaxation times, T_i , are determined with a collocation process using the Witczak 2006 mixture model (3) and the E_∞ is determined from the analysis of the FWD field data. Within the program, the temperature and relaxation modulus of the overlay at the current tip of the growing reflection crack is calculated for each day, and then used to calculate the viscoelastic thermal stress at the tip of the crack, the thermal SIF, and the incremental growth of the crack that occurs that day. The actual thermal loading time is converted to a reduced loading time using the Williams-Landel-Ferry (WLF) time-temperature shift (39). As with the growth of cracks due to traffic stresses, the incremental crack growth each day is accumulated until Position 1 is reached. The number of days required to reach Position 1 is recorded as is the number of days required for the crack to grow up the rest of the way to the overlay surface. These two numbers of days are used in the calibration equations to estimate the value of ρ , the scale parameter of the observed field cracking data.

The viscoelastic thermal stress is calculated using a Boltzmann Superposition Integral in numerical form (details of this calculation are given in Appendix I). The general form of the thermal stress integration is

$$\sigma(t_r) = \int_{\tau=0}^{\tau=t_r} E(t_r - \tau) \frac{\partial(\epsilon - \alpha\Delta T)}{\partial\tau} d\tau \quad (39)$$

The initial strain ϵ is calculated relative to the defining temperature of the master curve T_0 , and the remaining thermal strain value $\alpha\Delta T$ is the hourly change of thermal strain. It is the rate of change of the difference between ϵ and $\alpha\Delta T$ that accumulates the thermal stress at the tip of the growing thermal reflection crack. The thermal stress at the tip of the crack is calculated for every hour of each day and the highest calculated stress is used to calculate the thermal SIF and the incremental growth of the reflection crack for that day. Paris and Erdogan's Law coefficients were calculated using the modulus for the critical time and temperature each day to calculate the D_1 , m_{mix} , and σ_t values. The Δt was set at one 1 and the a_k was set at 1.0 for the thermal case.

The values for the coefficient of thermal expansion (contraction) α can be input at Level 1 and Level 3. The Level 3 input is the mean value of the thermal coefficients that were

Table 24. Level 3 thermal coefficients.

Climate Zone	Thermal Coeff. α	Absorption	Emissivity	Albedo
Wet-Freeze	0.0000248	0.7468	0.6628	0.3027
Wet-No Freeze	2.287E-05	0.7381	0.6571	0.1988
Dry-Freeze	0.00002298	0.7357	0.6071	0.2429
Dry-No Freeze	2.468E-05	0.7000	0.5750	0.2000

used in the earlier research for each of the four climatic zones (4). In addition, the absorption, emissivity, and albedo coefficients for the same climatic zones may be input at Level 1 and Level 3. Table 24 gives the mean values for these coefficients. Absorption, emissivity, and albedo coefficients vary throughout the United States and with the seasons (detailed values are given in Appendix B).

Supervisory Program to Compute Crack Growth

The supervisory program for the separate analysis of the growing reflection cracks by each of the three mechanisms (bending, shearing, and thermal stress) takes into account all of the identified details and produces five numbers of days to reach a defining point in the growth of a reflection crack up through an overlay. One defining point is Position 1, at which point bending produces no additional crack growth. The other defining point is the surface of the overlay. The five numbers of days are the number of days to reach Position 1 by bending, shearing, and thermal stress and the number of days for the crack to grow from Position 1 to the surface of the overlay because of shearing and thermal stress.

The supervisory program handles each of the crack growth processes separately and combines them after the calculations for each of the three separate mechanisms have been completed. Figures 37, 38, and 39 illustrate the calculation processes for thermal stress, bending, and shearing, respectively. In all cases, the initial crack length was taken to be the depth of the old pavement surface layer. In all crack growth calculations, the initial crack size, c_0 , is assumed to be the thickness of the overlaid pavement surface layer. This value enters into the calculation of the SIF at the tip of the crack each day.

User Interface Program for Input and Output Data

The input and output user interface for this program has been designed to have the same appearance as the user interface for the MEPDG software. An example of an input screen showing the input of a pavement layered structure is given in Figure 40. The user output is a graphic plot of the three severity level distress curves for reflection cracking, if the original field data had a sufficient amount of observed data to include high,

medium and low levels of severity (details of the various options for input and output are given in Appendix O).

Computation-to-Field Calibration Coefficients

At the end of the computations, there are five calculated numbers of days for a crack to reach a designated point within an overlay (Position I) where the bending stresses become compressive and no longer cause crack growth (Position II, the surface of the overlay). These five numbers of days are illustrated in Figure 41.

These five numbers of days can be combined in several ways to model the value of ρ , the scale parameter of the amount, and severity of the observed reflection cracking distress. One way of modeling the ρ -value is to assume that the principal cause of reflection cracking is bending stress and another way is to assume that shearing stress is the principal cause of reflection cracking. In both cases, it becomes necessary to find how many days of each of the other types of cracking are the equivalent of the number of days of the principal cause of the distress. This concept is illustrated in Figure 42 which shows all three ρ -values (i.e., ρ_{LMH} , ρ_{MH} , and ρ_H). The linear regression form of the model for the ρ_{LMH} -value assuming that bending stress is the principal cause of the reflection cracking up to Position I and shearing is the principal cracking mechanism from Position I up to the surface of the overlay, is presented in Equations 40 through 42.

The thermal calibration model for the low+medium+high distress curve is given by Equation 40.

$$\rho_{LMH} = N_{fB1} \left(\alpha_0 - \alpha_1 \frac{N_{fB1}}{N_{fT1}} - \alpha_2 \frac{N_{fB1}}{N_{fS1}} \right) + N_{fT2} \left(\alpha_3 - \alpha_4 \frac{N_{fT2}}{N_{fS2}} \right) \quad (40)$$

Calibration Coefficients: $\alpha_0, \alpha_1, \alpha_2, \alpha_3, \alpha_4, \beta_{LMH}$

The thermal calibration models for the Medium + High and High distress curves are given by Equations 41 and 42, respectively.

$$\rho_{MH} = N_{fB1} \left(\alpha_5 - \alpha_6 \frac{N_{fB1}}{N_{fT1}} - \alpha_7 \frac{N_{fB1}}{N_{fS1}} \right) + N_{fT2} \left(\alpha_8 - \alpha_9 \frac{N_{fT2}}{N_{fS2}} \right) \quad (41)$$

Calibration Coefficients: $\alpha_5, \alpha_6, \alpha_7, \alpha_8, \alpha_9, \beta_{MH}$

$$\rho_H = N_{fB1} \left(\alpha_{10} - \alpha_{11} \frac{N_{fB1}}{N_{fT1}} - \alpha_{12} \frac{N_{fB1}}{N_{fS1}} \right) + N_{fT2} \left(\alpha_{13} - \alpha_{14} \frac{N_{fT2}}{N_{fS2}} \right) \quad (42)$$

Calibration Coefficients: $\alpha_{10}, \alpha_{11}, \alpha_{12}, \alpha_{13}, \alpha_{14}, \beta_H$

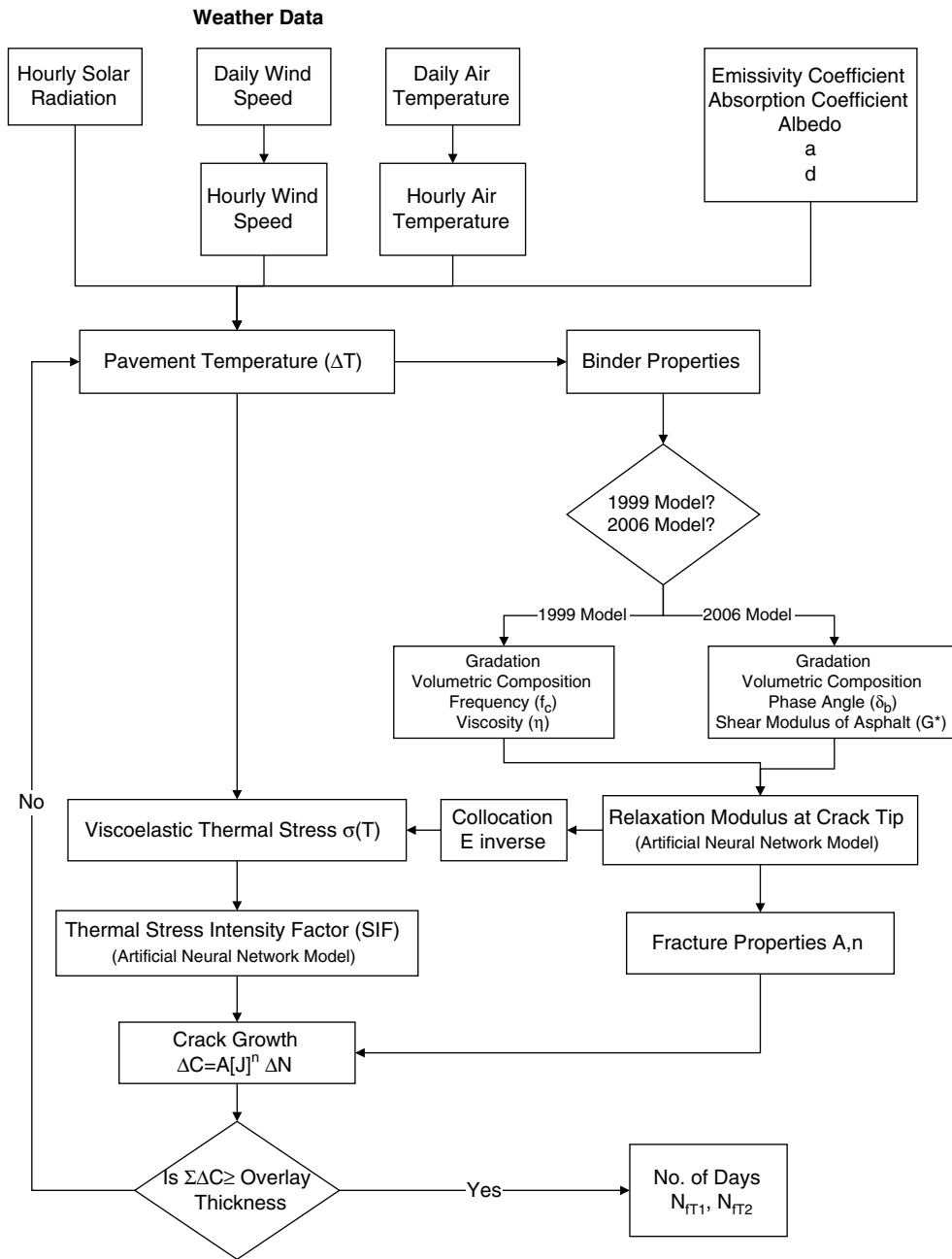


Figure 37. Flow chart of the thermal crack growth computations.

A similar set of coefficients can be derived by linear regression analysis, assuming that bending is the principal mode of reflection cracking until it reaches Position I and then shearing stress is the principal mode of reflection cracking from Position I to the surface of the overlay. An example of this assumed calibration form is shown in Equation 43.

$$\rho_{LMH} = N_{fB1} \left(\alpha_0 - \alpha_1 \frac{N_{fB1}}{N_{fT1}} - \alpha_2 \frac{N_{fB1}}{N_{fS1}} \right) + N_{fS2} \left(\alpha_3 - \alpha_4 \frac{N_{fS2}}{N_{fT2}} \right) \quad (43)$$

The calibration coefficients are, as in the first form of this model, $\alpha_0, \alpha_1, \alpha_2, \alpha_3$ and α_4 . Similar models are assumed for the scale parameters ρ_{MH} and ρ_{HS} ; similar linear regression models were used to model the shape parameter, β .

In performing the calibration analysis, the thermal, bending, and shearing forms of equation were tried and the one which proved to have the highest coefficient of determination, R^2 , was selected. In general, the model with bending as the principal cracking mechanism up to Position I and thermal stress as the principal cracking mechanism from there to the surface of the overlay had the highest R^2 -value with all

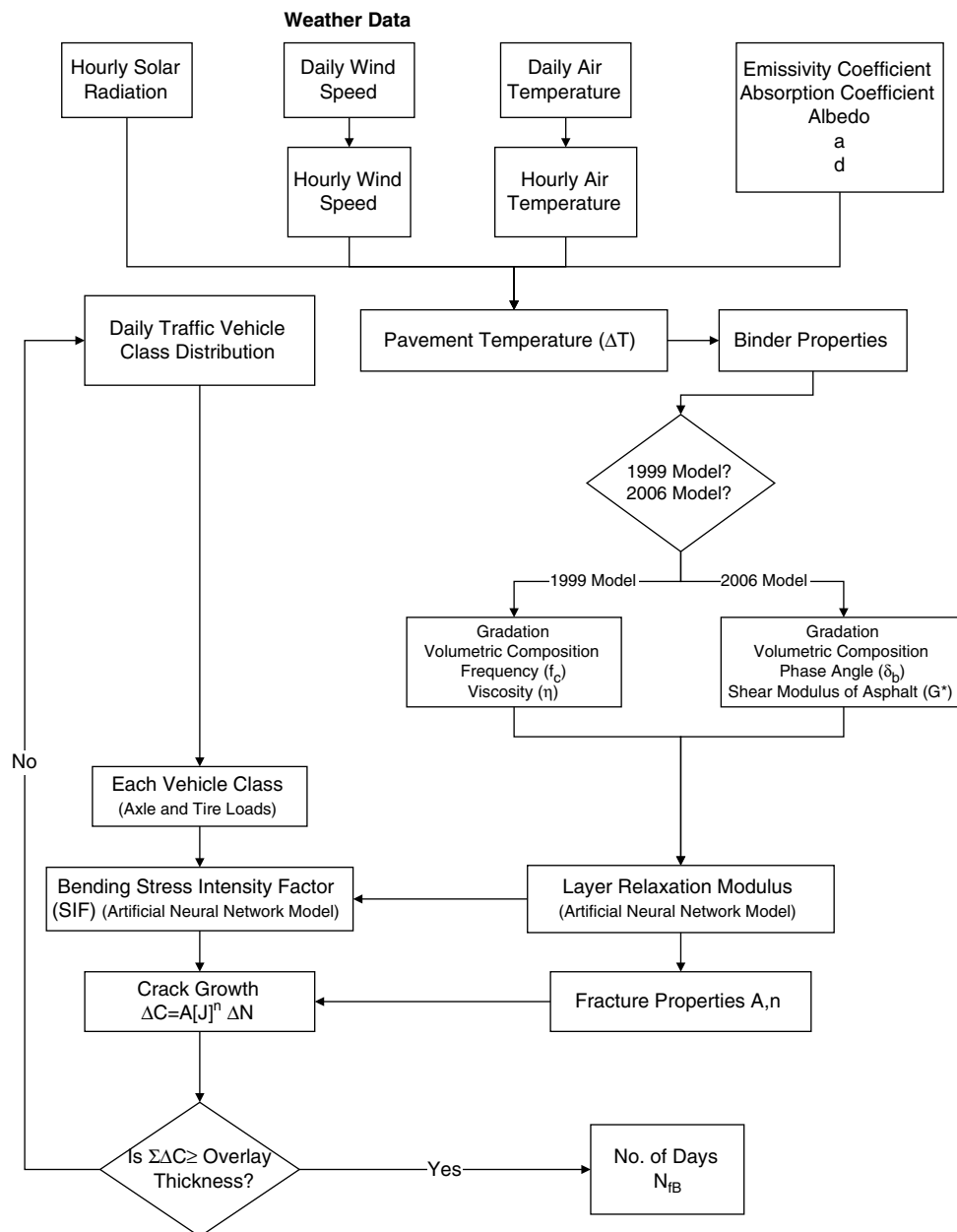


Figure 38. Flow chart of the bending crack growth computations.

overlay types except one. The exception was the AC overlay with reinforcing over AC in the Dry-Freeze Zone. Bending was the principal crack growth mode up to Position I in this model. Shearing was the principal cracking mode from Position I to the overlay. An example of this latter model is in Equation 43.

The complete set of calibration coefficients for each of the types of pavement structures and overlays and the statistical measures of their fit to the observed data is provided in Appendix N. In some cases, no distress was observed at the high severity level and in other cases, only low severity distress was observed. In such cases, the calibration coefficients for

the reflection cracking model were limited to those sets which were actually observed.

A separate calibration program was assembled to assist in the development of other regional computational model-to-field data calibration coefficients (a User's Guide to this Calibration Program is presented in Appendix P).

Validation of the Calibration Coefficients

In reviewing the detailed data for each of the test sections, it was determined that there were only 150 overlay sections with unique data. In some cases multiple sections were located

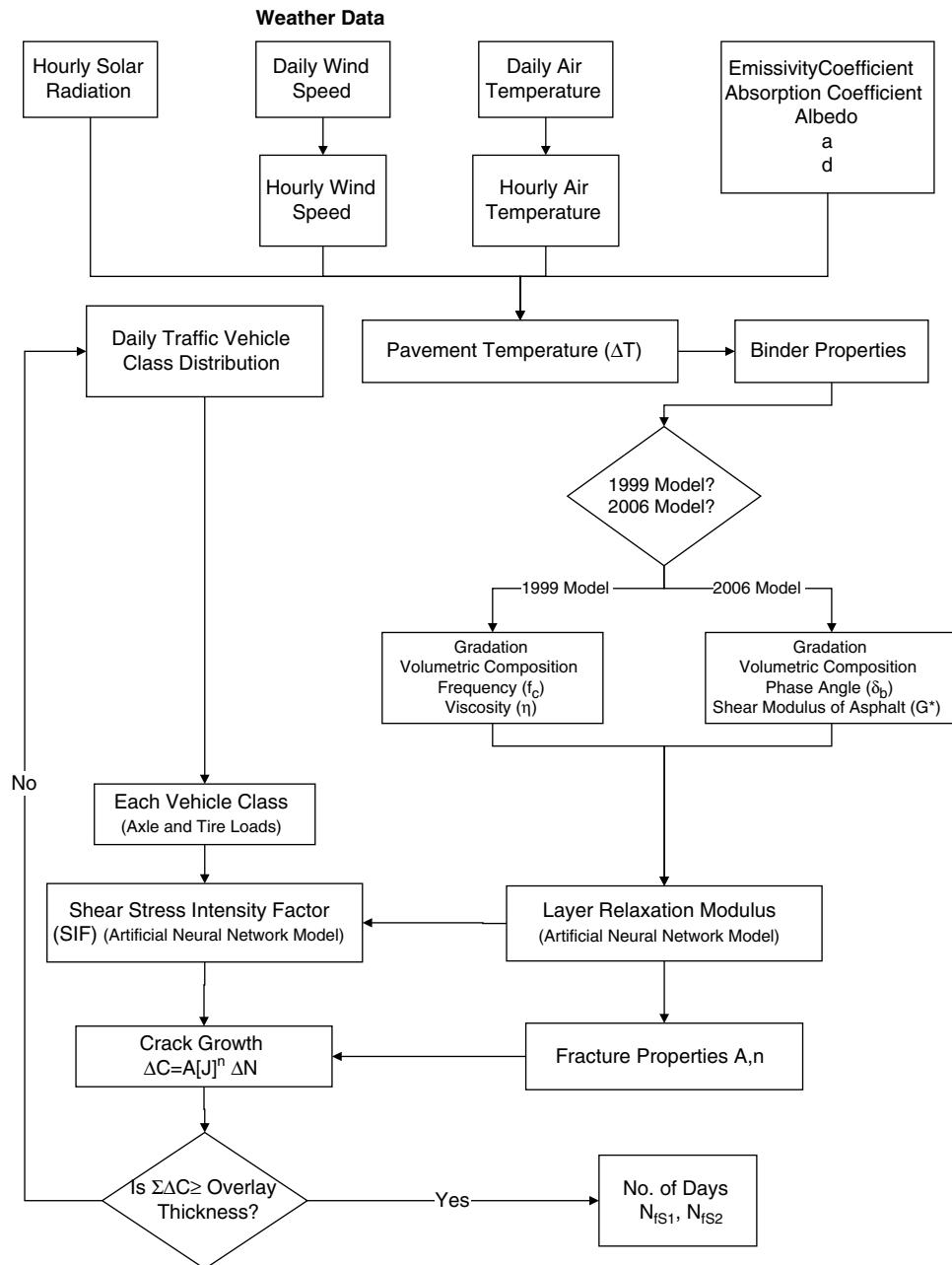


Figure 39. Flow chart of shearing crack growth computations.

on the same highway (i.e., each with the same traffic, climate, and pavement structure). Therefore, the calibration and validation process was conducted in a different way than was initially envisioned. It was planned to separate the overlay sections of each type into two groups: one group would be used to develop the calibration coefficients and the other group would be used to verify that their distress accumulation could be satisfactorily predicted. The small number of unique pavement-overlay sections did not permit splitting the sections into two such groups. Instead, it was necessary to use the observed data of all of the sections in both developing the calibration coeffi-

cients by regression analysis and comparing the set of coefficients with the original field data. If the set of calibration coefficients reproduced the original observed scales, trends, and patterns of ρ and β values with a high coefficient of determination (R^2) and with an acceptable scatter pattern around the line of equality, the set of coefficients were accepted as valid. If they did not produce an acceptable fit to all of the original observed ρ and β values, then the calibration coefficients were revised by trying a new model with bending or shearing as the principal distress mode. The model with the highest coefficient of determination (R^2) was selected. No separate validation

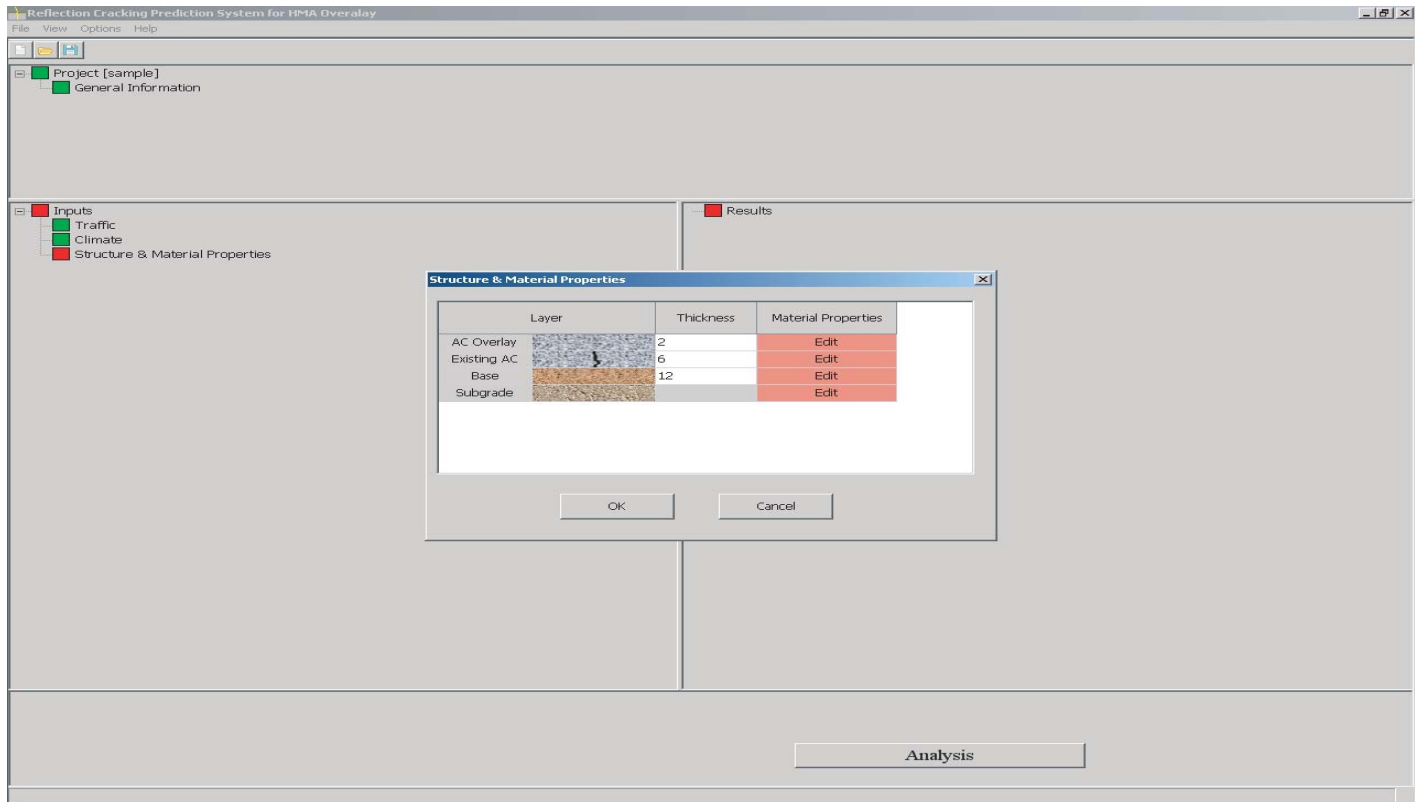


Figure 40. Example user input screen for the reflection cracking program.

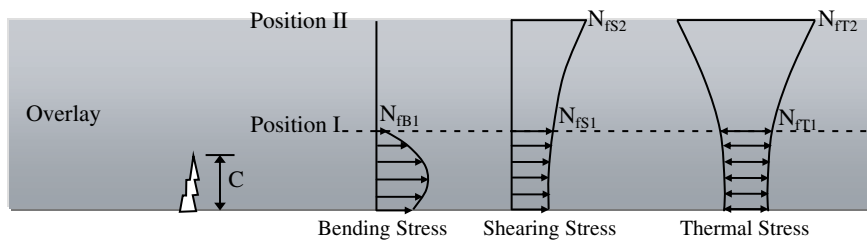


Figure 41. Definition of the number of days of crack growth.

- N_{FB1} = Number of days for crack growth due to bending to reach Position I.
- N_{FT1} = Number of days for thermal crack growth to reach Position I.
- N_{FS1} = Number of days for crack growth due to shearing stress to reach Position I.
- N_{FT2} = Number of days for thermal crack growth to go from Position I to Position II.
- N_{FS2} = Number of days for crack growth due to shearing stress to go from Position I to Position II.

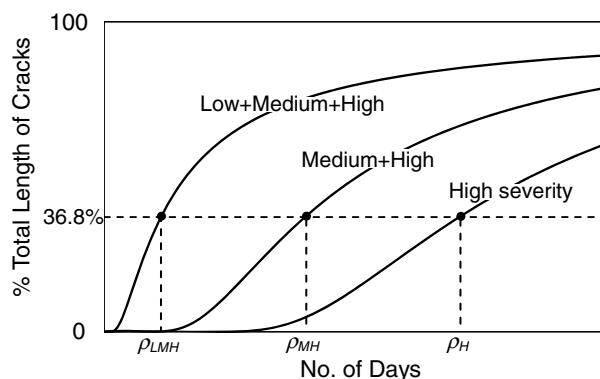


Figure 42. Illustration of amount and severity of reflection cracking distress curves.

process was pursued with the limited number of overlay test sections that was available.

The purpose of validation is to check if the equations derived by regression analysis correctly fit the observed scales, trends, and patterns of the field data. Validation is required because the regression analysis assumes that all of the error is in the observed dependent values and not in the independent variables. In this case, the independent variables were pre-

dicted using fracture mechanics concepts and material properties which are based on tabulated asphalt mixture, pavement structure, traffic and climatic variables. Thus, there are likely to be errors in the independent variables as well as in the dependent variables (i.e., the values of ρ and β which were fitted to the observed distress).

A total of 33 possible sets of calibration coefficients could have been developed if low, medium, and high levels of cracking severity had been observed in all pavement types. Because some of these severity levels were missing, a total of 24 sets of calibration coefficients were developed (all of the sets of calibration coefficients are found in Appendix N).

After arriving at a final set of calibration coefficients, a further quality control step was taken by graphically plotting the distress patterns for all of the test sections to make certain that the predicted patterns of distress accumulation were both reasonable and realistic. Logical tests were programmed into the design program to make certain that the predicted distress patterns will be correctly ordered from low to medium to high levels of distress. Examples of the final predicted values of ρ and β plotted against the observed field values are provided in the Chapter 3 (full set of such plots is provided in Appendix N).

CHAPTER 3

Interpretations, Appraisal, and Applications

Introduction

This project developed a HMA overlay design program which is based on calibrating mechanistically predicted reflection cracking lives to observed overlay reflection cracking distress. The program is written to be a subprogram to the MEPDG software for new pavements. The program uses the same input and type of input that the MEPDG software requires and additional data that is appropriate to the design of an overlay. This includes the condition of the pavement at the time of the overlay construction and the properties of the layers of the old pavement, which may be assumed or measured by nondestructive testing means. The design subprogram permits the user to make exploratory runs with trial mix designs, thicknesses, and reinforcing or strain-absorbing interlayers. As with the MEPDG, the overlay design subprogram requires the traffic to be input as an axle load spectrum. Over 150 separate weather databases were assembled in the course of this project and are incorporated into the files available to the user of this subprogram in addition to others that may be generated using the Enhanced Integrated Climatic Model (EICM). All data may be input at one of three levels of detail selected by the user (Levels 1, 2, or 3).

The project has also developed a model calibration program which may be used to create a set of calibration coefficients, for use in the design model, to design overlays calibrated to specific local or regional conditions and practices.

The design program is arranged as a single mechanistic crack growth model with different sets of calibration coefficients for overlays in different climatic zones or with a different pavement structure, such as overlays over cracked asphalt surfaces or over jointed concrete pavements. A total of 11 separate types of pavements were identified with a sufficient amount of quality data to develop sets of calibration coefficients. The final set of calibration coefficients for each type of overlay was selected to reproduce, as closely as possible, the actual field observations of the growth of reflection cracking distress in both its extent and

severity. The process by which these sets of model calibration coefficients were developed is described in Chapter 2 (more details are provided in Appendices L, M, and N).

Twenty two sets of calibration coefficients were developed, two sets for each combination of overlay and climatic zone (for which data were available).

The Model Development Process

The application of mechanics to the prediction of reflection cracking through HMA concrete overlays involves a number of steps including the use of finite element analysis of crack growth and the modeling of those results with an ANN algorithm to speed up the computational time. The computational task of determining the material properties of the overlay under a variety of loading conditions and temperatures, including traffic and thermal stresses, must be done rapidly to make the design model a practical tool for design. A third part is to generate accurate weather characteristics that can be used to provide realistic material properties and stresses throughout each day and over the observed service life of an overlay. A fourth part of the assembly of this model is to develop a consistent means of describing the distress observed in the field. The fifth part was to devise a means to relate the predicted distress to the observed distress in a simple way, and produce predicted distress that matched well with what was actually observed in the field. A discussion of these five steps follows.

Mechanistic Prediction of Crack Growth

The model was selected for the Design Program based on several factors. One of the most important factors was the speed with which daily crack growth could be computed to facilitate consideration of several material, thickness, and reinforcing options in the overlay. This led to the decision to use the ANN algorithms to compute both the changing modulus of the overlay mix and the growth of the cracks up from the

cracks in the existing pavement and to develop mechanistic data with which to “train” the ANN algorithms for crack growth. This was done by calculating a large set of stress intensity factor data for a variety of overlay and pavement structures using a two-dimensional finite element approach with the transverse third dimension being represented by a series solution. When the calculated results were compared to the correct answers generated by a full three-dimensional set of computational results, the errors were acceptably small (discussion is provided in Appendix Q). The ANN models were found to fit all 18 sets of computed databases very well (as described in Appendix F). Neither the two- nor the three-dimensional finite element analysis was used within the Design Program because of the long computational time that each requires.

HMA Overlay Material Properties

The ANN algorithms were also used for generating the material properties of a HMA overlay material as it responds to traffic and thermal stresses. It was also necessary to use a well constituted and widely available database of HMA material properties to represent these properties. The database assembled and modeled by Witczak in 1999 and 2006 (2, 3) satisfied these criteria. Representing both models by an ANN algorithm provided two models that were computationally fast yet have a better coefficient of determination (R^2) than Witczak’s regression models. By inputting binder properties, some aggregate gradation, volumetric composition of the mix, and frequency of loading and temperature into these ANN algorithms, HMA mixture properties over a wide range of loading times and temperatures can be generated quickly. The binder properties used as reference properties within the program were binder properties extracted from field cores and reported earlier (4). Although the user may input other binder properties at the detailed Level 1 input, binder data from actual constructed pavements may be used for Level 2 or 3. The PG of the binder and the internal reference data may be used for Level 2 to generate the remainder of the required data.

The fracture properties of an asphalt mixture depend on simpler and more fundamental properties of that mixture as shown by Schapery (36, 37) and confirmed in other studies (4), which calibrated to field fatigue cracking data. The calibration coefficients that were developed in these studies were used in this project without any alteration, even though the type of distress was different.

Weather Data and Temperature Prediction

Accurate temperature prediction is key to making accurate predictions of thermal crack growth, especially in an overlay. Comparisons, between the temperature predictions and actual temperatures measured in the field, demonstrated the need for a higher degree of accuracy in calculating the temperature

within the overlay. Such a temperature model was incorporated into the Design Program (characteristics of this model are described in detail in Appendix B). The temperatures calculated by this program and those measured in the field rarely differed by more than 2° C. A complete set of weather data were assembled from databases available to the public for about 150 different locations within the United States and Canada for use in the Design Program.

Consistent Description of Reflection Cracking Distress

The S-shaped curve for the accumulating extent of reflection cracking adopted in this project matches the pattern that is observed in the progressive development of many kinds of distress. There are three curves that represent the extent and severity of the reflection cracks as they are observed in the field. The curves show the one growth of the high severity reflection cracks; the sum of the percentages of the high and medium severity cracks; and the sum of percentages of the high, medium, and low severity cracks. Each curve is plotted against the percent of the original length of transverse cracks in the old pavement surface. The difference between the curves represents the percentages of the individual levels of distress severity. This S-shaped curve is defined by two parameters: ρ , the scale parameter, and β , the shape parameter. The scale parameter is the number of days required for the percentage of reflected cracks to reach 36.8 percent (i.e., $1/e$), of the original length of the transverse cracks or joints in the old pavement surface. The shape parameter determines how steep the growth of the curve is as it reaches the 36.8 percent mark.

This method allows a simple, consistent, and comprehensive description of the distress history of an overlay. It also makes the task of calibrating the calculated reflection cracking lives, due to traffic and thermal stresses to the field observations, possible.

Calibration of Calculated Overlay Life to the Observed Distress

The two-step method used to develop calibration coefficients first involved linear regression analysis and observation of the patterns of the predicted versus the observed values of both ρ and β . If the coefficient of determination (R^2) was acceptable and the scatter of the data was clustered around the line of equality, the calibration coefficients were considered acceptable. Otherwise, a second step was undertaken if there was a non-random pattern of scatter around the line of equality or R^2 was unacceptable.

This approach had to be taken because only about 150 of the sections were unique, the rest were similar in pavement features (structure, materials), traffic, and weather, such that

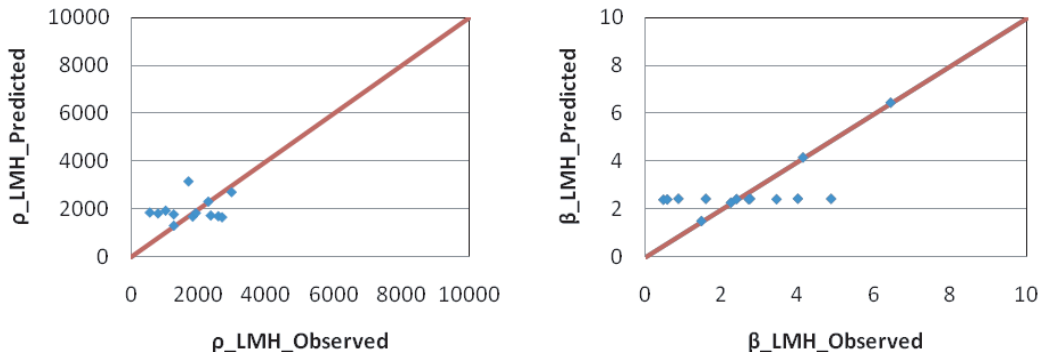


Figure 43. LMH Regression results of ρ and β for AC over AC pavement and Wet-No Freeze climate zone.

there were not enough sections to separate the sections into two categories (calibration sections and validation sections).

The approach taken raises concern about how well the calibrated predictions match the field data. The next section discusses that concern.

Calibrated Results Compared with Observed Field Data

The details of each set of calibration coefficients are provided in Appendices L, M, and N. The scale and shape parameters ρ and β that were fit to the field observations are provided in Appendix M, and the calibration coefficients and plots of the predicted versus the observed values of ρ and β are provided in Appendix N.

Calibration Coefficients by Regression Analysis

Figure 43 shows the predicted versus observed values of ρ and β for HMA overlays over a cracked asphalt surface in a Wet-No Freeze zone.

Figure 44 shows the predicted versus the observed values of ρ and β for a HMA overlay placed over a cracked asphalt pavement surface in the Dry-No Freeze zone.

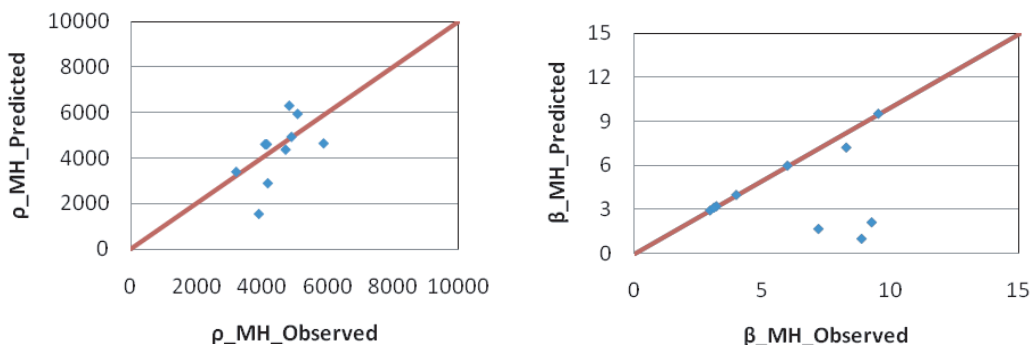


Figure 44. MH Regression results of ρ and β for AC over AC pavement and Dry-No Freeze climate zone.

The details of each set of model calibration coefficients are given in Appendix N.

Figure 45 shows the predicted versus observed values ρ and β for HMA overlays over a cracked asphalt pavement surface in a Wet-Freeze Zone.

Figure 46 shows the predicted versus the observed values of ρ and β for HMA overlays over jointed concrete pavements in a Wet-Freeze Zone.

Figure 47 shows the predicted versus the observed values of ρ and β for HMA overlays with reinforcing interlayers over cracked asphalt pavement surfaces in a Dry-Freeze Zone.

Figure 48 shows the predicted versus observed values of ρ and β for HMA overlays with reinforcing interlayers over jointed concrete pavements in a Wet-No Freeze Zone.

Some of the difference between the predicted and the observed distress in these figures is due to the difference in levels of construction quality control.

Predictions of Overlay Reflection Cracking

Eleven sets of calibration coefficients were developed, one set for each combination of pavement structure and climatic zone for which sufficient data were available. Each set of model calibration coefficients have a maximum of three pairs

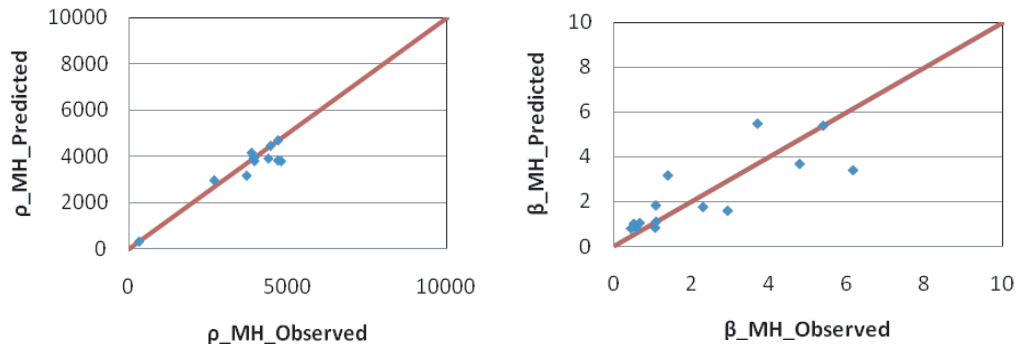


Figure 45. MH Regression results of ρ and β for AC over AC pavement and Wet-Freeze climate zone.

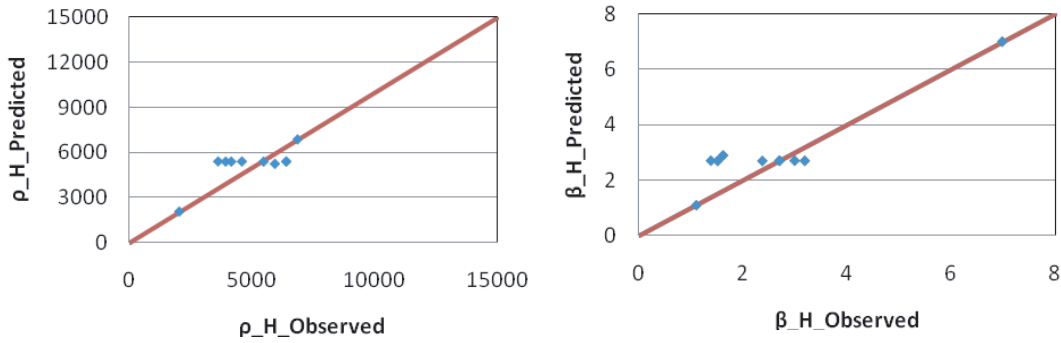


Figure 46. H Regression results of ρ and β for AC over JPC/JRC pavement and Wet-Freeze climate zone.

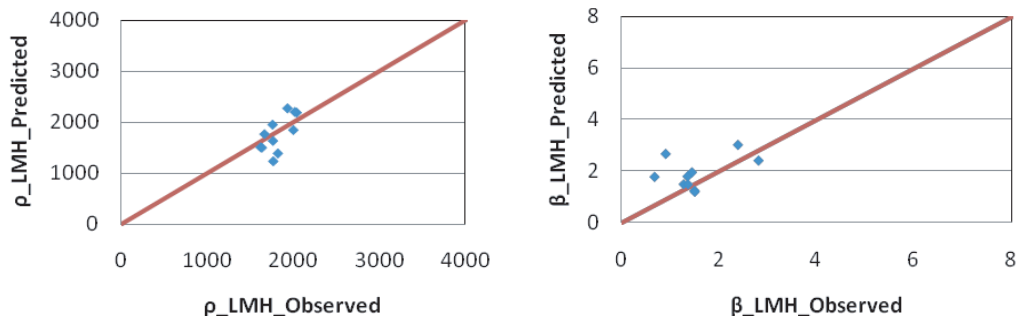


Figure 47. LMH Regression results of ρ and β for AC with reinforcing over AC pavement and Dry-Freeze climate zone.

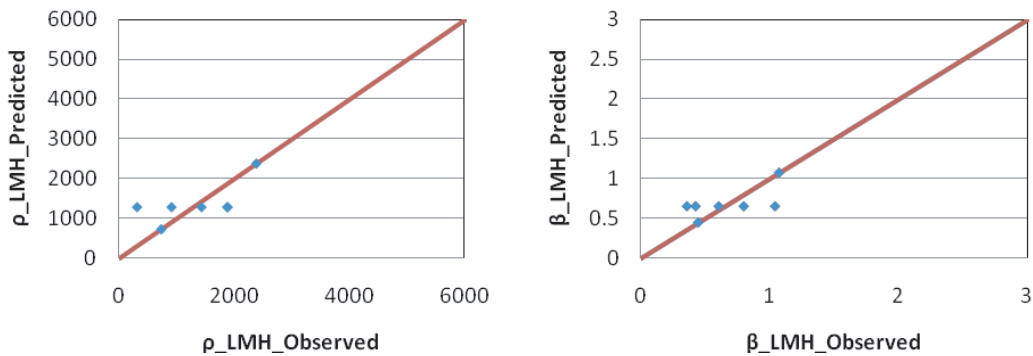


Figure 48. LMH Regression results of ρ and β for AC with Reinforcing over PCC pavement and Wet-No Freeze climate zone.

Table 25. Figures of calculated reflection cracking distress curves.

Figure Number	Overlaid Pavement Type	Climate Zone	Distress Severity Levels
49	Asphalt	WF	L, M, H
50	Jointed Reinforced Concrete	WF	L, M, H
51	Friction Course over Asphalt	WF	L, M, H
52	Continuously Reinforced Concrete	WF	L, M
53	Reinforcing Geosynthetic over Jointed Concrete	W-NF	L
54	Reinforcing Geosynthetic Over Asphalt	DF	L
55	Asphalt	W-NF	L, M
56	Friction Course Over Asphalt	W-NF	L
57	Asphalt	DF	L, M, H
58	Asphalt	D-NF	L, M, H
59	Reinforcing Geosynthetic Over Jointed Concrete	WF	L, M

of ρ and β values corresponding to the three levels of distress severity. In some cases, there were no observed high or medium severity distress levels. Thus data were available for 24 out of a total of 33 possible sets of model calibration coefficients. The 24 sets of calibration coefficients are tabulated and graphs of the observed versus the predicted values of ρ and β are presented in Appendix N. Figures 49 through 59 present 11 sample sets of calculated distress curves, one for each of the pavement structure and climatic zone combinations, as listed in Table 25.

Figure 49 shows the predicted development of transverse reflection cracking (at the L-M-H, M-H, and H levels of severity) for an HMA overlay over a cracked asphalt pavement surface in a Wet-Freeze Zone (Lincoln, Maine). The H level of severity begins to appear at around 100 days of service life.

Figure 50 shows the predicted development of transverse reflection cracking and severity for an HMA overlay over a

jointed reinforced concrete pavement in a Wet-Freeze Zone (Beaver, Pennsylvania). The High level of severity remains low for a long time before beginning its sharp rise. The difference between the rates of distress development shown in Figures 49 and 50 is due mainly to the difference in thermal stresses.

Figure 51 shows the predicted development of transverse reflection cracking and severity of an HMA overlay over an open graded friction course which was used as a strain relieving interlayer over a cracked asphalt pavement surface in a Wet-Freeze Zone (Frederick, Maryland).

Figure 52 shows the predicted development of transverse reflection cracking and severity of an HMA overlay over a continuously reinforced concrete pavement surface in a Wet-Freeze Zone (Minnesota, Washington). The figure indicates no observed high severity reflection cracks.

Figure 53 shows the predicted development of transverse reflection cracking and severity of an HMA overlay reinforced

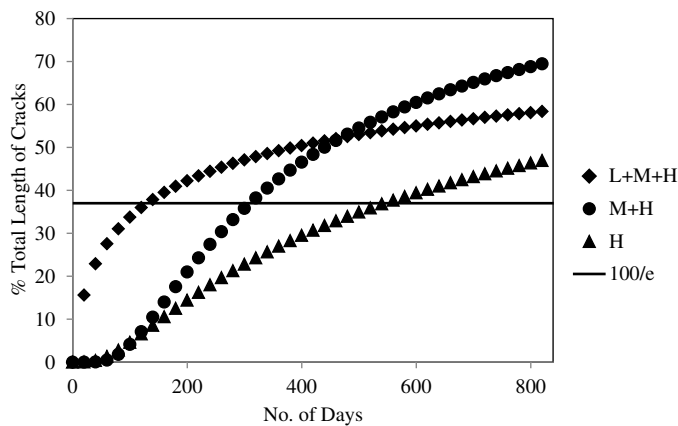


Figure 49. Development of transverse reflection cracking distress extent and severity for HMA overlay over asphalt surface in wet-freeze zone (Lincoln, Maine).

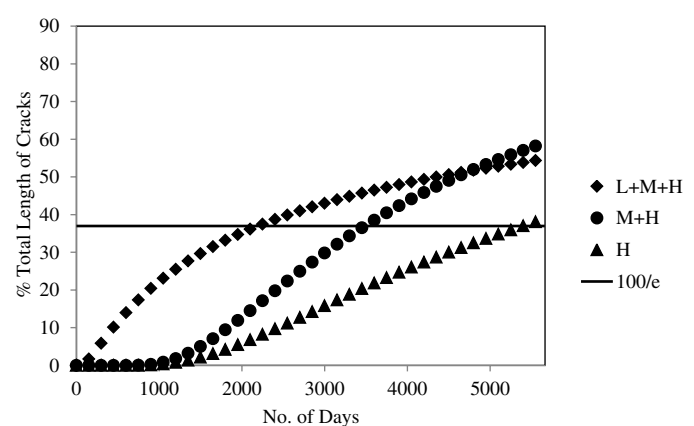


Figure 50. Development of transverse reflection cracking distress extent and severity for HMA overlay over jointed reinforced concrete in wet-freeze zone (Beaver, Pennsylvania).

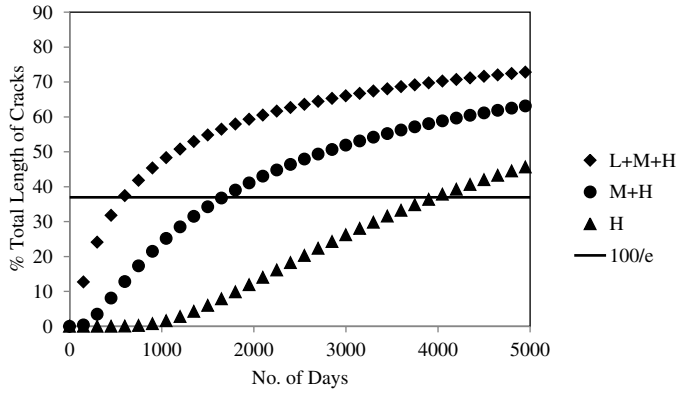


Figure 51. Development of transverse reflection cracking distress extent and severity for HMA overlay over friction course over asphalt surface in wet-freeze zone (Frederick, Maryland).

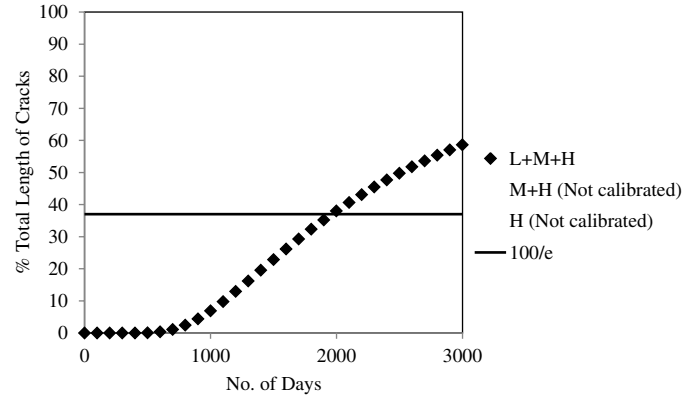


Figure 54. Development of transverse reflection cracking distress extent and severity for HMA overlay with reinforcing geosynthetic over asphalt surface in dry-freeze zone (Amarillo, Texas).

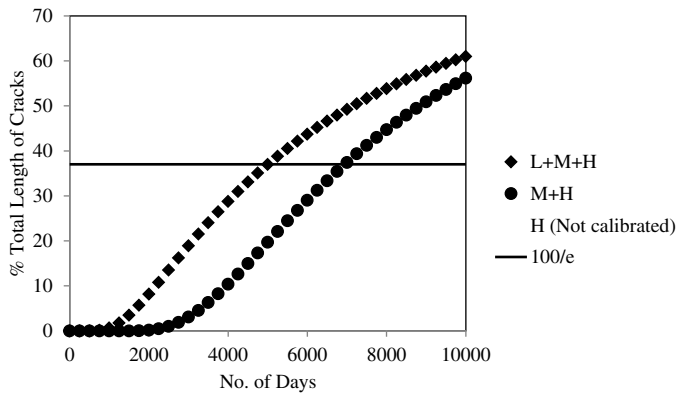


Figure 52. Development of transverse reflection cracking distress extent and severity for HMA overlay over continuously reinforced concrete pavement in wet-freeze zone (Minnesota, Washington).

with a geosynthetic material and placed over a jointed concrete pavement in a Wet-No Freeze Zone (Waco, Texas). Because medium or high levels of severity were not observed during the monitoring period, only the low level of severity could be modeled.

Figure 54 shows the predicted development of transverse reflection cracking and severity of an HMA overlay reinforced with a geosynthetic material and placed on a cracked asphalt pavement surface in a Dry-Freeze Zone (Amarillo, Texas). No medium or high level severity distress was observed on any of the test sections during the monitoring period.

Figure 55 shows the predicted development of transverse reflection cracking and severity of an HMA overlay over a cracked asphalt pavement surface in a Wet-No Freeze Zone (Pittsylvania, Virginia). The low severity distress appeared after about 1800 days and medium level severity began to

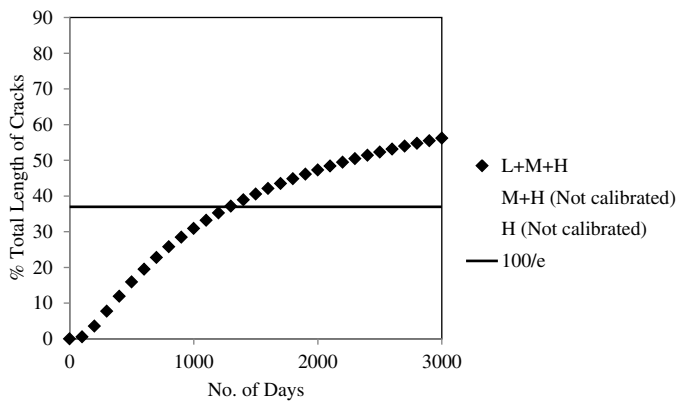


Figure 53. Development of transverse reflection cracking distress extent and severity for HMA overlay with reinforcing geosynthetic over jointed concrete in wet-no freeze zone (Waco, Texas).

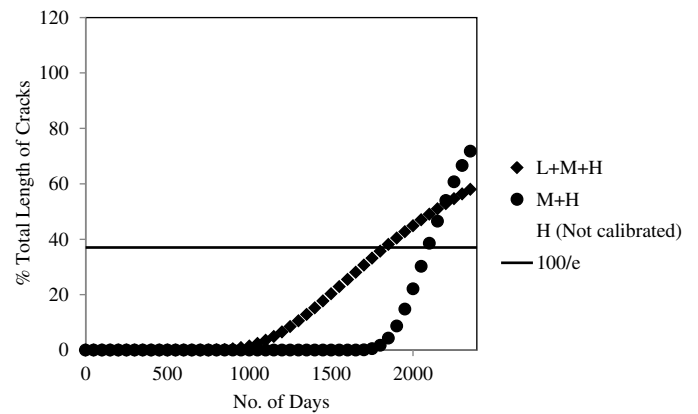


Figure 55. Development of transverse reflection cracking distress extent and severity for HMA overlay over asphalt surface in wet-no freeze zone (Pittsylvania, Virginia).

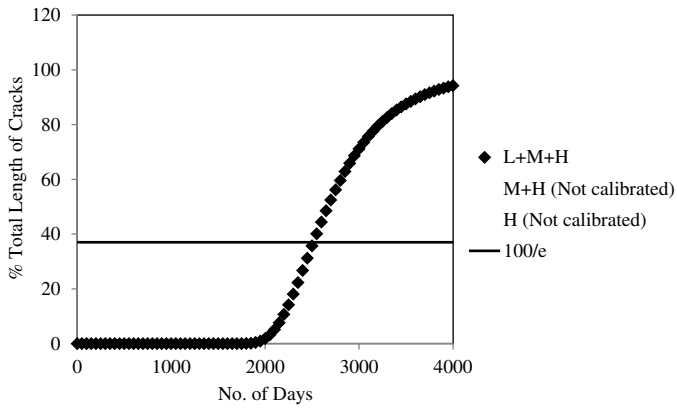


Figure 56. Development of transverse reflection cracking distress extent and severity for HMA overlay over friction course over asphalt surface in wet-no freeze zone (Yazoo, Mississippi).

appear after about six years; no high level severity distress was observed.

Figure 56 shows the predicted development of transverse reflection cracking and severity of an HMA overlay over an open graded friction course which was used as a strain relieving interlayer over a cracked asphalt pavement surface in a Wet-No Freeze Zone (Yazoo, Mississippi). Only the low level severity of distress was observed.

Figure 57 shows the predicted development of transverse reflection cracking and severity of an HMA overlay over a cracked asphalt pavement surface in a Dry-Freeze Zone (Deaf Smith County, Texas). The high, medium, and low levels of distress severity appeared within the first year.

Figure 58 shows the predicted development of transverse reflection cracking and severity of an HMA overlay over a

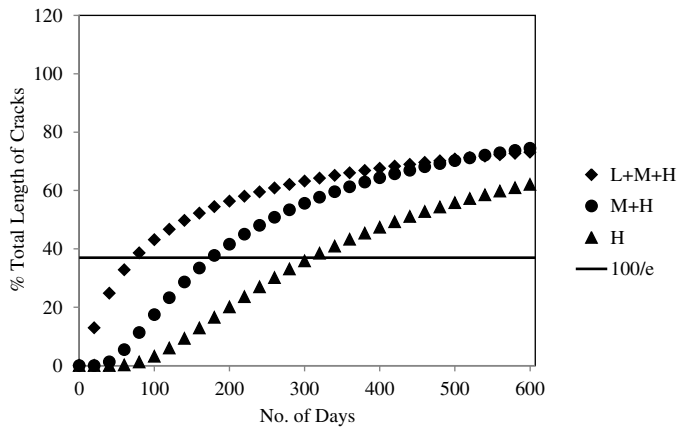


Figure 57. Development of transverse reflection cracking extent and severity for HMA overlay over asphalt pavement surface in dry-freeze zone (Deaf Smith County, Texas).

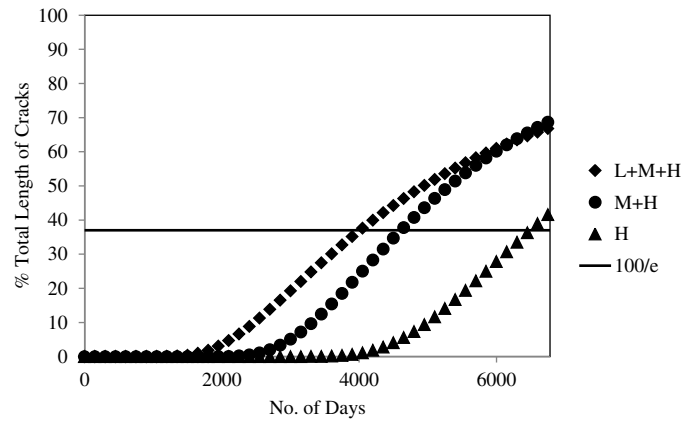


Figure 58. Development of transverse reflection cracking extent and severity for HMA overlay over asphalt pavement surface in dry-no freeze zone (Pinal, Arizona).

cracked asphalt pavement surface in a Dry-No Freeze Zone (Pinal, Arizona). The medium level severity of distress appeared and began its sharp rise after about 12 years.

Figure 59 shows the predicted development of transverse reflection cracking and severity of an HMA overlay with geosynthetic reinforcing over a jointed concrete pavement surface in a Wet-Freeze Zone (New York City). No high level severity distress was observed.

Figures 49 through 59 illustrate the predictions for each of the sets of reflection cracking model calibration coefficients. Each of the four major climatic zones are represented, but not all of the pavement structure-overlay types are. Although 11 sets of calibration coefficients were developed, a total of 40 combinations are possible (four climatic zones and 10 pavement structure-overlay types). All of these additional sets of

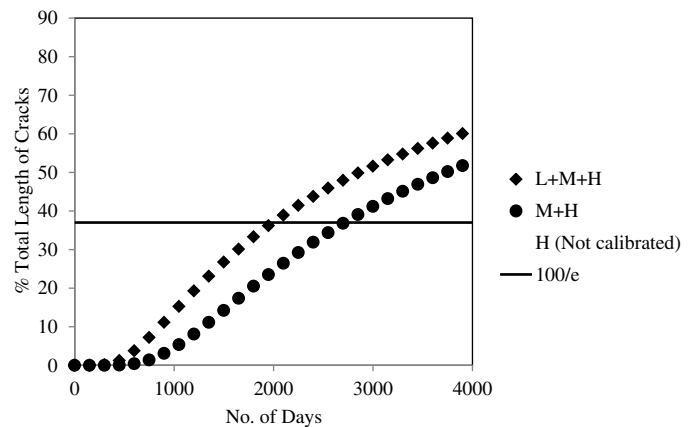


Figure 59. Development of transverse reflection cracking distress extent and severity for HMA overlay with reinforcing geosynthetic over jointed concrete pavement in wet-freeze zone (New York, New York).

calibration coefficients can be entered into this design program and can be used in the design of HMA overlays to represent each unique combination of climatic zone and pavement structure-overlay type. The remaining sets of calibration coefficients may be developed when a sufficient collection of field distress, pavement structure and materials, and traffic and weather data are assembled to repeat the process described in Chapter 2. In order to assist in such calibration efforts, a Calibration Program has been assembled and the User's Guide is provided in Appendix P.

It should be noted that if unrealistic input values are used, an unrealistic result can be expected from the predicted curves of reflection cracking extent and severity levels. Numerical trials in this project with the stress intensity factor and complex modulus ANN models have shown that they provide accurate extrapolations well beyond the values used to train them. These ANN algorithms are an integral part of both the calibration and design processes. However, they cannot be expected to produce realistic results if the input values are too far outside the range of their training values.

Calibration of the Computational Model to Field Data

The process of developing calibration coefficients is described in Chapter 2 and details of the process are contained in Appendices I through N. The Calibration Program, presented in Appendix P, generates five computed pavement reflection cracking lives that are required of each overlay in the original field data set.

At this point, the calibration process is completed by using linear regression analysis to produce the calibration coefficients for the overlay. The form of the model for the time scale value ρ is seen in Equations 40 through 43 and the same form of equation is used to model the shape factor β . Equations 40 through 42 are the form used if the principal cracking mechanisms are assumed to be bending stresses up to Position I and

thermal stresses are the principal mechanism from Position I up to the surface of the overlay. Equation 43 is an example of the form of the equation if bending stresses are assumed to be the principal cracking mechanism up to Position I and shearing stresses are assumed to be the principal cracking mechanism from Position I up to the surface of the overlay. All of these forms of equation are tried and calibration coefficients are found for each form of equation using linear regression analysis. The form of equation that produces the highest R^2 value and its corresponding set of calibration coefficients are selected as the best set for that type of overlay. Experience has shown that bending stresses are the principal cracking mechanism up to Position I and thermal stresses are the principal cracking mechanism from Position I up to the surface of the overlay, except for overlays with reinforcing interlayers. From this overlay, bending is the principal mechanism up to Position I and shearing is the principal mechanism from there up to the surface of the overlay. The reinforcing interlayer reduced the influence of thermal stress on the rate of crack growth in this type of overlay.

As a general rule, at least 10 overlay sections which are distinctively different from one another in their traffic, layer thicknesses, and overlay mix designs are needed to form a set of calibration coefficients. Validation of the developed sets of model coefficients involves the prediction of the distress of overlays that were not used in developing the original set of calibration coefficients. Such validation is desirable if sufficient additional overlay sections are available for this purpose.

The shape of the extent-severity-life curves was chosen to limit the percentage of cracking to be no more than 100 percent. The rate of rise of these curves is also constrained by the magnitude of the shape factor β . Generally, the scale factor ρ will be larger for the higher level of severity, although occasionally the H and the M+H curves will cross because of inverted values of β , as observed in Figures 49, 50, and 55. The logical structure in the design program does not prevent two severity curves from intersecting and this will occur on occasion.

CHAPTER 4

Summary and Suggested Research

Summary

A Reflection Cracking Overlay Design Program was calibrated using field data for more than 400 pavement test sections in 28 states and the four climatic zones of the United States. The program uses a mechanistic model that predicts the reflection cracking lives of a specified HMA overlay due to bending and shearing traffic stresses and thermal stresses. The relationship between the computed lives and the field conditions, in terms of the extent and severity of reflection cracking, depends upon the characteristics of the pavement structure and overlay and of the weather at the location. This relationship is expressed as sets of calibration coefficients that depend upon the season where the overlay was placed. A User's Guide for the Design Program is presented in Appendix O. It uses dialog boxes in the same format as the MEPDG and has the same three optional levels of input detail. The program is designed to run independently or to be incorporated as a subprogram of the MEPDG software.

A total of 11 sets of calibration coefficients were developed from the available data. The overlay performances that can be predicted with these different sets of calibration coefficients represent the four climatic zones in the United States. Eleven different pavement structure and overlay combinations were identified in the preliminary surveys. These overlays include HMA overlays over cracked asphalt pavement surfaces, jointed concrete pavement as well as asphalt overlays that use strain-absorbing membrane interlayers and reinforcing geosynthetics. When considering the four climatic zones, there are 36 possible sets of calibration coefficients. The methods of developing sets of calibration coefficients for overlays described in this report make it possible to develop sets of calibration coefficients for a specific type of overlay and to design overlays using these sets of calibration coefficients. A Calibration Program has been provided to facilitate this independent calibration process, and a User's Guide is provided in Appendix P. Both the Design Program and the Calibration Program have the same internal 150 location weather databases that can be called up by the user.

The calibration coefficients were developed in this project and used in the Reflection Cracking Overlay Design Model to produce reflection cracking predictions that match the field observations as closely as possible of the more commonly used overlays. The program runs quickly enough to allow speedy trials of several overlay thicknesses and asphalt mixes in order to find the design that best matches the project objectives. The computational speed is achieved partially by the use of ANN algorithms to perform the computations that must be done many times in the course of a simulated time period of 10 to 20 years. The ANN algorithms are used to compute the mixture modulus at different temperatures and loading rates and to calculate the stress intensity factors which drive the growth of cracks. Another factor in increasing the computational speed is re-writing all of the routines and subroutines in the same C # computer language.

Several examples of predicted reflection cracking performance of various overlays in different parts of the United States are presented in Chapter 3 and Appendix O. These examples illustrate the reproduction of the field observations of the growth of the extent and severity of reflection cracking. The assumed form of these distress growth curves was chosen because it gives realistic predictions and remains within reasonable bounds. However, extreme designs that are well outside the range of the types of overlays that were used for calibration may not produce realistic results.

Suggested Research

Another 25 sets of pavement structure-overlay and climatic zone combinations remain to be developed, some of which may not be possible because they are simply not built. However, the process of developing calibration coefficients for a particular type of overlay described in this report can be applied to any overlay in any region or even within a state or region. For example, sets of calibration coefficients for overlays incorporating geosynthetic reinforcing products need to be

developed (only three were developed in the project). It would also be desirable to develop guidelines or standards for such products to provide estimates of the reinforcing stiffness of these products.

The fit between the predicted and the observed reflection cracking distress can be improved by reducing the error in both the predicted and observed performance. The observed field data were fitted with an S-shaped curve with two parameters: ρ , the scale parameter and β , the shape parameter. Both of these parameters were fitted by linear regression analysis with mechanistically predicted numbers of days for traffic and thermal stresses to cause a reflection crack to grow to the surface of an overlay. There are errors that are inherent in both the observed and the predicted values. The error in the observed field data can be reduced by recording mean values of the observed distress from a sampling survey. The error in the mechanistically predicted numbers of days of crack propagation can be reduced by having more accurate recorded pavement structure and materials properties, traffic, and weather and by improving the cracking-predicting process of the mechanistic model.

A sensitivity analysis of the mechanistic model of the crack growth process will identify material properties which are the

most sensitive predictors of overlay performance. Making improvements in these material properties and how they are measured will extend the service lives of overlays and increase the predictive accuracy of the models that are developed. Performance-based specifications which are focused on these material properties will make construction quality control and quality assurance more effective and will extend the service lives of overlays.

The Design Program is a good candidate for incorporation into the MEPDG software framework or being a stand alone. Experience using the Design Program in designing overlays will show which sets of calibration coefficients need to be improved and, in addition, will reveal those features of a design that make the greatest extension of an overlay's service life.

An evaluation of available reflection cracking models was performed in this project and a number of promising approaches were in the development stage at that time. Most of these models proved to require extensive computational times that would make them impractical to use in design. However, as computer speeds increase, the mechanics-based methods will require less running time and should be considered for future versions of this overlay design function to reduce the systematic errors and simplify the calibration effort.

References

1. NCHRP 1-37A *Mechanistic Empirical Design of New and Rehabilitated Pavement Structures*. <http://www.trb.org/mepdg/guide.htm>. (2007).
2. Andrei, D., Witczak, M. W., and Mirza, M. W., *Development of a Revised Predictive Model for the Dynamic (Complex) Modulus of Asphalt Mixtures*. NCHRP 1-37 A Inter Team Report, University of Maryland, March, 1999.
3. Bari, J. and Witczak, M. W., Development of a New Revised Version of the Witczak E* Predictive Model for Hot Mix Asphalt Mixtures. *Journal of the Association of Asphalt Paving Technologists* 75, 2006.
4. Lytton, R. L., J. Uzan, E. G. Fernando, R. Roque, D. Hiltunen, and S. M. Stoffels, "Development and Validation of Performance Prediction Models and Specifications for Asphalt Binders and Paving Mixes," SHRP A-357, Transportation Research Board, National Research Council, Washington, D.C. (1993).
5. Long Term Pavement Performance, LTPP Data Base, <http://www.ltp-pp-products.com/index.asp>.
6. National Solar Radiation Database 1991–2005 Update: User's Manual. *Technical Report NREL/TP-581-41364*, April, 2007.
7. Monismith, C. L. and N. F. Coetzee, Reflection Cracking: Analysis, Laboratory Studies and Design Consideration, *Proceedings of Association of Asphalt Paving Technologists*, Vol. 49, 1980, pp. 268–313.
8. Nunn, M., An Investigation of Reflection Cracking in Composite Pavements in the United Kingdom, *Proceedings of 1st International RILEM Conference on Reflective Cracking in Pavements, Assessment and Control*, Liege University, Belgium, Edited by J. M. Rigo, et. al, March 1989.
9. Lytton, R. L. Use of Geotextiles for Reinforcement and Strain Relief in Asphaltic Concrete. *Geotextiles and Geomembranes*, Vol. 8, 1989, pp. 217–237.
10. Gary, B. E. and G. E. Martin, Resurfacing with Bituminous Types of Surfaces, *Proceedings of Highway Research Board*, National Research Council, Washington D.C., Vol. 12, 1932, pp. 177–192.
11. Paris, P. C. and Erdogan E., A Critical Analysis of Crack Propagation Laws, *Journal of Basic Engineering*, Transaction of the American Society of Mechanical Engineering, Series D., Vol. 85, pp. 528–883, 1963.
12. Jayawickrama, P. W., and Lytton, R. L., Methodology for Predicting Asphalt Concrete Overlay Life Against Reflection Cracking, *Proceedings 6th International Conference on Structural Design of Asphalt Pavements*, Volume I, pp. 912–924, 1987.
13. Wenting, L., and Scullion, T., "Modulus 6.0 for Windows: User's Manual," Research Report 1869-3, Texas Transportation Institute, Texas A&M University, College Station, Texas, 2001.
14. NCHRP, Guide for Mechanistic-Empirical Design of New and Rehabilitated Pavement Structures; Part 2. Design Inputs, Chapter 4. Traffic, National Cooperative Highway Research Program, 2004.
15. FHWA, Traffic Monitoring Guide. FHWA-PL-01-021, US Dept. of Transportation, Federal Highway Administration, Office of Highway Information Management, 2001.
16. Hajek, J. J., Selezneva, O. I., Mladenovic, G., and Jiang, Y. J., ESTIMATING CUMULATIVE TRAFFIC LOADS, Volume II: Traffic Data Assessment and Axle Load Projection for the Sites with Acceptable Axle Weight Data, Final Report for Phase 2. McLean, VA, Federal Highway Administration, 2008.
17. Sridhar, B. K, Characterization and Development of Axle Load Spectra to Enhance Pavement Design and Performance on the Basis of New Mechanistic-Empirical Design Guide in Louisiana. MS Thesis, Department of Civil and Environmental Engineering Louisiana State University, 2008.
18. Ahmed, Z., I. Marukic, S. Zaghoul, and N. Vitillo. Validation of Enhanced Integrated Climatic Model Predictions with New Jersey Seasonal Monitoring Data. In *Transportation Research Record: Journal of the Transportation Research Board*, No. 1913, Transportation Research Board of the National Academies, Washington, D.C., 2005, pp. 148–161.
19. Hermansson, A. Simulation Model for Calculating Pavement Temperatures, Including Maximum Temperature. *Transportation Research Record: Journal of the Transportation Research Board*, No. 1699, Transportation Research Board of the National Academies, Washington, D.C., 2000, pp. 134–141.
20. Gui, J., P. E Phelan, K. E. Kaloush, and J. S. Golden. Impact of Pavement Thermophysical Properties on Surface Temperature. *Journal of Materials in Civil Engineering*, Vol. 19, 2007, pp. 683–690.
21. Hermansson, A., Mathematical Model for Paved Surface Summer and Winter Temperature: Comparison of Calculated and Measured Temperatures. *Cold Regions Science and Technology*, Vol. 40, 2004, pp. 1–17.
22. Halil C., Gopalakrishnan, K., and Kim S. Looking to the Future: The Next-Generation Hot Mix Asphalt Dynamic Modulus Prediction Models, *International Journal of Pavement Engineering*, 2009, pp. 1–12.
23. Tsoukalas, L. H. and Uhrig, R. E., *Fuzzy and Neural Approaches in Engineering*, Wiley, New York, 1997.
24. Adeli, H., *Neural Networks in Civil Engineering: 1989–2000. Computer-Aided Civil and Infrastructure Engineering*, Vol. 16, 2001, pp. 126–142.

25. Fernando, E. G., Nusanu, D., Park, D., and Liu, W., Summary Report: Evaluation of Effects of Tire Size and Inflation Pressure on Tire Contact Stresses and Pavement Response. Technical Report 0-4361-1. College Station, Texas, Texas Transportation Institute, 2006.
 26. Ratkowsky, D. A., Handbook of Nonlinear Regression Models. New York, M. Dekker, 1990.
 27. Mallela, J. and H. Von Quintus, Investigation of Reflective Crack Control Measures for HMA Overlays of PCC Pavements, Submitted to City of New York Department of Design and Construction Division of Infrastructure, Applied Research Associates Inc., 2007.
 28. Button, J. W. and A. Chowdhury, Field Tests Using Geosynthetics in Flexible and Rigid Pavements to Reduce Reflection Cracking. FHWA/TX-06/0-1777-2, Texas Transportation Institute, College Station, Texas, 2006.
 29. Natke, H. G., Identification of Vibrating Structures, Springer-Verlag, New York, 1982.
 30. Wang, F. and R. L. Lytton, "System Identification Method for Back-calculating Pavement Layer Properties." *Transportation Research Record 1384*, Transportation Research Board, National Research Council, Washington, D.C.: pp. 1-7. 1993.
 31. Zollinger, D. G., S. Lee, J. Puccinelli, and N. Jackson, LTPP Computed Parameter: Moisture Content, FHWA-HRT-08-035, Federal Highway Administration, 2008.
 32. Dempsey, B. J., W. A. Herlach, and A. J. Patel, *The Climatic-Material-Structural Pavement Analysis Program*, FHWA/RD-84/115, Vol. 3., Final Report, Federal Highway Administration, Washington D.C., 1985.
 33. Lytton, R. L., D. E. Pufahl, C. H. Michalak, H. S. Liang, and B. J. Dempsey, *An Integrated Model of the Climatic Effects on Pavement*, Texas Transportation Institute, Texas A&M University, Report No. FHWA-RD-90-033, Federal Highway Administration, McLean, VA, 1990.
 34. Larson, G., and B. J. Dempsey, *Integrated Climatic Model, Version 2.0*. Newmark Civil Engineering Laboratory, University of Illinois at Urbana-Champaign, Illinois. Report No. DTFA MN/DOT 72114, 1997.
 35. Halil C., K. Gopalakrishnan, and S. Kim. Looking to the future: the next-generation Hot Mix Asphalt Dynamic Modulus Prediction Models, *International Journal of Pavement Engineering*, 2009, pp. 1-12.
 36. Schapery, R. A., *A Theory of Crack Growth in Visco-Elastic Media*, Report MM 2764-73-1, Mechanics and Materials Research Centre, Texas A&M University, College Station, Texas, 1973.
 37. Schapery, R. A., A Theory of Crack Initiation and Growth in Visco-Elastic Media; I: Theoretical Development, II: Approximate Methods of Analysis, III: Analysis of Continuous Growth, *International Journal of Fracture*, Sijthoff and Noordhoff International Publisher, Vol. 11, No. 1, pp. 141-159., Vol. 11, No. 3, pp. 369-388, and Vol. 11, No. 4, pp. 549-562, 1975.
 38. Hiltunen, D. R. and Roque, R., "A Mechanics-Based Prediction Model for Thermal Cracking of Asphaltic Concrete Pavements," *Association of Asphalt Paving Technologists*, Vol. 63, 1994, pp. 81-117.
 39. Williams, M. L., Landel, R. F., and Ferry, J. D., *Journal of American Chemical Society*, 1955, Vol. 77, pp. 3701.
-

Appendices

Appendices A through T are not published herein but they are available on the *NCHRP Report 669* summary web page at <http://www.trb.org/Main/Blurbs/163988.aspx>. The titles of the appendices are:

- Appendix A: Program Flow Charts
- Appendix B: Pavement Temperature Prediction
- Appendix C: Categorization of Traffic Loads
- Appendix D: Cumulative Axle Load Distribution as a Function of Tire Footprint Length
- Appendix E: Determination of Hourly Traffic Numbers
- Appendix F: Artificial Neural Network Models of Stress Intensity Factors
- Appendix G: Binder and Mixture Properties
- Appendix H: Fracture Properties of Asphalt Mixtures
- Appendix I: Viscoelastic Thermal Stress Computation
- Appendix J: Collection of Test Sections and Field Performance Data
- Appendix K: Reflection Cracking Amount and Severity Model
- Appendix L: Calibration of the Reflection Cracking Amount and Severity Model
- Appendix M: Calibrated Parameters of the Reflection Cracking Amount and Severity Model
- Appendix N: Calibration of the Computational Model to Field Data
- Appendix O: User's Guide to the Reflection Cracking Model
- Appendix P: User's Guide to the Computational Model to Field Data Calibration Program
- Appendix Q: Finite Element Program to Calculate Stress Intensity Factor
- Appendix R: Evaluation of Available Reflection Cracking Models
- Appendix S: Sensitivity Analysis of Designing Program
- Appendix T: The Comparison of Field Data and Predicting Results

Abbreviations and acronyms used without definitions in TRB publications:

AAAE	American Association of Airport Executives
AASHO	American Association of State Highway Officials
AASHTO	American Association of State Highway and Transportation Officials
ACI-NA	Airports Council International-North America
ACRP	Airport Cooperative Research Program
ADA	Americans with Disabilities Act
APTA	American Public Transportation Association
ASCE	American Society of Civil Engineers
ASME	American Society of Mechanical Engineers
ASTM	American Society for Testing and Materials
ATA	Air Transport Association
ATA	American Trucking Associations
CTAA	Community Transportation Association of America
CTBSSP	Commercial Truck and Bus Safety Synthesis Program
DHS	Department of Homeland Security
DOE	Department of Energy
EPA	Environmental Protection Agency
FAA	Federal Aviation Administration
FHWA	Federal Highway Administration
FMCSA	Federal Motor Carrier Safety Administration
FRA	Federal Railroad Administration
FTA	Federal Transit Administration
HMCRP	Hazardous Materials Cooperative Research Program
IEEE	Institute of Electrical and Electronics Engineers
ISTEA	Intermodal Surface Transportation Efficiency Act of 1991
ITE	Institute of Transportation Engineers
NASA	National Aeronautics and Space Administration
NASAO	National Association of State Aviation Officials
NCFRP	National Cooperative Freight Research Program
NCHRP	National Cooperative Highway Research Program
NHTSA	National Highway Traffic Safety Administration
NTSB	National Transportation Safety Board
PHMSA	Pipeline and Hazardous Materials Safety Administration
RITA	Research and Innovative Technology Administration
SAE	Society of Automotive Engineers
SAFETEA-LU	Safe, Accountable, Flexible, Efficient Transportation Equity Act: A Legacy for Users (2005)
TCRP	Transit Cooperative Research Program
TEA-21	Transportation Equity Act for the 21st Century (1998)
TRB	Transportation Research Board
TSA	Transportation Security Administration
U.S.DOT	United States Department of Transportation